Impulse of a Single-Pulse Detonation Tube

E. Wintenberger, J.M. Austin, M. Cooper, S. Jackson, and J.E. Shepherd

Graduate Aeronautical Laboratories
California Institute of Technology
Pasadena, CA 91125
U.S.A.

GALCIT Report FM 00-8

Revised August 2002

Contents

List of Figures

List of Tables

Part I
Foreword

This report describes experimental and numerical investigations on pulse detonation tubes carried out in the Explosion Dynamics Laboratory at Caltech during 1999-2002. The goal of this work was to develop a database on impulse measurements using direct ballistic measurement of impulse; and to develop a model based on simple gas dynamic principles that could be used to predict impulse for a wide range of fuels and initial conditions. At the time we started this work, there was a great deal of conflicting information regarding the values of impulse that could be obtained. Our goal was to clarify this situation and to develop a better understanding of the factors that controlled impulse generation in a pulse detonation tube – the simplest version of a pulse detonation engine. Since we began this project, many groups from throughout the world have made impulse models, carried out new numerical studies, and made direct experimental measurements of impulse. The work of these researchers has been invaluable to us as we refined and tested our ideas against their data and ours. We would like to acknowledge discussions with Fred Schauer (AFRL, USA), Chris Brophy (NPS,USA), K. Kailasanath (NRL, USA), R. Santoro (PSU, USA), Andrew Higgins (McGill University), Paul Harris (DREV, Canada), and E. Daniau (ENSMA - France). In particular, we thank Fred Schauer for generously sharing his data with us.

We initially began preparing this report in 2000 and it went through a number of revisions with portions being presented at the Joint Propulsion Conference in the summer of 2001. Subsequently, the material underwent further revision and additions in preparation for journal publication and the orginal report was significantly out of date. We have chosen to replace the original text with preprints of our journal articles and retained the appendices to the original report. The material in Parts II and III consist of preprints of revised versions (accepted for publications) of two papers submitted to the Journal of Propulsion and Power in the winter of 2001-2002. The Appendices contain additional details about the modeling, details on the experimental setup, tabulated data from the experiments, and tabulated results of model computations.

Part II
Analytical Model

This part is a reprint of a paper prepared for the Journal of Propulsion and Power. It describes an analytical model for predicting the impulse from a pulse detonation tube.

An analytical model for the impulse of a single-cycle pulse detonation tube

E. Wintenberger, J.M. Austin, M. Cooper, S. Jackson, and J.E. Shepherd
Graduate Aeronautical Laboratories,
California Institute of Technology, Pasadena, CA 91125

Abstract

An analytical model for the impulse of a single-cycle pulse detonation tube has been developed and validated against experimental data. The model is based on the pressure history at the thrust surface of the detonation tube. The pressure history is modeled by a constant pressure portion followed by a decay due to gas expansion out of the tube. The duration and amplitude of the constant pressure portion is determined by analyzing the gas dynamics of the self-similar flow behind a steadily-moving detonation wave within the tube. The gas expansion process is modeled using dimensional analysis and empirical observations. The model predictions are validated against direct experimental measurements in terms of impulse per unit volume, specific impulse, and thrust. Comparisons are given with estimates of the specific impulse based on numerical simulations. Impulse per unit volume and specific impulse calculations are carried out for a wide range of fuel-oxygen-nitrogen mixtures (including aviation fuels) varying initial pressure, equivalence ratio, and nitrogen dilution. The effect of the initial temperature is also investigated. The trends observed are explained using a simple scaling analysis showing the dependency of the impulse on initial conditions and energy release in the mixture.

1 Nomenclature

A	cross-sectional area of detonation tube
c_1	sound speed of reactants
c_2	sound speed of burned gases just behind detonation wave
c_3	sound speed of burned gases behind Taylor wave
$\hat{C}^-$	first reflected characteristic to reach the thrust surface
$C^\pm$	characteristics, left and right-facing families
d	inner diameter of detonation tube
f	cycle repetition frequency
g	standard earth gravitational acceleration
$\mathcal{H}$	non-dimensional heat release
I	single-cycle impulse
I_{sp}	mixture-based specific impulse
I_{spf}	fuel-based specific impulse
I_V	impulse per unit volume
J^-	Riemann invariant on a left-facing characteristic
K	proportionality coefficient
L	length of detonation tube
$\mathcal{L}$	critical length scale for DDT
M	total mass of initial combustible mixture within detonation tube
M_{CJ}	Chapman-Jouguet Mach number
M_f	initial mass of fuel within detonation tube
P	pressure
P_0	pressure outside detonation tube
P_1	initial pressure of reactants
P_2	Chapman-Jouguet pressure
P_3	pressure of burned gases behind Taylor wave
P_e	exhaust pressure
q	effective energy release per unit mass calculated from M_{CJ}
q_c	heat of combustion per unit mass of mixture
R	gas constant
t	time
t_1	time taken by the detonation wave to reach the open end of the tube
t_2	time taken by the first reflected characteristic to reach the thrust surface
t_3	time associated with pressure decay period
t^*	time at which the first reflected characteristic exits the Taylor wave

T	thrust
T_1	initial temperature of reactants
T_2	Chapman-Jouguet temperature
u	flow velocity
u_2	flow velocity just behind detonation wave
u_e	exhaust velocity
U_{CJ}	Chapman-Jouguet detonation velocity
V	volume of gas within detonation tube
X_F	fuel mass fraction
α	non-dimensional parameter corresponding to time t_2
β	non-dimensional parameter corresponding to pressure decay period
ΔP	pressure differential
ΔP_3	pressure differential at the thrust surface
η	similarity variable
γ	ratio of specific heats
λ	cell size
ϕ	equivalence ratio
Π	non-dimensional pressure
ρ_1	initial density of reactants
ρ_e	exhaust density
τ	non-dimensional time ct/L

2 Introduction

A key issue[5, 6, 7, 8, 9] in evaluating pulse detonation engine (PDE) propulsion concepts is reliable estimates of the performance as a function of operating conditions and fuel types. A basic PDE consists of an inlet, a series of valves, a detonation tube (closed at one end and open at the other), and an exit nozzle. It is an unsteady device which uses a repetitive cycle to generate thrust. The engine goes through four major steps during one cycle: the filling of the device with a combustible mixture, the initiation[a] of the detonation near the closed end (thrust surface), the propagation of the detonation down the tube, and finally, the exhaust of the products into the atmosphere. A schematic of the cycle for the detonation tube alone is shown in Fig. 1. The pressure differential created by the detonation wave on the tube's thrust surface produces unsteady thrust. If the cycle is repeated at a constant frequency, typically 10 to 100 Hz, an average thrust useful for propulsion is generated.

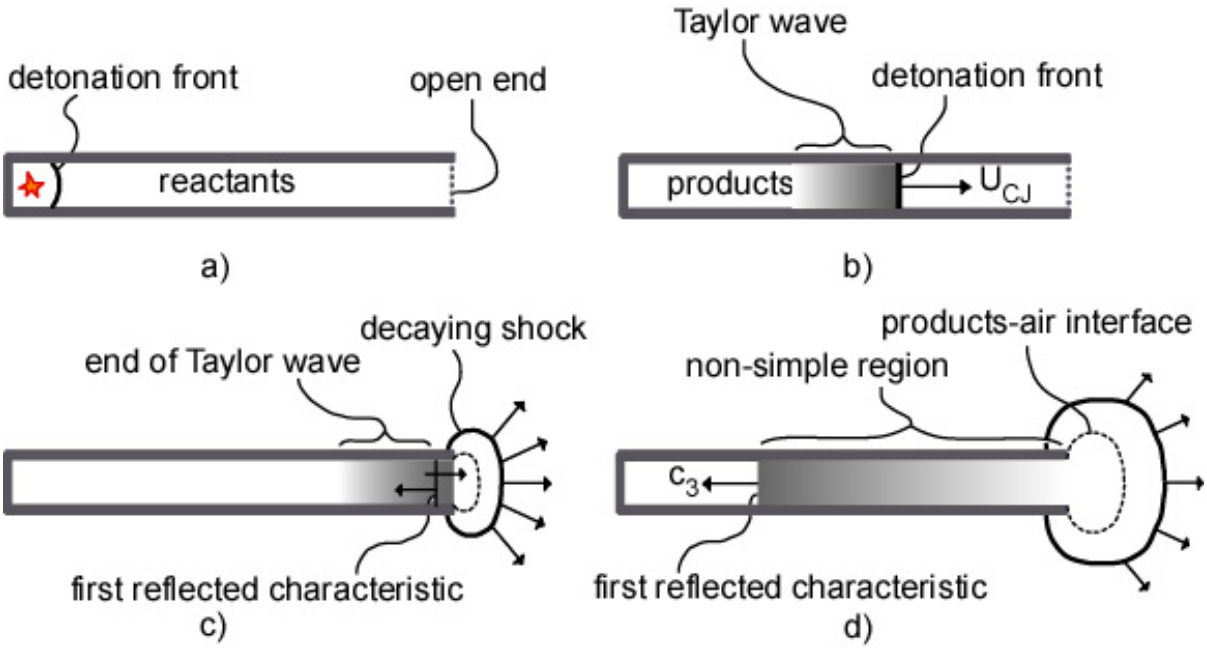

Figure 1: Pulse detonation engine cycle: a) The detonation is initiated at the thrust surface. b) The detonation, followed by the Taylor wave, propagates to the open end of the tube at a velocity U_{CJ}. c) An expansion wave is reflected at the mixture-air interface and immediately interacts with the Taylor wave while the products start to exhaust from the tube. d) The first characteristic of the reflected expansion reaches the thrust surface and decreases the pressure at the thrust surface.

The goal of the present study is to provide a simple predictive model for detonation

[a]Initiation at the closed end of the tube is not an essential part of PDE operation but greatly simplifies the analysis and will be used throughout the present study. Zhdan et al.[10] found that the impulse is essentially independent of the igniter location for prompt initiation.

tube thrust. In order to do that, we have to carry out a fully unsteady treatment of the flow processes within the tube. This is a very different situation from modeling conventional propulsion systems such as turbojets, ramjets, and rockets for which steady-state, steady-flow analyses define performance standards. In those conventional systems, thermodynamic cycle analyses are used to derive simple but realistic upper bounds for thrust, thrust-specific fuel consumption, and other performance figures of merit. Due to the intrinsically unsteady nature of the PDE, the analogous thermodynamic bounds on performance have been elusive.

Unlike some previous[6] and contemporary[11] analyses, we do not attempt to replace the unsteady PDE cycle with a fictitious steady-state, steady-flow cycle. Although these analyses are purported to provide an ideal or upper bound for performance, we find that these bounds are so broad that they are unsuitable for making realistic performance estimates for simple devices like a detonation tube. This becomes clear when comparing the predicted upper bound values[6, 11] of 3000-5000 s for the fuel-based specific impulse of typical stoichiometric hydrocarbon-air mixtures with the measured values of about 2000 s obtained in detonation tube experiments[12, 10, 1, 13]. Instead, the present model focuses on the gas dynamic processes in the detonation tube during one cycle. The model is based on a physical description of the flow inside the tube and uses elementary one-dimensional gas dynamics and dimensional analysis of experimental observations. The model computes the impulse delivered during one cycle of operation as the integral of the thrust during one cycle.

It is critical to gain understanding of the single-cycle impulse of a detonation tube before more complex engine configurations are considered. There have been a number of efforts to develop a gas dynamics-based model for single-cycle operation of detonation tubes. The pioneering work on single-cycle impulse was in 1957 by Nicholls et al.[14] who proposed a very simplified model for the impulse delivered during one cycle. Only the contribution of the constant pressure portion at the thrust surface was considered and the contribution of the pressure decay period was neglected. Consequently, their model predictions are about 20% lower than the results of our model presented here and the values obtained from modern experiments.

Zitoun and Desbordes[12] proposed a model for the single-cycle impulse and compared this to their experimentally measured data. They showed predictions for stoichiometric mixtures of ethylene, hydrogen and acetylene with oxygen and air. The models of Nicholls et al.[14], Zitoun and Desbordes[12], and the more recent work of Endo and Fujiwara[15] have many features in common with the present model since they are all based on a simple gas dynamic description of the flow field. Zhdan et al.[10] used both numerical simulations and simple analytical models based on the results of Stanyukovich [16] to predict the impulse for tubes completely and partially filled with a combustible mixture.

In addition to analytical models, numerous numerical simulations have investigated various aspects of PDEs. Early studies, reviewed by Kailasanath et al.[17], gave disparate and often contradictory values for performance parameters. Kailasanath and Patnaik[9] identified how the issue of outflow boundary conditions can account for some of these discrepancies. With the recognition of this issue and the availability of high-quality ex-

perimental data, there is now substantial agreement[18] between careful numerical simulation and experimental data, at least in the case of ethylene-air mixtures. However, even with improvements in numerical capability, it is desirable to develop simple analytical methods that can be used to rapidly and reliably estimate the impulse delivered by a detonation tube during one cycle in order to predict trends and to better understand the influence of fuel type, initial conditions, and tube size without conducting a large number of numerical simulations.

An end-to-end performance analysis of a pulse detonation engine has to take into account the behavior of the inlet, the valves, the combustor, and the exit nozzle. However, the ideal performance is mainly dictated by the thrust generation in the detonation tube. In developing our model, we have considered the simplest configuration of a single-cycle detonation tube open at one end and closed at the other. We realize that there are significant issues[7] associated with inlets, valves, exit nozzles, and multi-cycle operation that are not addressed in our approach. However, we are anticipating that our simple model can be incorporated into more elaborate models that will account for these features of actual engines and that the present model will provide a basis for realistic engine performance analysis.

The paper is organized as follows. First, we describe the flow field for an ideal detonation propagating from the closed end of a tube towards the open end. We describe the essential features of the ideal detonation, the following expansion wave, and the relevant wave interactions. We present a simple numerical simulation illustrating these issues. Second, we formulate a method for approximating the impulse with a combination of analytical techniques and dimensional analysis. Third, the impulse model is validated by comparison with experimental data and numerical simulations. Fourth, a scaling analysis is performed to study the dependency of the impulse on initial conditions and energy release in the mixture. Fifth, the impulse model is used to compute impulse for a range of fuels and initial conditions. The influence of fuel type, equivalence ratio, initial pressure, and initial temperature are examined in a series of parametric computations.

3 Flow field associated with an ideal detonation in a tube

The gas dynamic processes that occur during a single cycle of a PDE can be summarized as follows. A detonation wave is directly initiated and propagates from the thrust surface towards the open end. For the purposes of formulating our simple model, we consider ideal detonations described as discontinuities propagating at the Chapman-Jouguet (CJ) velocity. The detonation front is immediately followed by a self-similar expansion wave[19, 20] known as the Taylor wave. This expansion wave decreases the pressure and brings the flow to rest. The method of characteristics[20, 19] can be used to calculate flow properties within the Taylor wave (see Eqs. 11, 12, 13 in the following section).

There is a stagnant region extending from the rear of the Taylor wave to the closed end of the tube. When the detonation reaches the open end of the tube, a shock is

generated and diffracts out into the surrounding air. Because the pressure at the tube exit is higher than ambient, the transmitted shock continues to expand outside of the tube. Since the flow at the tube exit is subsonic, a reflected wave propagates back into the tube. This reflected wave is usually an expansion wave, which reflects from the closed end, reducing the pressure and creating an expansion wave that propagates back towards the open end. After several sequences of wave propagation within the tube, the pressure inside approaches atmospheric. A simplified, but realistic model of the flow field can be developed by using classical analytical methods.

3.1 Ideal detonation and Taylor wave

In order to predict the ideal impulse performance of a pulsed detonation tube, we can consider the detonation as a discontinuity that propagates with a constant velocity. This velocity is a function of the mixture composition and initial thermodynamic state. The reaction zone structure and the associated property variations such as the Von Neumann pressure spike are neglected in this model since the contribution of these features to the impulse is negligible.

The detonation speed is determined by the standard CJ model of a detonation that assumes that the flow just downstream of the detonation is moving at sonic velocity relative to the wave. This special downstream state, referred to as the CJ point, can be found by numerically solving the relations for mass, momentum, and energy conservation across the discontinuity while simultaneously determining the chemical composition. Equilibrium computations[21] based on realistic thermochemical properties and a mixture of the relevant gas species in reactants and products are used to calculate the chemical composition.

Alternatively, the conservation equations can be analytically solved for simple models, using an ideal gas equation of state, a fixed heat of reaction, and heat capacities that are independent of temperature. A widely used version of this model, described in Thompson[22], uses different properties in the reactants and products, and a fixed value of the energy release, q, within the detonation wave. In the present study we use an even simpler version,[23] the one-γ model, which neglects the differences in specific heat and molar mass between reactants and products.

3.2 Interaction of the detonation with the open end

The flow behind a CJ detonation wave is subsonic relative to the tube and has a Mach number $M_2 = u_2/c_2$ of approximately 0.8 for typical hydrocarbon mixtures. Hence, when the detonation wave reaches the open end, a disturbance propagates back into the tube in the form of a reflected wave[24]. The interface at the open end of the tube can be modeled in one dimension as a contact surface. When the detonation wave is incident on this contact surface, a transmitted wave will propagate out of the tube while a reflected wave propagates into the tube towards the thrust surface.

The reflected wave can be either a shock or an expansion wave. A simple way to

determine the nature of the reflected wave is to use a pressure-velocity diagram[24], as the pressure and velocity must be matched across the contact surface after the interaction. In the case of a detonation wave exiting into air, the transmitted wave will always be a shock wave; the locus of solutions (the shock adiabat) is shown in Figs. 2 and 3. The shock adiabat is computed from the shock jump conditions, which can be written in term of the pressure jump and velocity jump across the wave

$$\frac{\Delta u}{c_1} = \frac{\Delta P/P_1}{\gamma\left(1+\frac{\gamma+1}{2\gamma}\frac{\Delta P}{P_1}\right)^{\frac{1}{2}}} \ . \tag{1}$$

The reflected wave initially propagates back into the products at the CJ state behind the detonation wave. The CJ states for various fuels and equivalence ratios appear in Figs. 2 and 3. If the CJ point is below the shock adiabat, the reflected wave must be a shock to increase the pressure to match that behind the transmitted shock. Alternatively, if the CJ state is above the shock adiabat, the reflected wave must be an expansion in order to decrease the pressure to match that behind the transmitted shock. Hydrocarbon fuels all produce a reflected expansion wave at the tube's open end for any stoichiometry. However, a reflected shock is obtained for hydrogen-oxygen at an equivalence ratio $\phi > 0.8$ (Fig. 2) and for very rich hydrogen-air mixtures with $\phi > 2.2$ (Fig. 3).

Ultimately, following the initial interaction of the detonation wave with the contact surface, the pressure at the exit of the tube will drop as the transmitted shock wave propagates outward. In all cases, since the flow outside the tube is expanding radially behind the diffracting shock wave, an expansion wave also exists in the flow external to the tube. The flow in this region can not be modeled as one-dimensional. A numerical simulation (discussed below) is used to illustrate this portion of the flow.

3.3 Waves and space-time diagram

A space-time (x–t) diagram, shown in Fig. 4, is used to present the important features of the flow inside the tube. The x–t diagram displays the detonation wave propagating at the CJ velocity U_{CJ} followed by the Taylor wave. The first characteristic $\hat{C}^-$ of the wave reflected from the mixture-air interface at the open end of the tube is also shown. The initial slope of this characteristic is determined by the conditions at the mixture-air interface and is then modified by interaction with the Taylor wave. After passing through the Taylor wave, the characteristic $\hat{C}^-$ propagates at the sound speed c_3. The region lying behind this first characteristic is non-simple because of the interaction between the reflected expansion wave and the Taylor wave. Two characteristic times can be defined: t_1 corresponding to the interaction of the detonation wave with the open end, and t_2 corresponding to the time necessary for the characteristic $\hat{C}^-$ to reach the thrust surface. The diffracted shock wave in Fig. 4 is shown outside the tube as a single trajectory; however, this is actually a three-dimensional wavefront that can not be fully represented on this simple plot.

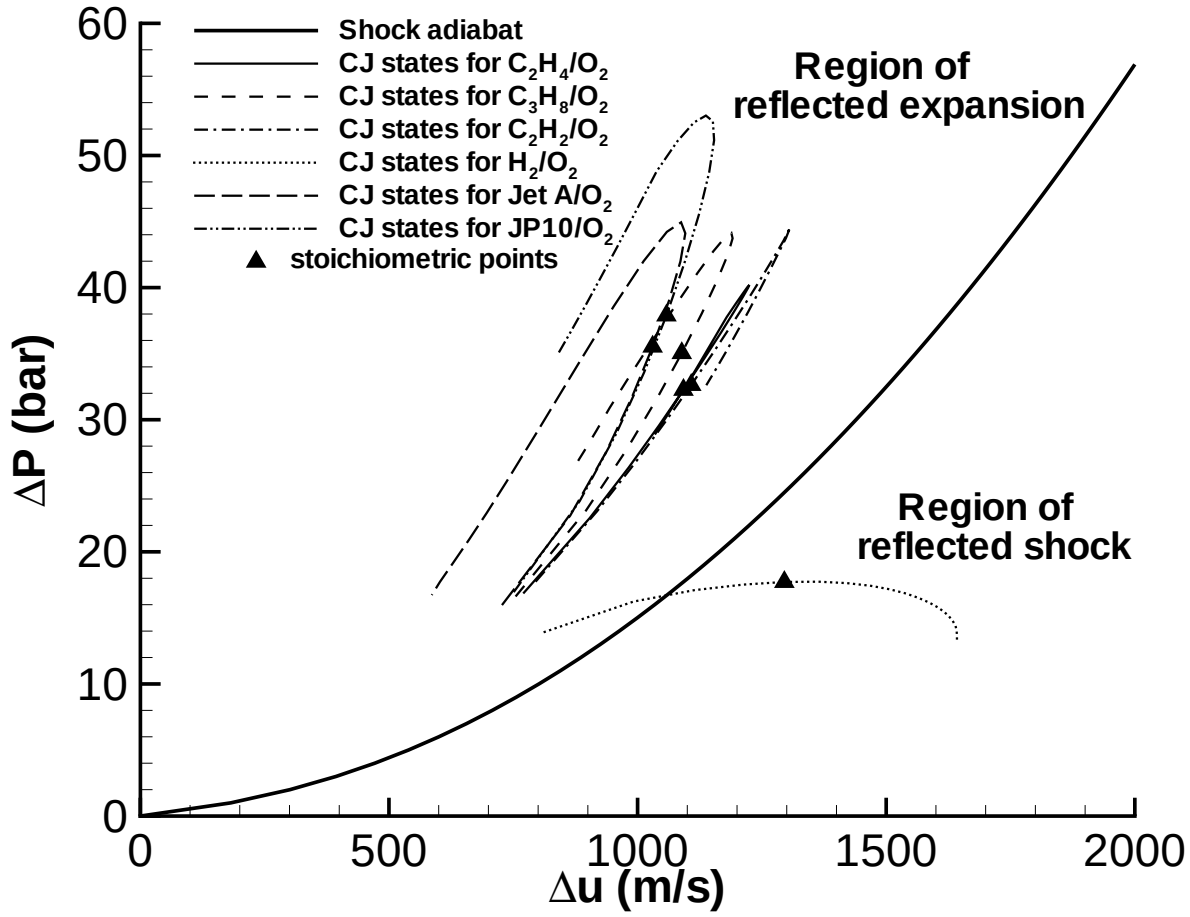

Figure 2: Pressure-velocity diagram used to compute wave interactions at the tube open end for fuel-oxygen mixtures.

3.4 A numerical simulation example

In order to further examine the issues related to the interaction of the detonation with the open end of the tube, the flow was investigated numerically[25] using Amrita[26]. The Taylor wave similarity solution[19, 20] was used as an initial condition, assuming the detonation has just reached the open end of the tube when the simulation is started. This solution was calculated using a one-γ model for detonations[23, 22] for a non-dimensional energy release $q/RT_1 = 40$ across the detonation and $\gamma = 1.2$ for reactants and products. The corresponding CJ parameters are $M_{CJ} = 5.6$ and $P_{CJ}/P_1 = 17.5$, values representative of stoichiometric hydrocarbon-air mixtures.

The initial pressure P_1 ahead of the detonation wave was taken to be equal to the pressure P_0 outside the detonation tube. The simulation solved the non-reactive Euler equations using a Kappa-MUSCL-HLLE solver in the two-dimensional (cylindrical symmetry) computational domain consisting of a tube of length L closed at the left end and open to a half-space at the right end. Numerical schlieren images are displayed in Fig. 5,

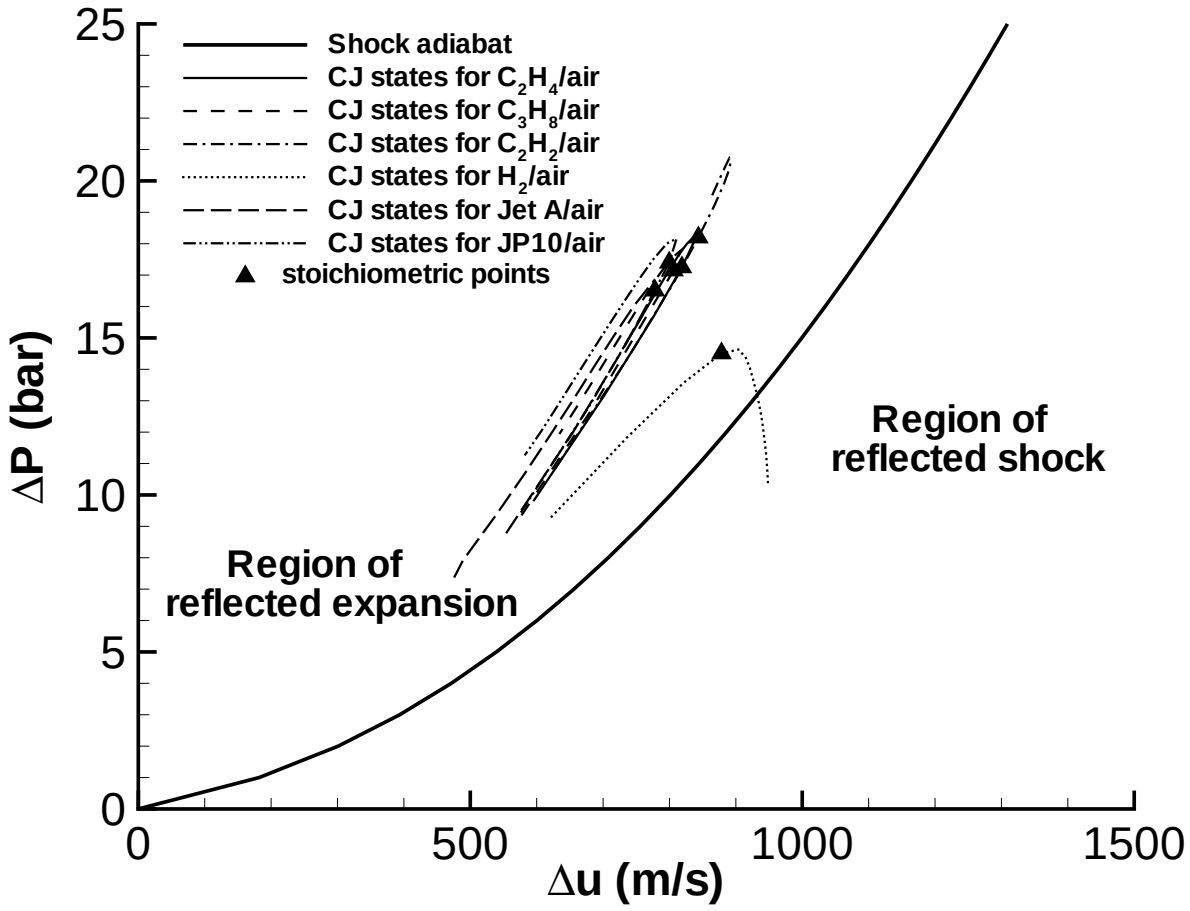

Figure 3: Pressure-velocity diagram used to compute wave interactions at the tube open end for fuel-air mixtures.

and the corresponding pressure and horizontal velocity profiles along the tube centerline are shown on Figs. 6 and 7, respectively. Only one-half of the tube is shown in Fig. 5; the lower boundary is the axis of symmetry of the cylindrical detonation tube. The times given on these figures account the initial detonation travel from the closed end to the open end of the tube, so that the first frame of Figs. 5, 6, and 7 corresponds to a time $t_1 = L/U_{CJ}$.

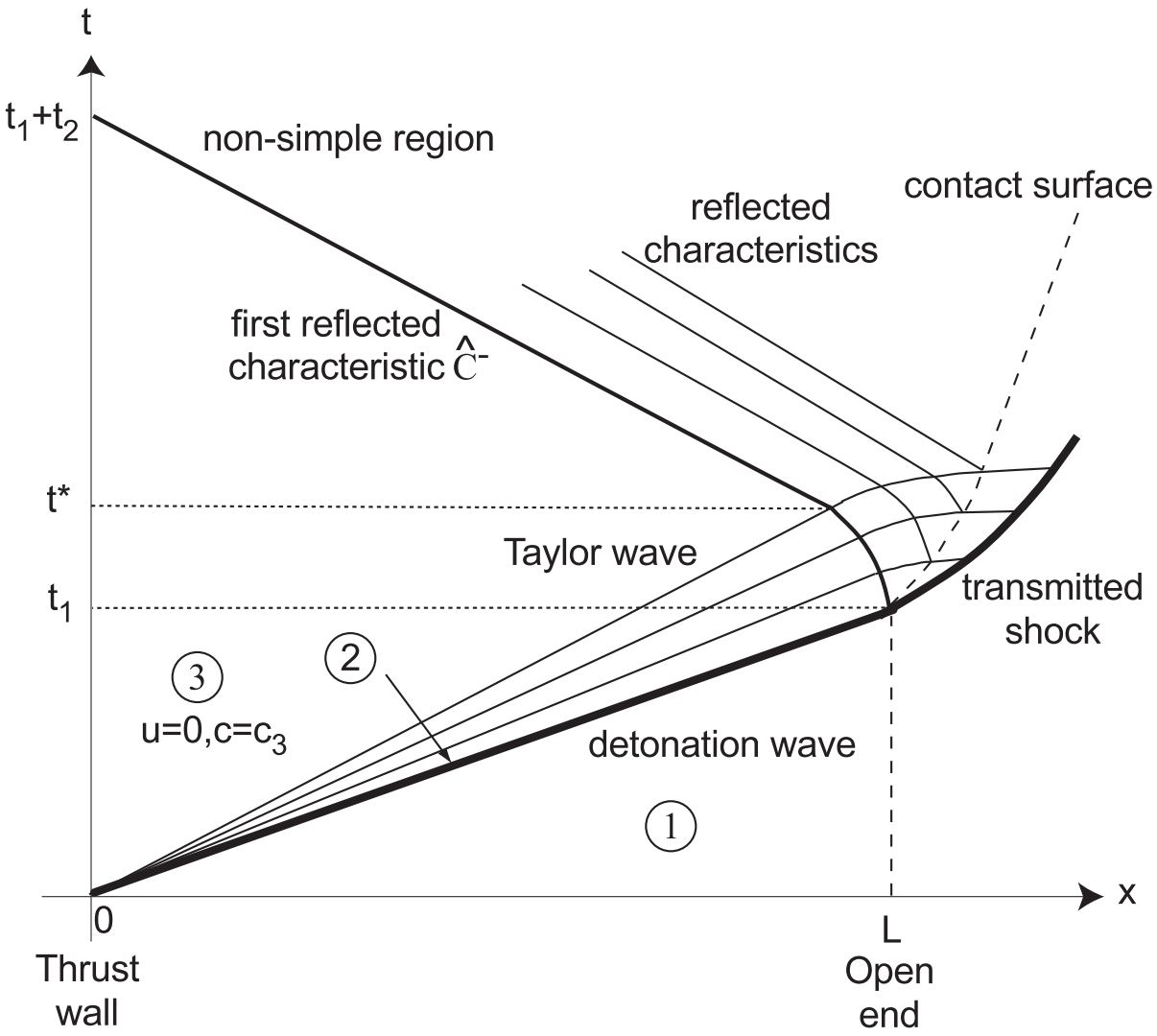

Figure 4: Space-time diagram for detonation wave propagation and interaction with the tube open end.

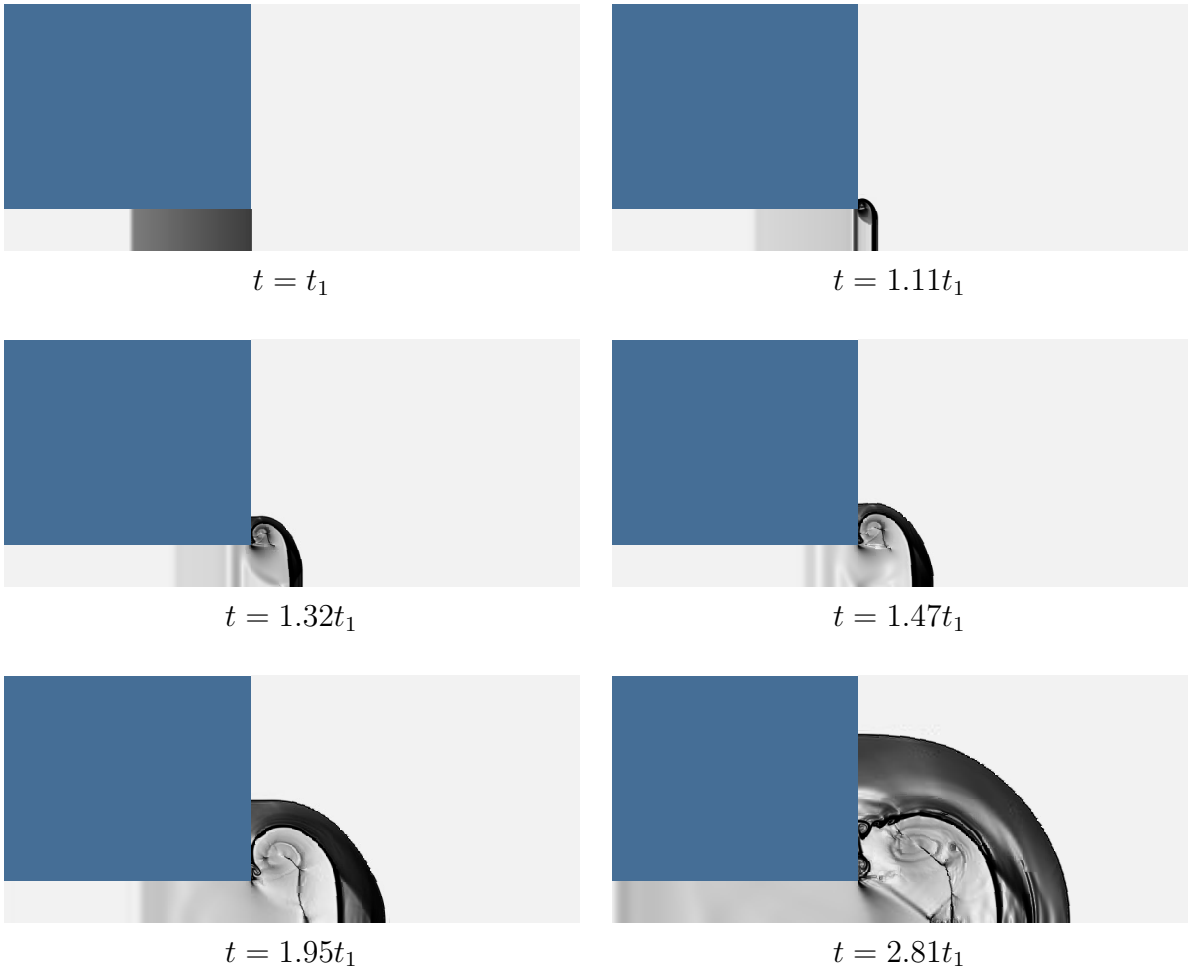

Figure 5: Numerical schlieren images of the exhaust process.

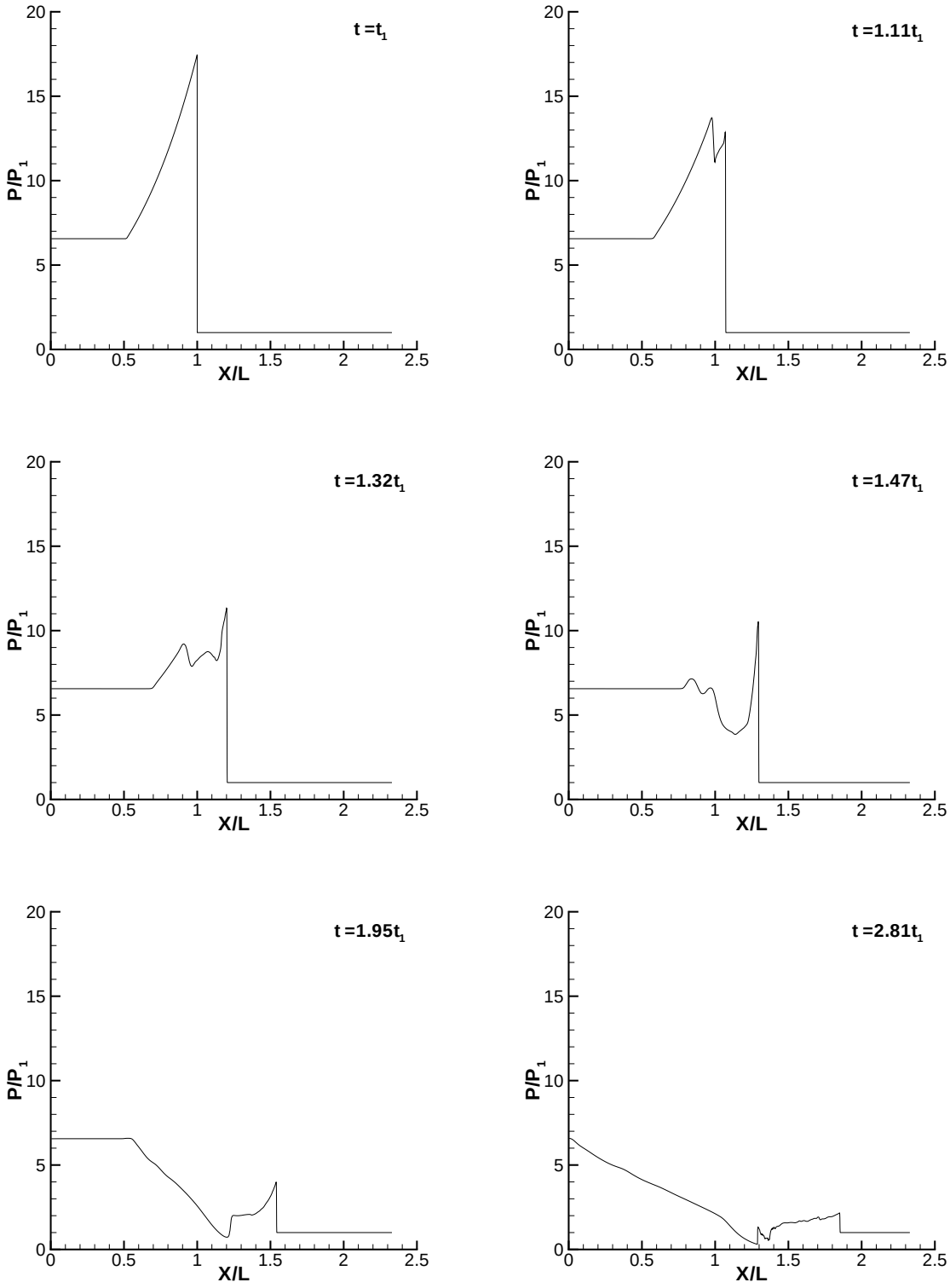

Figure 6: Pressure along the tube centerline from numerical simulation. P_1 is the initial pressure inside and outside the tube.

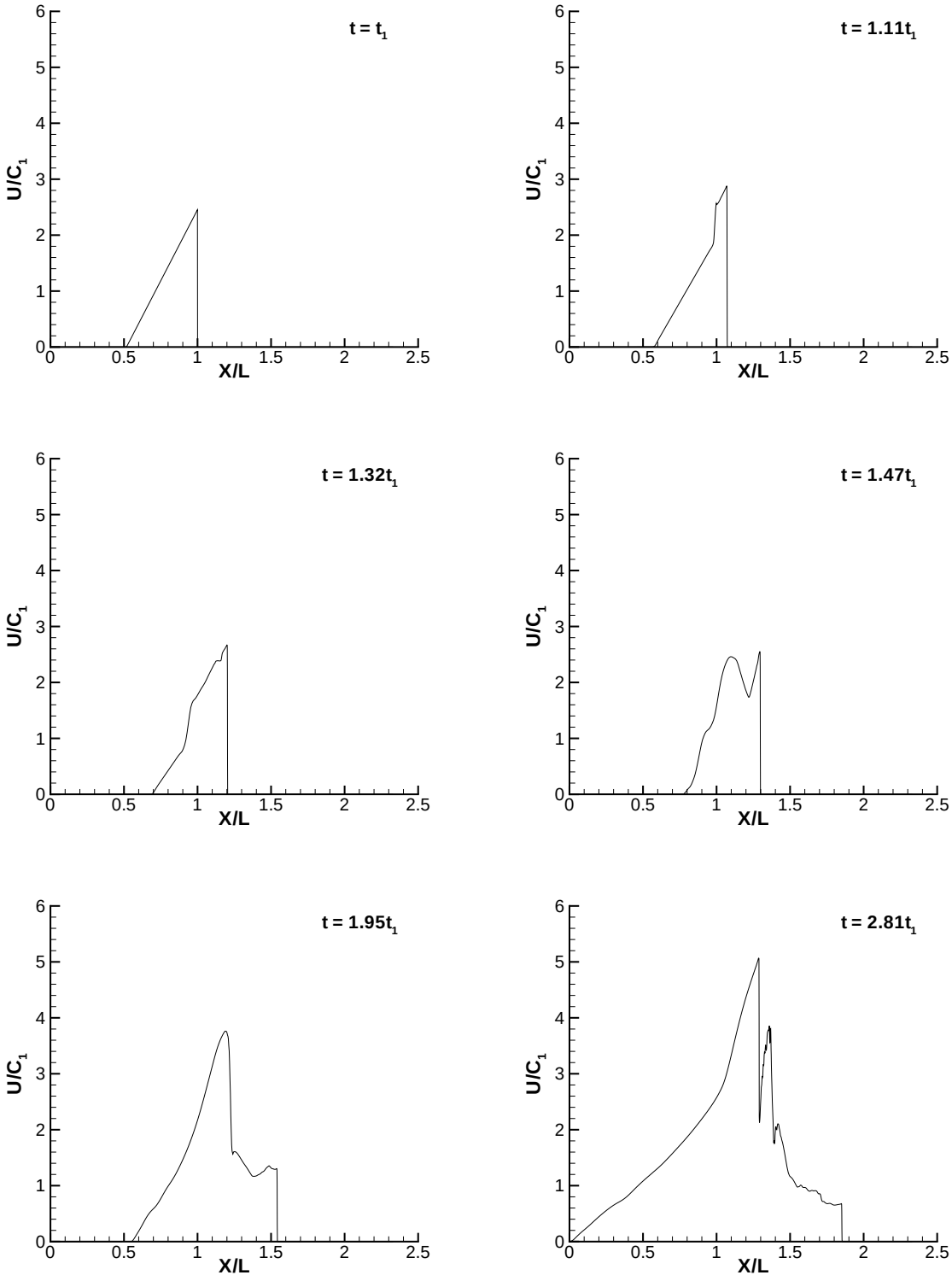

Figure 7: Velocity along the tube centerline from numerical simulation. c_1 is the initial sound speed inside and outside the tube.

The first frame in Figs. 5, 6, and 7 shows the initial condition with the pressure decreasing behind the detonation front from the CJ pressure P_2 to a value P_3 at the end of the Taylor wave. The detonation wave becomes a decaying shock as it exits the tube since the region external to the tube is non-reactive, simulating the surrounding atmosphere of most experimental configurations.

This decaying shock is initially planar but is affected by the expansions originating from the corners of the tube and gradually becomes spherical. The pressure profiles show the decay of the pressure behind the leading shock front with time. A very complex flow structure, involving vortices and secondary shocks, forms behind the leading shock. The fluid just outside the tube accelerates due to the expansion waves coming from the corners of the tube. At the same time the leading shock front exits the tube, a reflected expansion wave is generated and propagates back into the tube, interacting with the Taylor wave. This reflected wave propagates until it reaches the closed end of the tube, decreasing the pressure and accelerating the fluid towards the open end. The exhaust process is characterized by low pressure and high flow velocity downstream of the tube exit. A system of quasi-steady shocks similar to those observed in steady underexpanded supersonic jets, and an unsteady leading shock wave, bring the flow back to atmospheric pressure.

One of the most important points learned from this simulation is that the flow inside the tube is one-dimensional except for within one-to-two diameters of the open end. Another is that the pressure at the open end is unsteady, initially much higher than ambient pressure, and decreasing at intermediate times to lower than ambient before finally reaching equilibrium. Despite the one-dimensional nature of the flow within the tube, it is important to properly simulate the multi-dimensional flow in the vicinity of the exit in order to get a realistic representation of the exhaust process. In our simple model, this is accomplished by using a non-dimensional correlation of the experimental data for this portion of the process.

The normalized pressure P/P_1 at the thrust surface as well as the normalized impulse per unit volume $(I/V)(U_{CJ}/P_1)$ are shown as a function of normalized time t/t_1 in Fig. 8. The impulse per unit volume was computed by integrating the pressure at the thrust surface over time. Note that these plots take into account the initial detonation travel from the closed end to the open end of the tube. The pressure at the thrust surface remains constant until the reflected wave from the tube's open end reaches the thrust surface at time $t_1 + t_2 \approx 2.81t_1$. The final pressure decay process is characterized by a steep pressure decrease and a region of sub-atmospheric pressure. The integrated impulse consequently increases to a maximum before decreasing due to this region of negative overpressure.

4 Impulse model

Our impulse model is based on elementary gas dynamic considerations. We assume one-dimensional, adiabatic flow in a straight unobstructed tube closed at one end and open

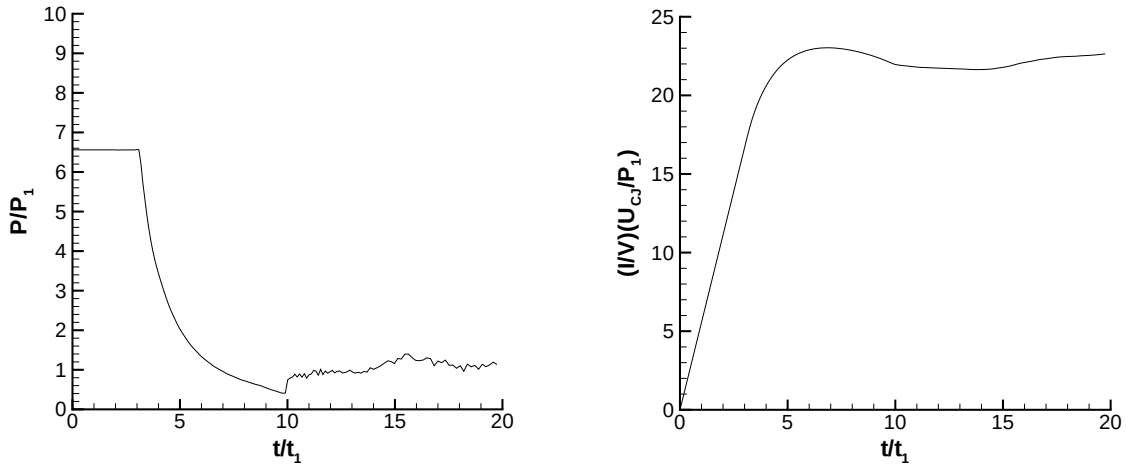

Figure 8: Non-dimensionalized thrust surface pressure and impulse per unit volume as a function of non-dimensionalized time for the numerical simulation.

at the other. The impulse is calculated by considering a control volume around the straight tube as shown in Case b) of Fig. 9. Case a), which represents the usual control volume used for rocket engine analysis, requires the knowledge of the exit pressure P_e, the exhaust velocity u_e and exhaust density ρ_e (or mass flow rate). Case b), the control volume considered in the model, requires only the knowledge of the pressure history at the thrust surface. The impulse is obtained by integrating the pressure differential $P_3 - P_0$ across the thrust surface during one cycle, assuming $P_e = P_0$. This approach is rather limited and is certainly not applicable to air-breathing engines with complex inlets and/or exits. However, it is appropriate for a single tube of constant area and the modeling assumptions eliminate the need for numerical simulations or detailed flow measurements required to evaluate the thrust by integration over the flow properties at the exit plane.

We have made a number of other simplifying assumptions. Non-ideal effects such as viscosity or heat transfer are not considered. The detonation properties are calculated assuming the ideal one-dimensional CJ profile. Real-gas thermodynamics are used to calculate the CJ detonation properties, and classical gas dynamics for a perfect gas are used to model the flow behind the detonation wave. We assume direct instantaneous initiation of planar detonations at the thrust surface. The effect of indirect initiation is discussed in Cooper et al.[1] The model assumes that a reflected expansion wave is generated when the detonation wave reaches the open end, which is generally true, as discussed previously. The model is based on analytical calculations except for the modeling of the pressure decay period, which results from dimensional analysis and experimental observations.

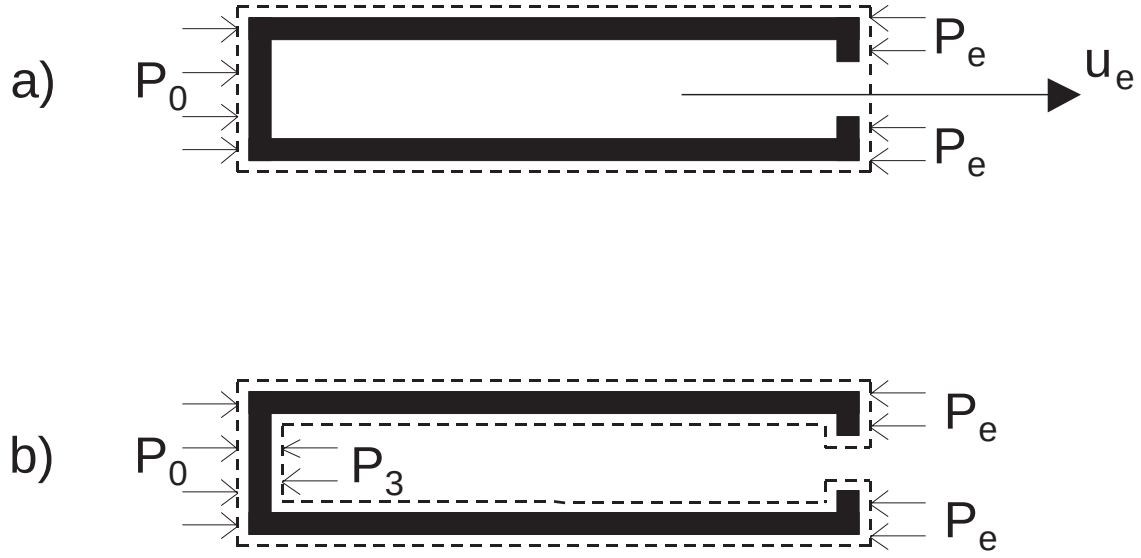

Figure 9: Control volumes a) typically used in rocket engine analysis b) used in our analysis.

4.1 Determination of the impulse

Under our model assumptions, the single-cycle impulse is generated by the pressure differential at the thrust surface. A typical experimental pressure history at the thrust surface recorded by Cooper et al.[1] is given in Fig. 10. When the detonation is initiated, the CJ pressure peak is observed before the pressure decreases to P_3 by the passage of the Taylor wave. The pressure at the thrust surface remains approximately constant until the first reflected characteristic reaches the thrust surface and the reflected expansion wave decreases the pressure. The pressure is decreased below atmospheric for a period of time before ultimately reaching the atmospheric value (Fig. 8).

For our modeling, the pressure-time trace at the thrust surface has been idealized (Fig. 11). The CJ pressure peak is considered to occur during a negligibly short time. The pressure stays constant for a total time $t_1 + t_2$ at pressure P_3. Then the pressure is affected by the reflected expansion and eventually decreases to the atmospheric value.

Using the control volume defined in Case b) of Fig. 9, the single-cycle impulse can be computed as

$$I = A \int_0^\infty \Delta P(t)\, dt \tag{2}$$

where ignition is assumed to occur at $t = 0$. From the idealized pressure-time trace, the impulse can be decomposed into three terms

$$I = A \left[\Delta P_3\, t_1 + \Delta P_3\, t_2 + \int_{t_1+t_2}^\infty \Delta P(t)\, dt \right] . \tag{3}$$

The first term on the right-hand side of Eq. 3 represents the contribution to the impulse associated with the detonation propagation during time $t_1 = L/U_{CJ}$, the second term

is the contribution associated with the time t_2 required for expansion wave propagation from the open end to the thrust surface, and the third term is associated with the pressure decay period.

The time t_2 depends primarily on the length of the tube and the characteristic sound speed c_3 behind the expansion wave which suggests the introduction of a non-dimensional parameter α defined by

$$t_2 = \alpha L/c_3 \ . \tag{4}$$

Dimensional analysis will be used to model the third term on the right-hand side of Eq. 3. The inviscid, compressible flow equations can always be non-dimensionalized using reference parameters, which are a sound speed, a characteristic length, and a reference pressure. Thus, we non-dimensionalize our pressure integral in terms of c_3, L, and P_3

$$\int_{t_1+t_2}^{\infty} \Delta P(t)\, dt = \frac{\Delta P_3 L}{c_3} \int_{\tau_1+\tau_2}^{\infty} \Pi(\tau)\, d\tau \ . \tag{5}$$

The non-dimensional integral on the right-hand side of Eq. 5 can depend only on the remaining non-dimensional parameters of the flow, which are the ratio of specific heats in the products γ, the pressure ratio between the constant pressure region and the initial pressure P_3/P_1, and the non-dimensional energy release during the detonation process q/RT_1. We will define the value of this integral to be β, which has a definite value for a given mixture

$$\beta(\gamma, P_3/P_1, q/RT_1) = \int_{\tau_1+\tau_2}^{\infty} \Pi(\tau)\, d\tau \ . \tag{6}$$

For fuel-air detonations over a limited range of compositions close to stoichiometric, the parameters in Eq. 6 vary by only a modest amount and we will assume that β is approximately constant. This assumption is not crucial in our model and a more realistic expression for β can readily be obtained by numerical simulation. For the present purposes, this assumption is justified by the comparisons with the experimental data shown subsequently.

The dimensional integral on the left-hand side of Eq. 5 can be used to define a characteristic time t_3, which is related to β

$$\int_{t_1+t_2}^{\infty} \Delta P(t)\, dt = \Delta P_3\, t_3 = \Delta P_3 \beta \frac{L}{c_3} \ . \tag{7}$$

In Fig. 11, the time t_3 can be interpreted as the width of the hatched zone representing the equivalent area under the decaying part of the pressure-time trace for $t > t_1 + t_2$. The impulse of Eq. 3 can now be rewritten to include the non-dimensional parameters α and β

$$I = A\Delta P_3 \left[\frac{L}{U_{CJ}} + (\alpha + \beta)\frac{L}{c_3} \right] \ . \tag{8}$$

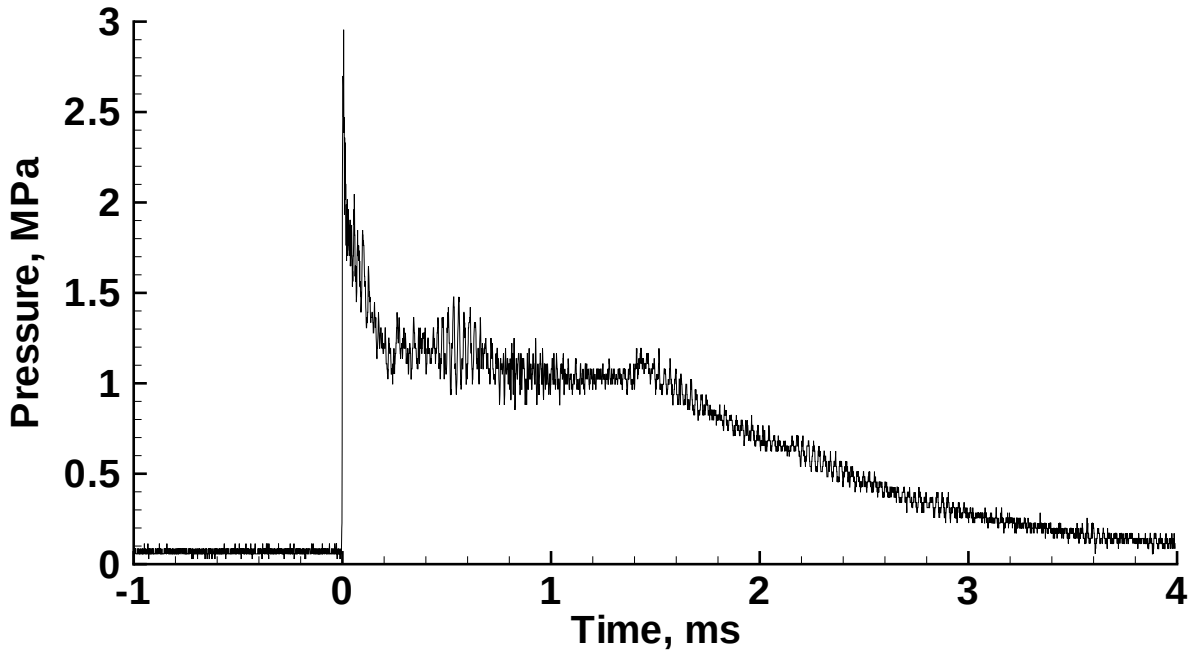

Figure 10: Sample pressure recorded at the thrust surface[1] for a mixture of stoichiometric ethylene-oxygen at 1 bar and 300 K initial conditions.

4.2 Determination of α

We have determined α by considering the interaction of the reflected wave and the Taylor wave. The method of characteristics is used to derive a similarity solution for the leading characteristic of the reflected expansion. This technique will also work for reflected compressions as long as the waves are sufficiently weak.

The derivation of the expression for α begins by considering the network of characteristics within the Taylor wave, shown in Fig. 4. The Riemann invariant J^- is conserved along a C^- characteristic going through the Taylor wave

$$J^- = u_2 - \frac{2c_2}{\gamma - 1} = -\frac{2c_3}{\gamma - 1} = u - \frac{2c}{\gamma - 1} \; . \tag{9}$$

Inside the Taylor wave, the C^+ characteristics are straight lines with a slope given by $x/t = u + c$. Using the Riemann invariant J^- to relate u and c to the flow parameters in state 2, we find that

$$\frac{x}{c_2 t} = \frac{u + c}{c_2} = \frac{u_2}{c_2} + \frac{\gamma + 1}{\gamma - 1}\frac{c}{c_2} - \frac{2}{\gamma - 1} \; . \tag{10}$$

In particular, this method can be used to derive the flow properties in the Taylor wave. The speed of sound is

$$\frac{c}{c_3} = \frac{2}{\gamma + 1} + \frac{\gamma - 1}{\gamma + 1}\frac{x}{c_3 t} \tag{11}$$

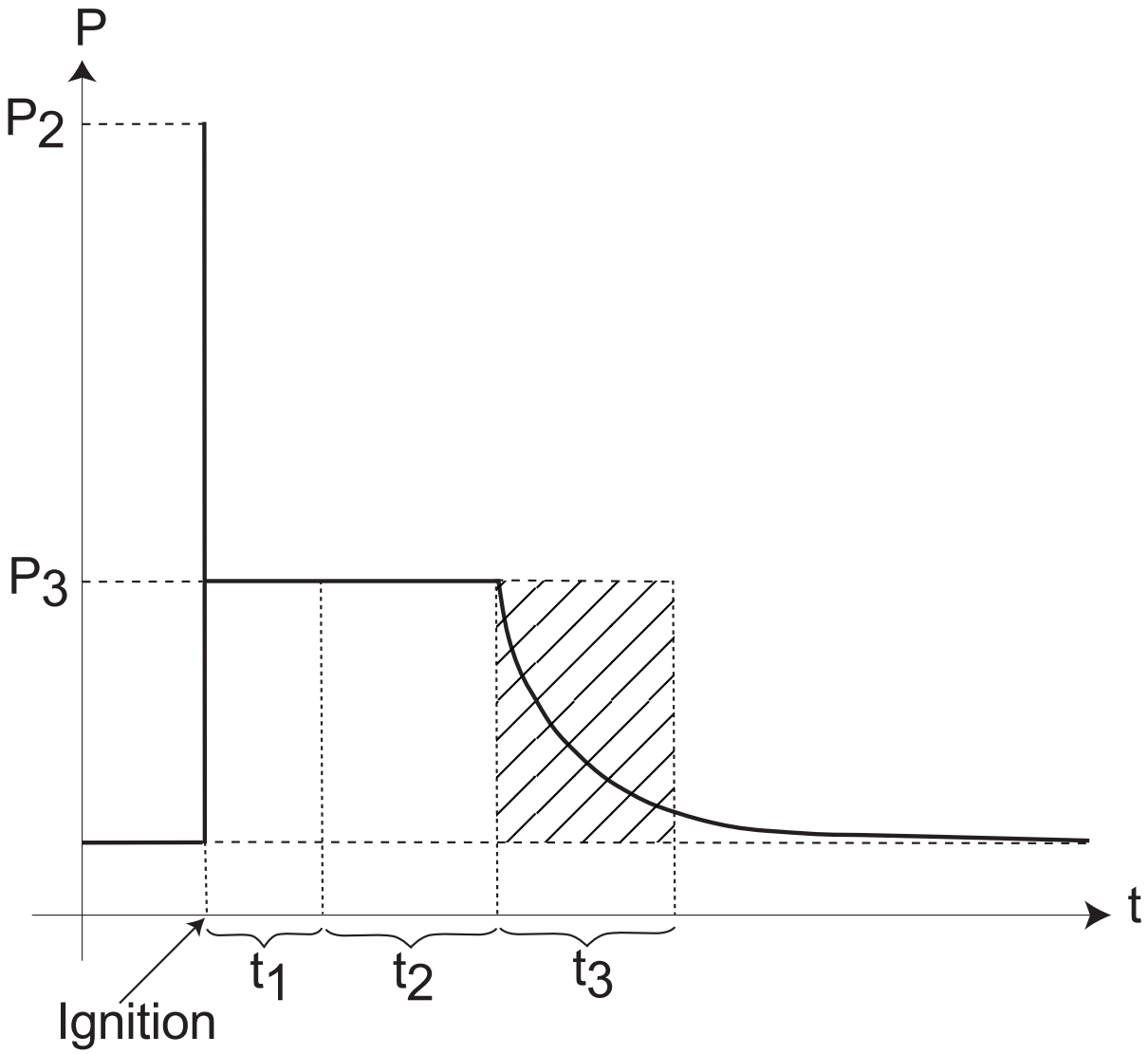

Figure 11: Idealized model of the thrust surface pressure history.

where c_3 is calculated from

$$c_3 = c_2 - \frac{\gamma - 1}{2} u_2 = \frac{\gamma + 1}{2} c_2 - \frac{\gamma - 1}{2} U_{CJ} \ . \tag{12}$$

Equation 11 is valid in the expansion wave, for $c_3 t \leq x \leq U_{CJ} t$. The pressure in the Taylor wave can be computed using the isentropic flow relations.

$$P = P_3 \left(1 - \left(\frac{\gamma - 1}{\gamma + 1} \right) \left[1 - \frac{x}{c_3 t} \right] \right)^{\frac{2\gamma}{\gamma - 1}} \tag{13}$$

Considering the interaction of the reflected expansion wave with the Taylor wave, the

slope of the first reflected characteristic $\hat{C}^-$ can be calculated as

$$\frac{dx}{dt} = u - c = \frac{x}{t} - 2c \; . \tag{14}$$

Substituting for x/t from Eq. 10, we find that

$$\frac{1}{c_2}\frac{dx}{dt} + \frac{2(\gamma-1)}{\gamma+1}\left[\frac{u_2}{c_2} - \frac{2}{\gamma-1} + \frac{3-\gamma}{2(\gamma-1)}\frac{x}{c_2 t}\right] = 0 \; . \tag{15}$$

The form of Eq. 15 suggests the introduction of a similarity variable $\eta = x/c_2 t$. Making the change of variables, we obtain an ordinary differential equation for η

$$t\frac{d\eta}{dt} + \frac{2(\gamma-1)}{\gamma+1}\left[\eta - \frac{u_2}{c_2} + \frac{2}{\gamma-1}\right] = 0 \; . \tag{16}$$

The solution to this equation is

$$\eta(t) = \frac{u_2}{c_2} - \frac{2}{\gamma-1} + \frac{\gamma+1}{\gamma-1}\left(\frac{L}{U_{CJ}t}\right)^{\frac{2(\gamma-1)}{\gamma+1}} \tag{17}$$

where we have used the initial condition $\eta(t_1) = U_{CJ}/c_2$. The last characteristic of the Taylor wave has a slope $x/t = c_3$. Hence, the first reflected characteristic exits the Taylor wave at time t^* determined by $\eta(t^*) = c_3/c_2$. Solving for t^*, we have

$$t^* = \frac{L}{U_{CJ}}\left[\left(\frac{\gamma-1}{\gamma+1}\right)\left(\frac{c_3 - u_2}{c_2} + \frac{2}{\gamma-1}\right)\right]^{-\frac{\gamma+1}{2(\gamma-1)}} \; . \tag{18}$$

For $t^* < t < t_1 + t_2$, the characteristic $\hat{C}^-$ propagates at constant velocity equal to the sound speed c_3. From the geometry of the characteristic network shown in Fig. 4, $\hat{C}^-$ reaches the thrust surface at time $t_1 + t_2 = 2t^*$. Thus, $t_2 = 2t^* - t_1 = \alpha L/c_3$. Solving for α, we obtain

$$\alpha = \frac{c_3}{U_{CJ}}\left[2\left(\frac{\gamma-1}{\gamma+1}\left[\frac{c_3 - u_2}{c_2} + \frac{2}{\gamma-1}\right]\right)^{-\frac{\gamma+1}{2(\gamma-1)}} - 1\right] \; . \tag{19}$$

The quantities involved in this expression essentially depend on two non-dimensional parameters: γ and the detonation Mach number $M_{CJ} = U_{CJ}/c_1$. These can either be computed numerically with realistic thermochemistry or else analytically using the ideal gas one-γ model for a CJ detonation. Numerical evaluations of this expression for typical fuel-air detonations show that $\alpha \approx 1.1$ for a wide range of fuel and compositions. Using the one-γ model, the resulting expression for $\alpha(\gamma, M_{CJ})$ is

$$\frac{1}{2}\left(1 + \frac{1}{M_{CJ}^2}\right)\left(2\left[\frac{\gamma-1}{\gamma+1}\left(\frac{\gamma+3}{2} + \frac{2}{\gamma-1} - \frac{(\gamma+1)^2}{2}\quad\frac{M_{CJ}^2}{1+\gamma M_{CJ}^2}\right)\right]^{-\frac{\gamma+1}{2(\gamma-1)}} - 1\right) \; . \tag{20}$$

4.3 Determination of β

The region between the first reflected characteristic and the contact surface in Fig. 4 is a non-simple region created by the interaction of the reflected expansion wave with the Taylor wave. The multi-dimensional flow behind the diffracting shock front also plays a significant role in determining the pressure in this region. For these reasons, it is impossible to derive an analytical solution for the parameter β. It is, however, possible to use experimental data and Eq. 6 to calculate β. We considered data from Zitoun and Desbordes[12], who carried out detonation tube experiments and measured impulse using tubes of different lengths. They showed that the impulse scales with the length of the tube, as expected from Eq. 8.

Zitoun and Desbordes used an exploding wire to directly initiate detonations, which is representative of the idealized conditions of our model. They determined impulse for stoichiometric ethylene-oxygen mixtures by integrating the pressure differential at the thrust surface. The analysis of their pressure-time traces reveals that the overpressure, after being roughly constant for a certain period of time, decreases and becomes negative before returning to zero. The integration of the decaying part of the pressure-time trace was carried out up to a time late enough (typically greater than $20t_1$) to ensure that the overpressure has returned to zero. This integration gave a value of $\beta = 0.53$.

5 Validation of the model

The model was validated against experimental data and comparisons were made in terms of impulse per unit volume and specific impulse. The impulse per unit volume is defined as

$$I_V = I/V \ . \tag{21}$$

The mixture-based specific impulse I_{sp} is defined as

$$I_{sp} = \frac{I}{\rho_1 V g} = \frac{I_V}{\rho_1 g} = \frac{I}{Mg} \ . \tag{22}$$

The fuel-based specific impulse I_{spf} is defined with respect to the fuel mass instead of the mixture mass

$$I_{spf} = \frac{I}{\rho_1 X_F V g} = \frac{I_{sp}}{X_F} = \frac{I}{M_f g} \ . \tag{23}$$

5.1 Comparisons with single-cycle experiments

The calculation of the parameter α was validated by comparing the arrival time of the reflected expansion wave from experimental pressure histories at the thrust surface with the time calculated from the similarity solution. For a mixture of stoichiometric ethylene-air at 1 bar initial pressure, the time in an experimental pressure history [1] between detonation initiation and the arrival of the reflected expansion wave was 1.43 ms from a 1.016 m long tube. The corresponding calculated time was 1.39 ms, within 3% of the

experimental value. Similarly, comparing with data[12] for a tube of length 0.225 m, excellent agreement (within 1%) is obtained between our calculated value (313 μs) and experiment (315 μs).

The value of β was also computed using data from our experiments[1] with stoichiometric ethylene-oxygen. Because these experiments used indirect detonation initiation (DDT), we were able to compare with only two cases using an unobstructed tube and an initial pressure of 1 bar for which there was very rapid onset of detonation. These cases correspond to values of β equal to 0.55 and 0.66. Note that these values are sensitive to the time at which the integration is started. We computed this time using our theoretical values of t_1 and t_2.

Model predictions of impulse per unit volume were compared with data from Cooper et al.[1]. Direct experimental impulse measurements were obtained with a ballistic pendulum and detonation initiation was obtained via DDT. Obstacles were mounted inside the detonation tube in some of the experiments in order to enhance DDT. A correlation plot showing the impulse per unit volume obtained with the model versus the experimental values is displayed in Fig. 12. The values displayed here cover experiments with four different fuels (hydrogen, acetylene, ethylene, and propane) over a range of initial conditions and compositions. The solid line represents perfect correlation between the experimental data and the model. The filled symbols represent the data for unobstructed tubes, while the open symbols correspond to cases for which obstacles were used in the detonation tube.

The analytical model predictions were close to the experimental values of the impulse as shown on Fig. 12. The model assumes direct initiation of detonation, so it does not take into account any DDT phenomenon. The agreement is better for cases with high initial pressure and no nitrogen dilution, since the DDT time (time it takes the initial flame to transition to a detonation) is the shortest for these mixtures. For the unobstructed tube experiments, the model systematically underpredicts the impulse by 5% to 15%, except for the acetylene case, where it is about 25% too low. When obstacles are used, the experimental values are up to 25% lower than the model predictions. In general, the discrepancy between model and experiment is less than or equal to $\pm$15%. This conclusion is supported in Fig. 12 by the $\pm$15% deviation lines which encompass the experimental data. The lower experimental values for cases with obstacles are apparently caused by the additional form drag associated with the separated flow over the obstacles[1].

The model parameters are relatively constant, $1.07 < \alpha < 1.13$ and $0.53 < \beta < 0.66$, for all the mixtures studied here. A reasonable estimate for α is 1.1 and for β is 0.53. The ratio U_{CJ}/c_3 for fuel-oxygen-nitrogen mixtures is approximately 2. For quick estimates of the impulse, these values can be used in Eq. 8 to obtain the approximate model prediction formula

$$I = 4.3\frac{\Delta P_3}{U_{CJ}}AL = 4.3\frac{\Delta P_3}{U_{CJ}}V \ . \tag{24}$$

The approximate formula reproduces the exact expressions within 2.5%.

Zitoun and Desbordes[12] calculated the single-cycle specific impulse for various reactive mixtures based on a formula developed from their experimental data for ethylene-

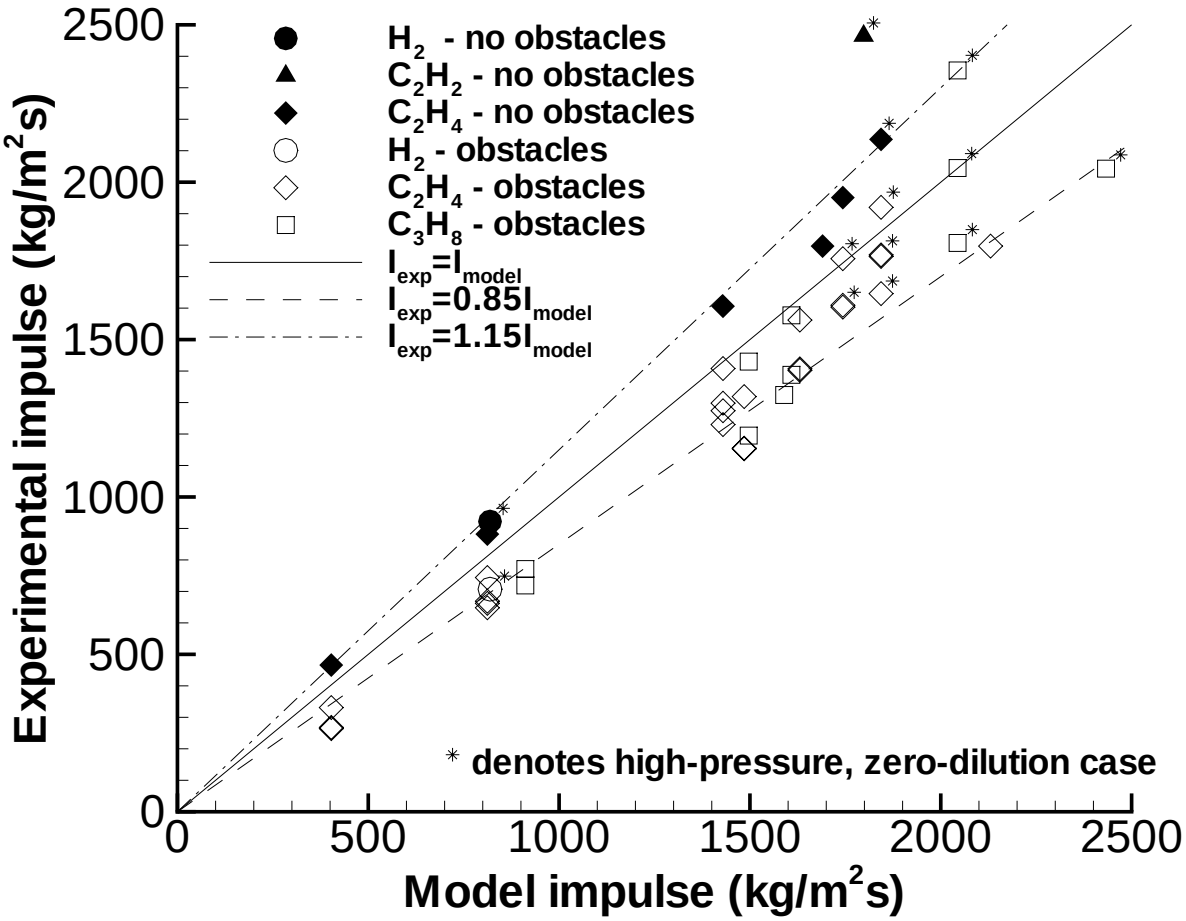

Figure 12: Model predictions versus experimental data for the impulse per unit volume. Filled symbols represent data for unobstructed tubes, whereas open symbols show data for cases in which obstacles were used. Lines corresponding to +15% and -15% deviation from the model values are also shown. * symbols denote high-pressure (higher than 0.8 bar), zero-dilution cases.

oxygen mixtures: $I_{sp} = K\Delta P_3/(g\rho_1 U_{CJ})$. The coefficient K is estimated to be 5.4 in their study, whereas we obtained an estimate of 4.3. This accounts for the difference in the specific impulse results presented in Table 1. The present analytical model impulse is about 20% lower than Zitoun's predictions. This difference can be explained by the fact that Zitoun and Desbordes[12] considered only the region of positive overpressure, which extends to about $9t_1$, in their integration of the pressure differential. They based this on the assumption that the following region of negative overpressure would be used for the self-aspiration of air in a multi-cycle air-breathing application. However, since we were interested in comparing with ballistic pendulum measurements, we performed the integration until the overpressure was back to zero, which occurs at about $20t_1$. The region of negative overpressure between 9 and $20t_1$ results in an impulse decrease. If we calculate the value of β by limiting the integration to the time of positive overpressure,

we obtain a value of $K = 4.8$.

Mixture	Model I_{sp}	Zitoun and Desbordes[12]
C_2H_4+$3O_2$	151.1	200
C_2H_4+$3(O_2$+$3.76N_2)$	117.3	142
C_2H_2+$2.5O_2$	150.9	203
C_2H_2+$2.5(O_2$+$3.76N_2)$	120.6	147
H_2+$0.5O_2$	172.9	226
H_2+$0.5(O_2$+$3.76N_2)$	123.7	149

Table 1: Comparison of the model predictions for the mixture-based specific impulse.

5.2 Comparisons with multi-cycle experiments

Calculations of specific impulse and thrust were compared to experimental data from Schauer et al.[2, 3]. Their facility consisted of a 50.8 mm diameter by 914.4 mm long tube mounted on a damped thrust stand. Impulse and thrust measurements were made in hydrogen-air[2] and propane-air[3] mixtures with varying equivalence ratio. Data were collected during continuous multi-cycle operation and the thrust was averaged over many cycles. To compare with our model predictions, we assume multi-cycle operation is equivalent to a sequence of ideal single cycles. In multi-cycle operation, a portion of the cycle time is used to purge the tube and re-fill with reactants. The expulsion of gas from the tube can result in a contribution to the impulse which is not accounted for in our simple model. To estimate the magnitude of the impulse during refilling, we assumed that the detonation and exhaust phase had a duration of about $10t_1$ and that the remaining portion of the cycle is used for the purging and filling processes. We found that the contribution of the purge and fill portion to the thrust was less than their stated experimental uncertainty of 6%[2].

Comparisons of specific impulse are presented in Fig. 13 for hydrogen-air[2] and in Fig. 14 for propane-air[3]. For comparison, predictions and one single-cycle measurement for hydrogen-oxygen are shown in Fig. 13. Two sets of data are shown for propane: data labeled "det" are from runs in which the average detonation wave velocity was about 80% of the CJ value, and data labeled "no det?" are from runs in which detonations were unstable or intermittent. The impulse model predictions are within 8% of the experimental data for hydrogen-air at $\phi > 0.8$, and within 15% for stable propane-air cases. Figure 13 also includes an experimental hydrogen-oxygen single-cycle data point from our own experiments[1]. The vertical dashed line on Fig. 13 denotes a limit of the model validity. For richer mixtures, a reflected shock is calculated (Figs. 2, 3). The fact that the model still correctly predicts the impulse beyond this limit suggests that the reflected shock is weak and does not significantly affect the integrated pressure. Indeed, a ballistic pendulum experiment [1] carried out with hydrogen-oxygen resulted

in the directly measured impulse being within 10% of the value predicted by the model (Fig. 13). Figs. 13 and 14 also include ±15% deviation lines from the model predictions.

In Fig. 14, the significantly lower impulse of the experimental point at $\phi = 0.59$ in propane mixtures is certainly due to cell size effects. At the lower equivalence ratios, the cell size[27] of propane-air (152 mm at $\phi = 0.74$) approaches π times the diameter of the tube which is the nominal limit for stable detonation propagation [28, 29].

In the case of hydrogen-air, Fig. 13, the cell size[27] at $\phi = 0.75$ is 21 mm so the decrease in the experimental impulse data at low equivalence ratios can not be explained by cell size effects. Following the work of Dorofeev et al.[30], the magnitude of the expansion ratio was examined for these mixtures. However, calculations for lean hydrogen-air showed that the expansion ratio is always higher than the critical value defined [30] for hydrogen mixtures. Instead, the results may be explained by the transition distance of the mixtures. Dorofeev et al.[31] studied the effect of scale on the onset of detonations. They proposed and validated a criterion for successful transition to detonation: $\mathcal{L} > 7\lambda$, where $\mathcal{L}$ is the characteristic geometrical size (defined to account for the presence of obstacles) and λ the cell size of the mixture. Schauer et al.[2] used a 45.7 mm pitch Shchelkin spiral constructed of 4.8 mm diameter wire to initiate detonations in their detonation tube. As defined by Dorofeev[31], this results in a characteristic geometrical size of 257 mm, comparable to $7\lambda = 217$ mm for a value of $\phi = 0.67$. The cell size increases with decreasing equivalence ratio for lean mixtures, so mixtures with equivalence ratios smaller than 0.67 will not transition to detonation within the spiral or possibly even the tube itself. This is consistent with the data shown on Fig. 13; hydrogen-air tests with $\phi \leq 0.67$ have experimental specific impulse values significantly lower than the model prediction. Similar reductions in I_{sp} were also observed by Cooper et al.[1] in single-cycle tests of propane-oxygen-nitrogen and ethylene-oxygen-nitrogen mixtures with greater than a critical amount of nitrogen dilution.

Average thrust for multi-cycle operation can be calculated from our single-cycle impulse model predictions, assuming a periodic sequence of individual pulses that do not interact. For a given single-cycle performance and tube size, the average thrust is proportional to the frequency f

$$T = I_V V f \ . \tag{25}$$

Schauer et al.[2] measured the average thrust in multi-cycle operation with hydrogen-air over a range of frequencies between 14 and 40 Hz and verified the linear dependence on frequency. Although this simple model suggests that thrust can be increased indefinitely by increasing the cycle frequency, there are obvious physical constraints[32] that limit the maximum frequency for given size tube. The maximum cycle frequency is inversely proportional to the sum of the minimum detonation, exhaust, fill, and purge times. The purge and fill times are typically much longer than the detonation and exhaust time and therefore are the limiting factors in determining the maximum cycle frequency.

Fig. 15 compares measurements[2] and model predictions for operation at a fixed frequency of 16 Hz. The computation of the thrust with the model is within 4% of the experimental data for $\phi > 0.8$. The discrepancies at low equivalence ratios are due to the increased transition distance discussed above.

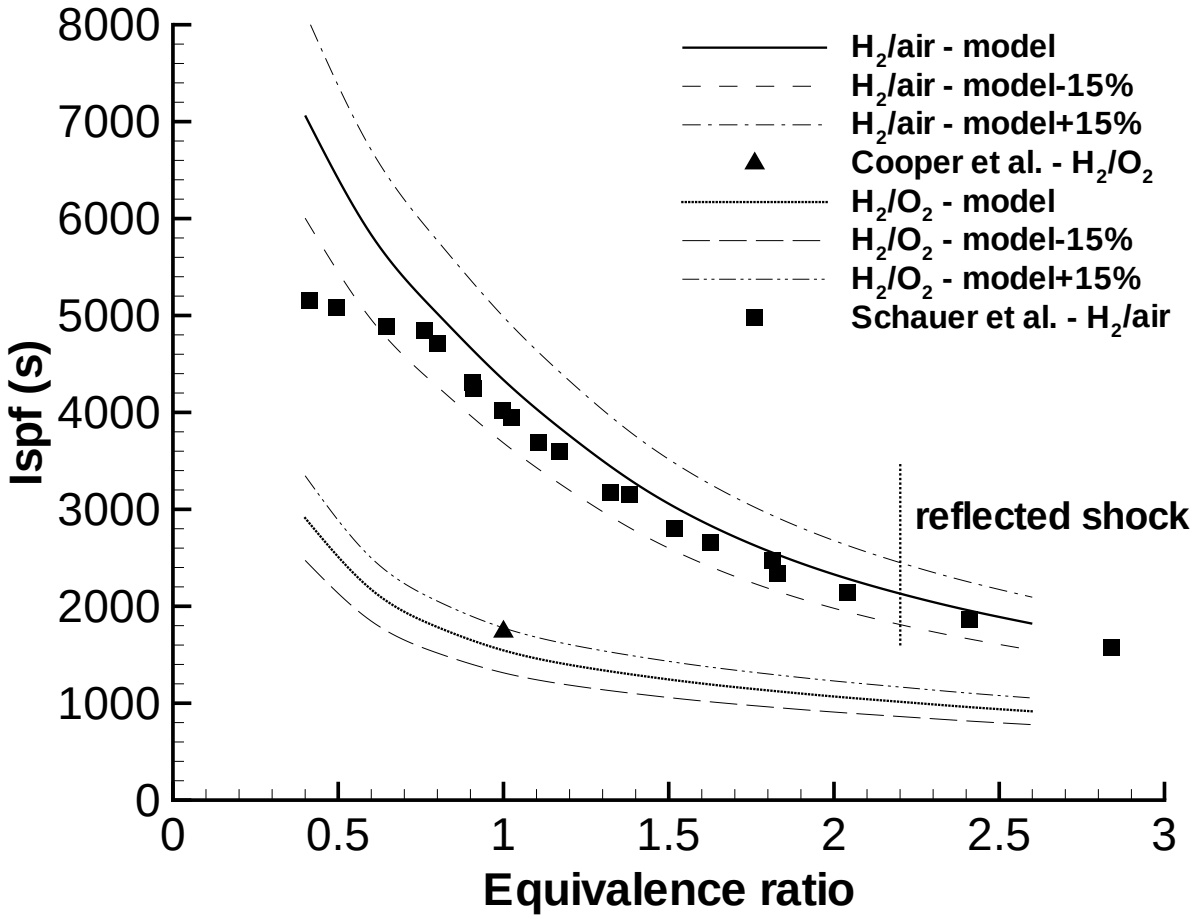

Figure 13: Comparison of specific impulse between model predictions and experimental data for hydrogen-air[2] with varying equivalence ratio and stoichiometric hydrogen-oxygen[1]. Nominal initial conditions are $P_1 = 1$ bar, $T_1 = 300$ K. Lines corresponding to +15% and -15% deviation from the model values are also shown.

Comparisons with numerical simulations

Data from the numerical simulation presented previously in this paper were used to compute the impulse per unit volume. The pressure at the thrust surface (Fig. 8) was integrated over time to obtain the impulse per unit area. Since the simulation was carried out for non-reactive flow and started as the detonation front exited the tube, the initial time corresponding to the detonation travel from the closed end to the open end of the tube was not simulated but was taken to be L/U_{CJ}. The integration was performed up to a time corresponding to $20t_1$ and the impulse per unit volume was

$$I/V = 22.6\frac{P_1}{U_{CJ}} \, . \tag{26}$$

This result is within 0.1% of the approximate model formula of Eq. 24. The simulation results are valid only for cases where the initial pressure P_1 is equal to the pressure

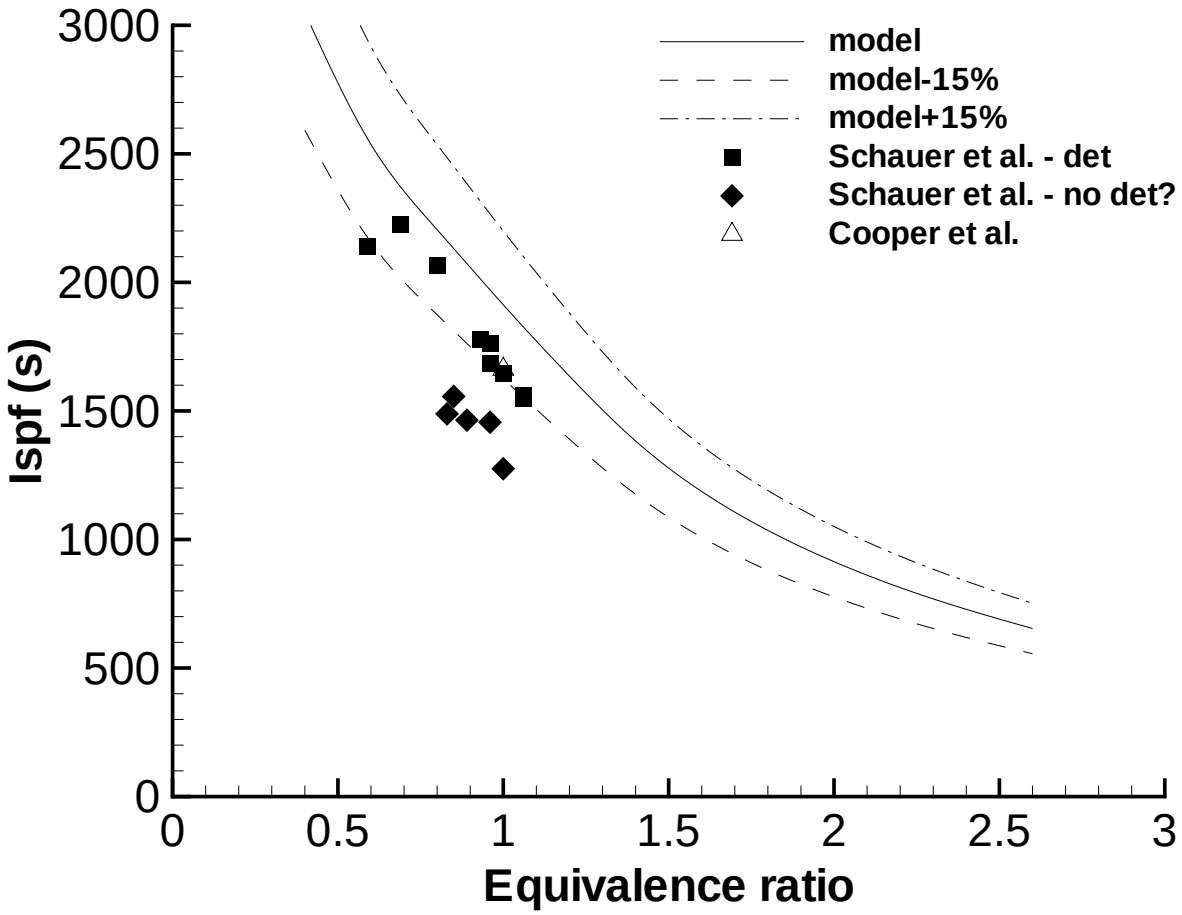

Figure 14: Comparison of specific impulse between model predictions and experimental data [1, 3] for propane-air with varying equivalence ratio. Nominal initial conditions are $P_1 = 1$ bar, $T_1 = 300$ K. Lines corresponding to +15% and -15% deviation from the model values are also shown.

outside the detonation tube P_0.

Comparisons with numerical computations of specific impulse by other researchers can also be made. Numerical simulations are very sensitive to the specification of the outflow boundary condition at the open end, and the numerical results vary widely when different types of boundary conditions are used. Sterling et al.[5] obtained an average value of 5151 s for the fuel-based specific impulse of a stoichiometric hydrogen-air mixture in a multi-cycle simulation using a constant pressure boundary condition. Bussing et al.[7] obtained a range of values of 7500-8000 s. Other predictions by Cambier and Tegner[8], including a correction for the effect of the initiation process, gave values between 3000 and 3800 s. More recently, Kailasanath and Patnaik [9] tried to reconcile these different studies for hydrogen-air by highlighting the effect of the outflow boundary condition. They varied the pressure relaxation rate at the exit and obtained a range of values from 4850 s (constant pressure case) to 7930 s (gradual relaxation case). Our analytical model

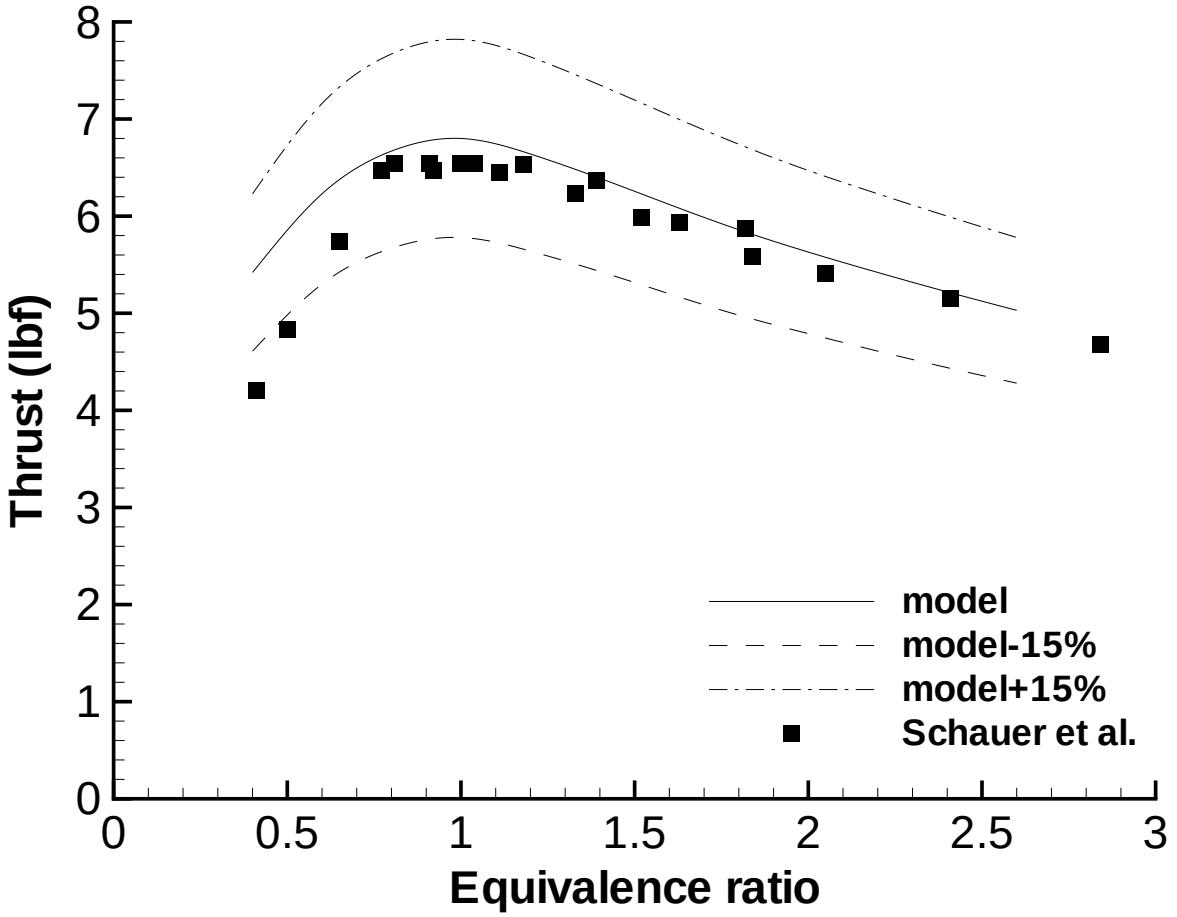

Figure 15: Thrust prediction for a 50.8 mm diameter by 914.4 mm long hydrogen-air PDE operated at 16 Hz. Comparison with experimental data of Schauer et al.[2]. Nominal initial conditions are $P_1 = 1$ bar, $T_1 = 300$ K. Lines corresponding to +15% and -15% deviation from the model values are also shown.

predicts 4335 s for the fuel-based specific impulse of stoichiometric hydrogen-air and the experimental value of Schauer et al. [2] is 4024 s.

6 Impulse scaling relationships

From Eq. 24, the impulse can be written as

$$I = K \cdot V \frac{\Delta P_3}{U_{CJ}} \tag{27}$$

where K has a weak dependence on the properties of the mixture, $K(\gamma, q/RT_1)$. For the purposes of predicting how the impulse depends on the mixture properties and tube size, the principal dependencies are explicitly given in Eq. 27 with K = constant. The

dependence of impulse on the mixture properties comes in through the thermodynamic quantities U_{CJ} and ΔP_3. The CJ velocity is a function of composition only and independent of initial pressure as long as it is not so low that dissociation of the detonation products is significant. For the case of $P_1 = P_0$, the impulse can be written

$$I = K \frac{V P_1}{U_{CJ}} \left(\frac{P_2}{P_1} \frac{P_3}{P_2} - 1 \right) . \tag{28}$$

From the gas dynamic considerations given in the previous section, Eq. 13 implies that

$$\frac{P_3}{P_2} = \left[1 - \left(\frac{\gamma - 1}{\gamma + 1} \right) \left(1 - \frac{U_{CJ}}{c_3} \right) \right]^{-\frac{2\gamma}{\gamma - 1}} \tag{29}$$

Equilibrium computations with realistic thermochemistry indicate that $U_{CJ}/c_3 \approx 2$ and $0.324 \leq P_3/P_2 \leq 0.375$ with an average value of 0.35 for a wide range of compositions and initial conditions. Under these conditions, the pressure ratio is approximately constant

$$\frac{P_3}{P_2} \approx \left(\frac{2\gamma}{\gamma + 1} \right)^{-\frac{2\gamma}{\gamma - 1}} . \tag{30}$$

The approximate value of Eq. 30 is within 7% of the exact value of Eq. 29 for a range of mixtures including hydrogen, acetylene, ethylene, propane, and JP10 with air and oxygen varying nitrogen dilution (0 to 60%) at initial conditions $P_1 = 1$ bar and $T_1 = 300$ K. This indicates that the impulse will be mainly dependent on the CJ conditions and the total volume of explosive mixture

$$I \propto \frac{V P_2}{U_{CJ}} . \tag{31}$$

Values of the CJ parameters and model impulses for several stoichiometric fuel-oxygen-nitrogen mixtures are given in Table 2.

Dependence of impulse on energy content

In order to explicitly compute the dependence of impulse on energy content, the approximate one-γ model of a detonation can be used. The CJ Mach number can be written

$$M_{CJ} = \sqrt{1 + \mathcal{H}} + \sqrt{\mathcal{H}} \qquad \text{where} \qquad \mathcal{H} = \frac{\gamma^2 - 1}{2\gamma} \frac{q}{R T_1} . \tag{32}$$

The effective specific energy release q is generally less than the actual specific heat of combustion q_c due to the effects of dissociation, specific heat dependence on temperature, and the difference in average molar mass of reactants and products. Values of γ, q_c, and q are given for selected fuel-oxygen-nitrogen mixtures in Table 2 and the computation of q is discussed subsequently. For large values of the parameter $\mathcal{H}$, we can approximate the CJ velocity as

$$M_{CJ} \approx 2\sqrt{\mathcal{H}} \qquad \text{or} \qquad U_{CJ} \approx \sqrt{2(\gamma^2 - 1) q} . \tag{33}$$

Mixture	q_c (MJ/kg)	γ	P_2 (bar)	T_2 (K)	U_{CJ} (m/s)	M_{CJ}	I_{sp} (s)	q (MJ/kg)
H_2-O_2	13.29	1.223	18.72	3679	2840	5.26	172.9	6.59
H_2-O_2-20% N_2	8.39	1.189	17.98	3501	2474	5.16	155.4	5.80
H_2-O_2-40% N_2	5.20	1.170	16.95	3256	2187	5.01	138.7	4.98
H_2-air	3.39	1.175	15.51	2948	1971	4.81	123.7	3.92
C_2H_2-O_2	11.82	1.263	33.63	4209	2424	7.32	150.9	4.50
C_2H_2-O_2-20% N_2	9.60	1.238	30.17	4051	2311	6.89	146.0	4.37
C_2H_2-O_2-40% N_2	7.31	1.212	26.53	3836	2181	6.42	139.8	4.32
C_2H_2-O_2-60% N_2	4.95	1.186	22.46	3505	2021	5.87	130.6	4.09
C_2H_2-air	3.39	1.179	19.20	3147	1879	5.42	120.6	3.60
C_2H_4-O_2	10.67	1.236	33.27	3935	2376	7.24	151.0	4.76
C_2H_4-O_2-20% N_2	8.70	1.210	29.57	3783	2258	6.79	145.7	4.72
C_2H_4-O_2-40% N_2	6.66	1.187	25.89	3589	2132	6.32	139.1	4.60
C_2H_4-O_2-60% N_2	4.53	1.169	21.82	3291	1977	5.77	129.3	4.26
C_2H_4-air	3.01	1.172	18.25	2926	1825	5.27	117.0	3.51
C_3H_8-O_2	10.04	1.220	36.04	3826	2360	7.67	152.7	5.20
C_3H_8-O_2-20% N_2	8.33	1.199	31.73	3688	2251	7.14	147.3	5.10
C_3H_8-O_2-40% N_2	6.48	1.181	27.45	3513	2131	6.58	140.4	4.90
C_3H_8-O_2-60% N_2	4.49	1.166	22.79	3239	1980	5.95	130.3	4.45
C_3H_8-air	2.80	1.174	18.15	2823	1801	5.29	115.4	3.41
JP10-O_2	9.83	1.226	38.89	3899	2294	7.99	148.4	4.84
JP10-O_2-20% N_2	8.34	1.205	34.00	3759	2204	7.41	144.1	4.80
JP10-O_2-40% N_2	6.65	1.186	29.18	3585	2103	6.81	138.5	4.67
JP10-O_2-60% N_2	4.73	1.169	24.06	3316	1972	6.12	130.1	4.37
JP10-air	2.79	1.173	18.40	2843	1784	5.32	114.6	3.38

Table 2: Detonation CJ parameters and computed impulse for selected stoichiometric mixtures at 1 bar initial pressure and 300 K initial temperature.

The pressure ratio $\Delta P_3/P_1$ is also a function of composition only as long as the initial pressure is sufficiently high. The one-γ model can be used to compute the CJ pressure as

$$\frac{P_2}{P_1} = \frac{\gamma M_{CJ}^2 + 1}{\gamma + 1} \ . \tag{34}$$

For large values of the parameter $\mathcal{H}$, equivalent to large M_{CJ}, this can be approximated as

$$P_2 \approx \frac{1}{\gamma + 1} \rho_1 U_{CJ}^2 \ . \tag{35}$$

In the same spirit, we can approximate, assuming $P_1 = P_0$,

$$\Delta P_3/P_1 = \frac{P_2}{P_1}\frac{P_3}{P_2} - 1 \approx \frac{P_2}{P_1}\frac{P_3}{P_2} \tag{36}$$

and the impulse can be approximated as

$$I \approx \frac{1}{\gamma + 1} M U_{CJ} K \frac{P_3}{P_2} \ . \tag{37}$$

Using the approximation of Eq. 33, this can be written

$$I \approx M\sqrt{q}\left[\sqrt{2\frac{\gamma - 1}{\gamma + 1}} K \frac{P_3}{P_2}\right] \ . \tag{38}$$

The term in the square brackets is only weakly dependent on the mixture composition. Using Eq. 30, the impulse can be approximated as

$$I \approx M\sqrt{q} K \sqrt{2\frac{\gamma - 1}{\gamma + 1}} \left(\frac{2\gamma}{\gamma + 1}\right)^{-\frac{2\gamma}{\gamma - 1}} \ . \tag{39}$$

This expression indicates that the impulse is directly proportional to the product of the total mass of explosive mixture in the tube and the square root of the specific energy content of the mixture.

$$I \propto M\sqrt{q} \tag{40}$$

Dependence of impulse on initial pressure

At fixed composition and initial temperature, the values of q, γ, and R are constant. Equilibrium computations with realistic thermochemistry show that for high enough initial pressures, U_{CJ}, P_3/P_2, and P_2/P_1 are essentially independent of initial pressure. From Eq. 39, we conclude that the impulse (or impulse per unit volume) is directly proportional to initial pressure under these conditions, since $M = \rho_1 V = P_1 V/RT_1$.

$$I \propto V P_1 \tag{41}$$

Dependence of impulse on initial temperature

At fixed composition and initial pressure, the impulse decreases with increasing initial temperature. This is because the mass in the detonation tube varies inversely with initial temperature when the pressure is fixed. From Eq. 39, we have

$$I \propto \frac{V}{T_1} \, . \tag{42}$$

Mixture-based specific impulse

At fixed composition, the mixture-based specific impulse is essentially independent of initial pressure and initial temperature:

$$I_{sp} = \frac{I}{Mg} \approx \frac{\sqrt{q}}{g} K \sqrt{2\frac{\gamma-1}{\gamma+1}} \left(\frac{2\gamma}{\gamma+1} \right)^{-\frac{2\gamma}{\gamma-1}} \, . \tag{43}$$

This also holds for the fuel-based specific impulse since at fixed composition, the fuel mass is a fixed fraction of the total mass. More generally, Eq. 43 shows that the specific impulse is proportional to the square root of the specific energy content of the explosive mixture

$$I_{sp} \propto \sqrt{q} \, . \tag{44}$$

The coefficient in Eq. 43 can be numerically evaluated using our value of the coefficient K of 4.3 and a value of γ obtained from equilibrium computations[21]. The range of γ for the mixtures considered (Table 2) was $1.16 < \gamma < 1.26$ where fuel-oxygen-nitrogen mixtures usually have a higher γ than undiluted fuel-oxygen mixtures. The resulting coefficient of proportionality in Eq. 44 is between 0.061 and 0.071 with an average value of 0.065 when q is expressed in J/kg, so that $I_{sp} \approx 0.065\sqrt{q}$.

The value of q is calculated with Eq. 32 and the results (Table 2) of equilibrium computations of M_{CJ} and γ. Eq. 32 can be rearranged to give q explicitly

$$q = \frac{\gamma R T_1}{2(\gamma^2-1)} \left(M_{CJ} - \frac{1}{M_{CJ}} \right)^2 \, . \tag{45}$$

Values of q given in Table 2 were computed using this expression with a gas constant based on the reactant molar mass. Note that the values of q computed in this fashion are significantly less than the specific heat of combustion q_c when the CJ temperature is above 3500 K. This is due to dissociation of the major products reducing the temperature and the effective energy release.

The scaling relationship of Eq. 44 is tested in Fig. 16 by plotting the model impulse I_{sp} versus the effective specific energy release q for all of the cases shown in Table 2. The approximate relationship $I_{sp} \approx 0.065\sqrt{q}$ is also shown. In general, higher values of the specific impulse correspond to mixtures with a lower nitrogen dilution and, hence, a higher energy release, for which the CJ temperature is higher and dissociation reactions are favored. There is reasonable agreement between the model I_{sp} and the approximate

square root scaling relationship with a fixed coefficient of proportionality. However, there is significant scatter about the average trend due to the dependence of γ on the mixture composition and temperature. Including this dependence substantially improves the agreement and the predictions of Eq. 43 are within 3.5% of the values computed by Eq. 8.

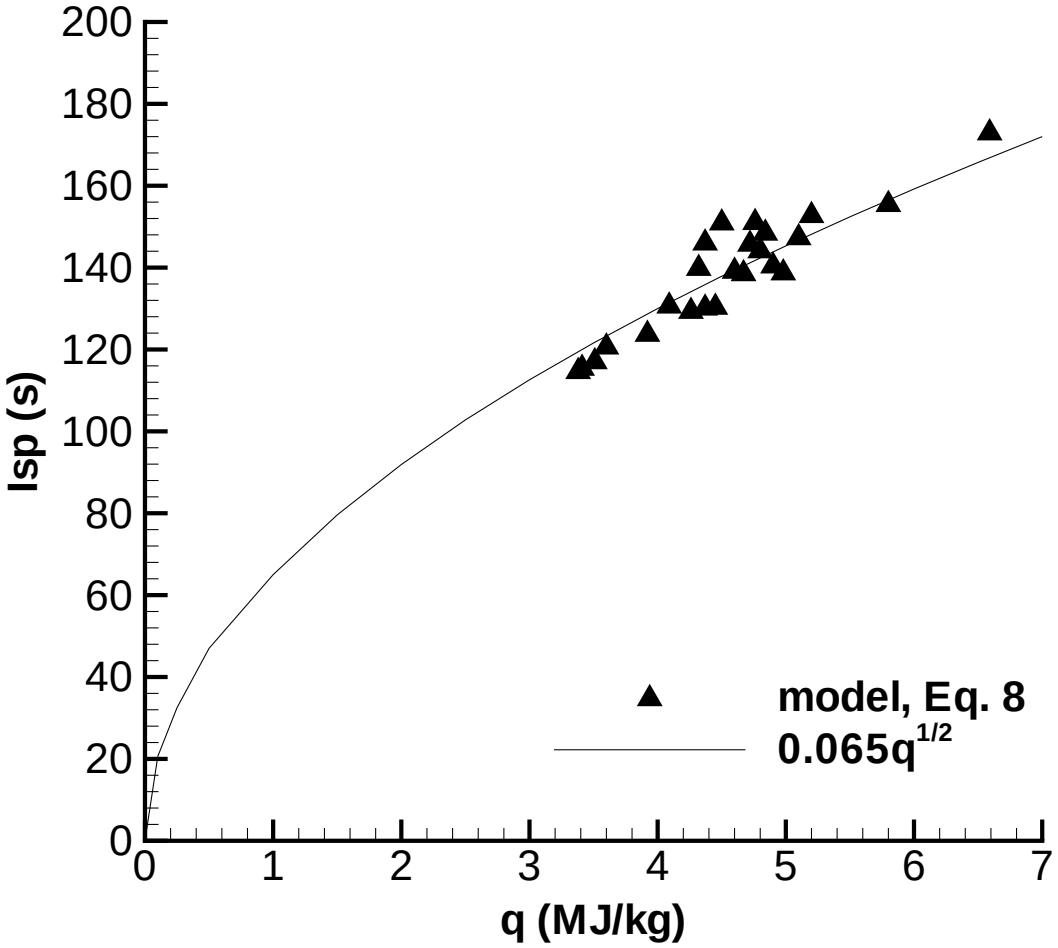

Figure 16: Specific impulse scaling with energy content. Model predictions (Eq. 8) versus effective specific energy content q for hydrogen, acetylene, ethylene, propane, and JP10 with air and oxygen including 0, 20%, 40%, and 60% nitrogen dilution at $P_1 = 1$ bar and $T_1 = 300$ K.

7 Impulse predictions – Parametric studies

Impulse calculations were carried out for different mixtures, equivalence ratios, initial pressures, and nitrogen dilutions. Unless otherwise mentioned, all calculations were performed with an initial temperature of 300 K.

The model input parameters consist of the external environment pressure P_0, the detonation velocity U_{CJ}, the sound speed behind the detonation front c_2, the CJ pressure P_2, and the ratio of the specific heats of the products γ. All parameters were computed using equilibrium calculations[21] performed with a realistic set of combustion products. The input parameters were used in Eqs. 12, 29, and 19 to calculate P_3 and α. The parameters were then used in Eq. 8 to obtain the impulse.

The impulse is calculated for the following fuels: ethylene, propane, acetylene, hydrogen, Jet A, and JP10 with varying initial pressure (Figs. 17, 20, 23), equivalence ratio (Figs. 18, 21, 24), and nitrogen dilution (Figs. 19, 22, 25). Results are expressed in terms of impulse per unit volume of the tube, specific impulse, and fuel-based specific impulse. Results for hydrogen-oxygen mixtures are strictly valid for equivalence ratios less than 0.8 and for hydrogen-air mixtures with equivalence ratios less than 2.2. In these cases, the calculations are probably reasonable estimates but the reader should keep in mind that the underlying physical assumption is no longer justified. The results for Jet A and JP10 assume that these fuels are in completely vaporized form for all initial conditions. While unrealistic at low temperatures, this gives a uniform basis for comparison of all fuels.

7.1 Impulse per unit volume

The impulse per unit volume is independent of the tube size and is linearly dependent on the initial pressure, as indicated by Eq. 41. The variation of I_V with P_1, ϕ, and $N_2\%$ is shown in Figs. 17, 18, and 19. Hydrogen cases are very different from hydrocarbons. The impulse per unit volume is much lower due to the lower molecular mass of hydrogen, which results in lower density and CJ pressure. Eq. 40 shows that the impulse per unit volume is proportional to the density of the explosive mixture and the square root of the specific energy release. The specific energy release of hydrogen mixtures is of the same order as that obtained with other fuels, but the density of hydrogen mixtures is much lower, resulting in a lower impulse per unit volume.

Impulse per unit volume versus equivalence ratio is shown in Fig. 18. The impulse is expected to be maximum at stoichiometric conditions from Eq. 40 if we consider only the major products of combustion. However, examining the plot we see that, with the exception of hydrogen, the maximum values of I_V occur for rich ($\phi \sim 2$) fuel-oxygen mixtures and slightly rich ($\phi \sim 1.1$–1.2) fuel-air mixtures. Equilibrium computations reveal that the maximum detonation velocity and pressure also occur for rich mixtures. Even though the nominal heat of reaction of the mixture based on major products is maximum at stoichiometry, the detonation velocity is not a maximum at stoichiometric because of the product species distribution for rich combustion. Increasing amounts of

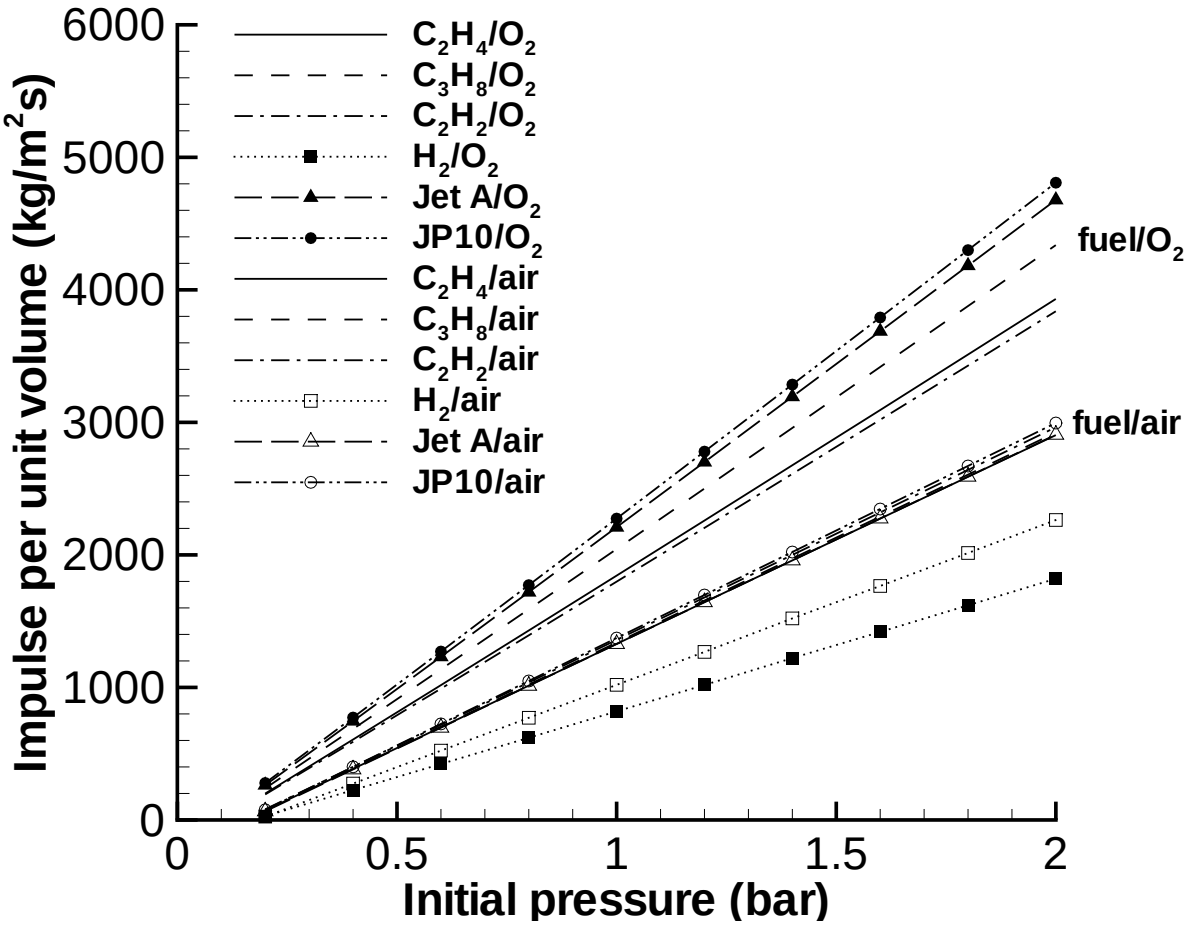

Figure 17: Variation of impulse per unit volume with initial pressure. Nominal initial conditions are $T_1 = 300$ K, stoichiometric fuel-oxygen ratio.

CO and H_2 in increasingly rich mixtures results in a larger number of products, effectively increasing the heat of reaction and shifting the peak detonation velocity and pressure to a rich mixture. The effect is much stronger in fuel-oxygen mixtures than in fuel-air mixtures since the nitrogen in the air moderates the effect of the increasing number of products in rich mixtures. A similar effect is observed in flames.

In the case of hydrogen, the product distribution effect is not as prominent since the number of major products is always less than reactants, independent of stoichiometry. For hydrogen-air mixtures, the maximum I_V is obtained for an equivalence ratio close to 1. The impulse of hydrogen-oxygen mixtures decreases monotonically with increasing equivalence ratio. Unlike hydrocarbon fuels, which have a molecular mass comparable to or higher than oxygen and air, hydrogen has a much lower molecular mass. Thus, increasing the equivalence ratio causes a sharp decrease in the mixture density. The linear dependence of the impulse per unit volume with mixture density dominates over its square root variation with effective energy release (Eq. 40), resulting in a decreasing impulse with increasing equivalence ratio for hydrogen-oxygen mixtures.

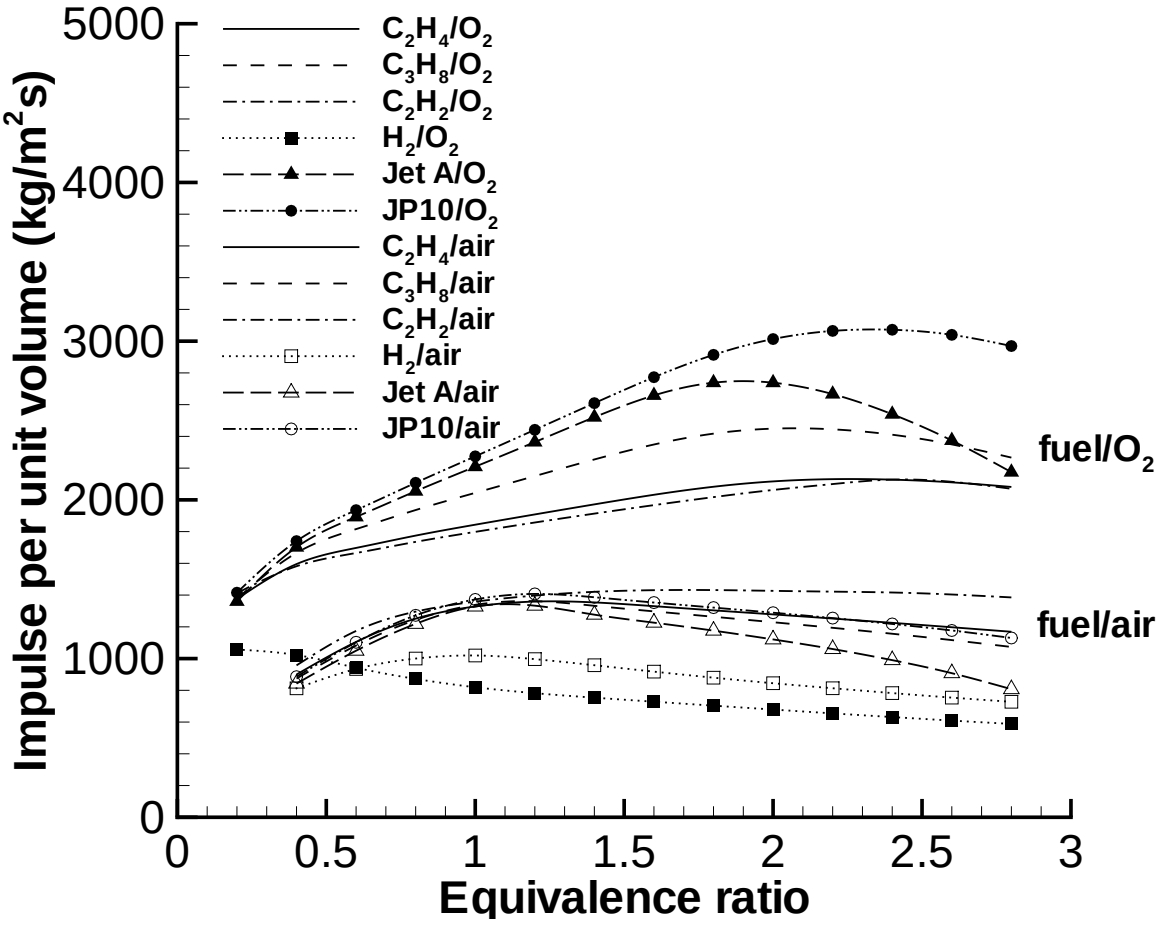

Figure 18: Variation of impulse per unit volume with equivalence ratio. Nominal initial conditions are $P_1 = 1$ bar, $T_1 = 300$ K.

The impulse per unit volume generated by the different fuels with oxygen can be ranked in all cases as follows from lowest to highest: hydrogen, acetylene, ethylene, propane, Jet A, and JP10. The impulse is generated by the chemical energy of the mixture, which depends on a combination of bond strength and hydrogen to carbon ratio. The results obtained for the impulse per unit volume versus the equivalence ratio are presented for an equivalence ratio range from 0.4 to 2.6. The results of calculations at higher equivalence ratios were considered unreliable because carbon production, which is not possible to account for correctly in equilibrium calculations, occurs for very rich mixtures, in particular for Jet A and JP10.

The nitrogen dilution calculations (Fig. 19) show that the impulse decreases with increasing nitrogen dilution for hydrocarbon fuels. However, as the dilution increases, the values of the impulse for the different fuels approach each other. The presence of the diluent masks the effect of the hydrogen to carbon ratio. The hydrogen curve is much lower due to the lower CJ pressures caused by the lower molecular mass and heat of combustion of hydrogen. Unlike for hydrocarbons, this curve has a maximum. The presence

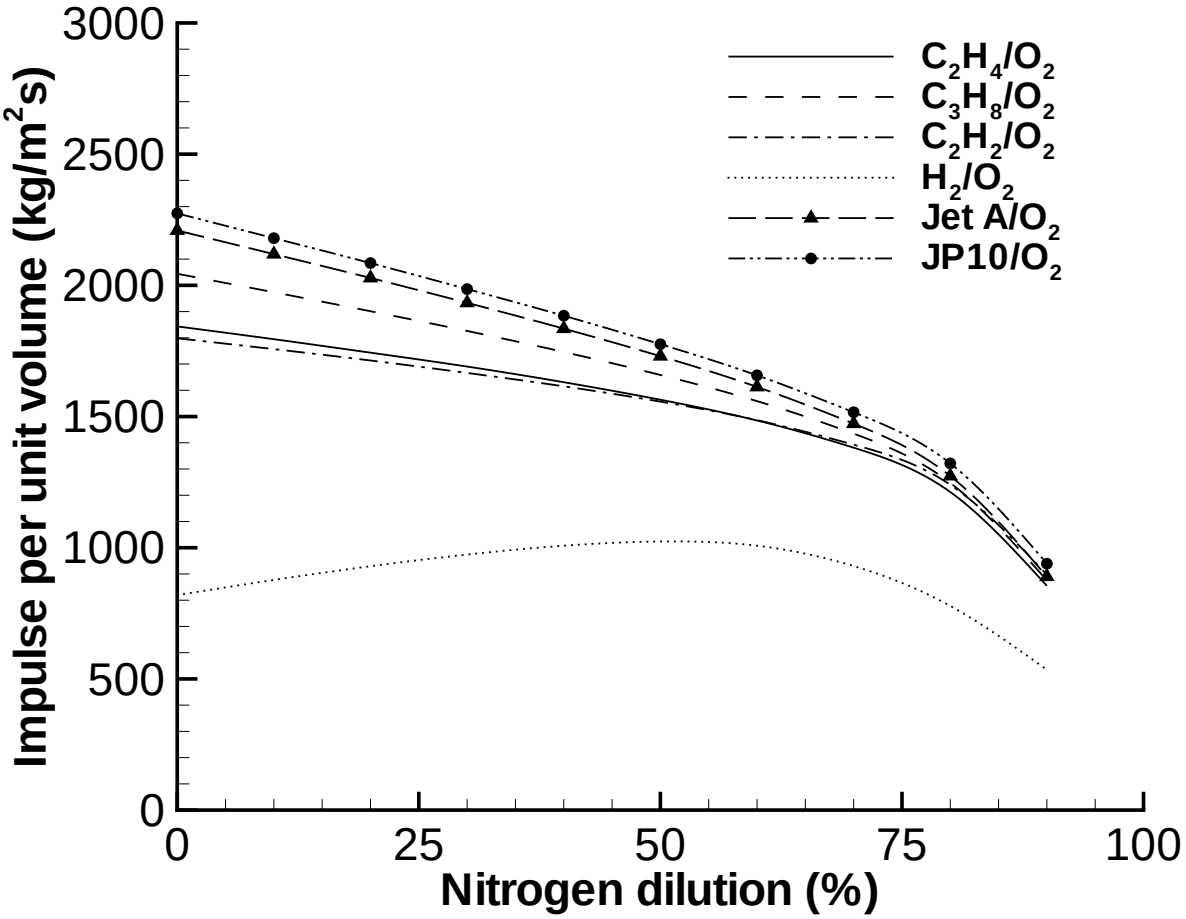

Figure 19: Variation of impulse per unit volume with nitrogen dilution. Nominal initial conditions are $P_1 = 1$ bar, $T_1 = 300$ K, stoichiometric fuel-oxygen ratio.

of this maximum can be explained by the two competing effects of nitrogen addition: one is to dilute the mixture, reducing the energy release per unit mass (dominant at high dilution), while the other is to increase the molecular mass of the mixture (dominant at low dilution). Note that the highest value of the impulse is obtained close to 50% dilution, which is similar to the case of air (55.6% dilution).

7.2 Mixture-based specific impulse

The mixture-based specific impulse I_{sp} is plotted versus initial pressure, equivalence ratio, and nitrogen dilution in Figs. 20, 21, and 22, respectively. The specific impulse decreases steeply as the initial pressure decreases due to the increasing importance of dissociation at low pressures (Fig. 20). Dissociation is an endothermic process and the effective energy release q decreases with decreasing initial pressure.

Recombination of radical species occurs with increasing initial pressure. At sufficiently high initial pressures, the major products dominate over the radical species and the CJ

detonation properties tend to constant values. The mixture-based specific impulse tends to a constant value at high pressures, which is in agreement with the impulse scaling relationship of Eq. 43 if the values of q and γ reach limiting values with increasing initial pressure. Additional calculations for ethylene and propane with oxygen and air showed that the specific impulse was increased by approximately 7% between 2 and 10 bar and by less than 2% between 10 and 20 bar, confirming the idea of a high-pressure limit.

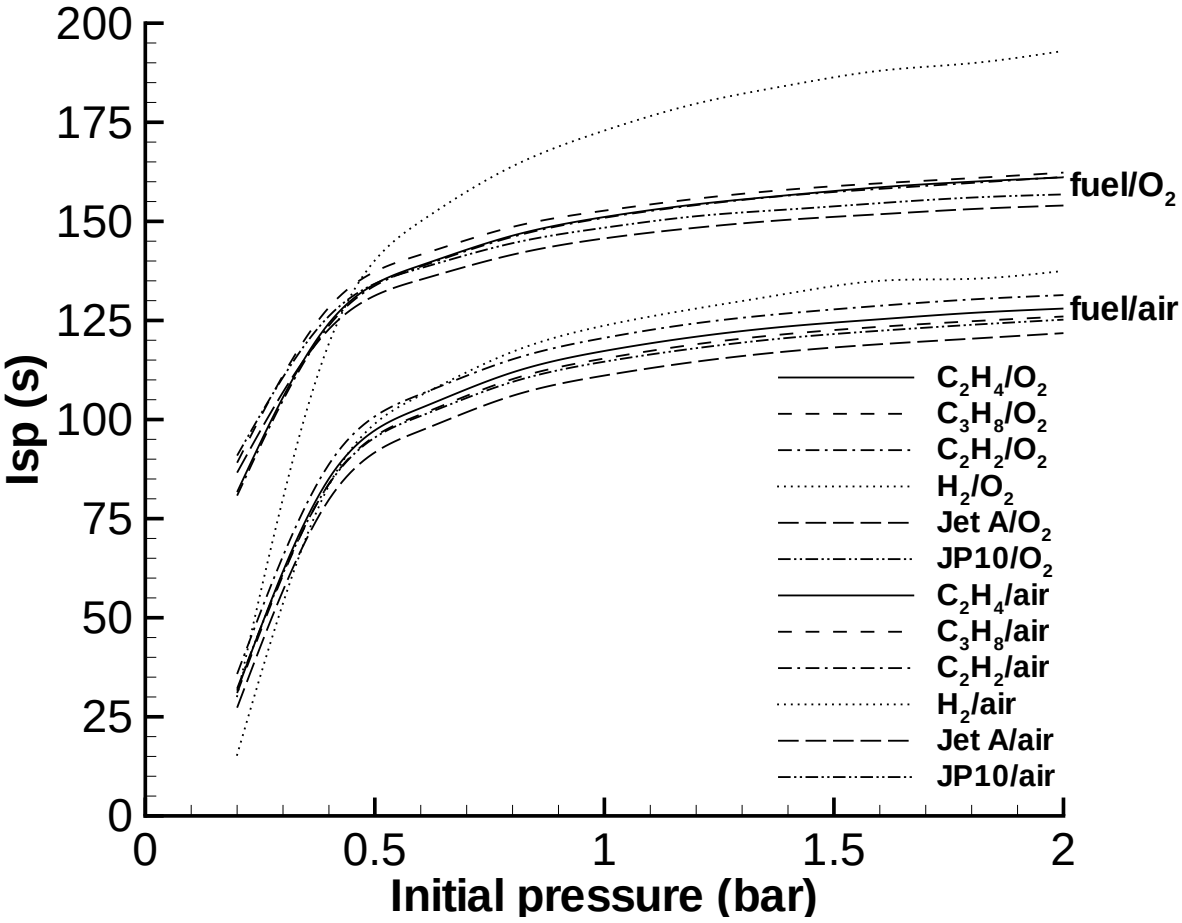

Figure 20: Variation of mixture-based specific impulse with initial pressure. Nominal initial conditions are $T_1 = 300$ K, stoichiometric fuel-oxygen ratio.

The specific impulses of hydrocarbon fuels varying the equivalence ratio (Fig. 21) have a similar behavior to that of the impulse per unit volume. This is expected since the only difference is due to the mixture density. Most hydrocarbon fuels have a heavier molecular mass than the oxidizer, but the fuel mass fraction for heavier fuels is smaller. The overall fuel mass in the mixture does not change much with the equivalence ratio, so the mixture density does not vary significantly. However, this effect is important in the case of hydrogen, where the mixture density decreases significantly as the equivalence ratio increases. This accounts for the monotonic increase of the hydrogen-oxygen curve. In the case of hydrogen-air, the mixture density effect is masked because of the nitrogen

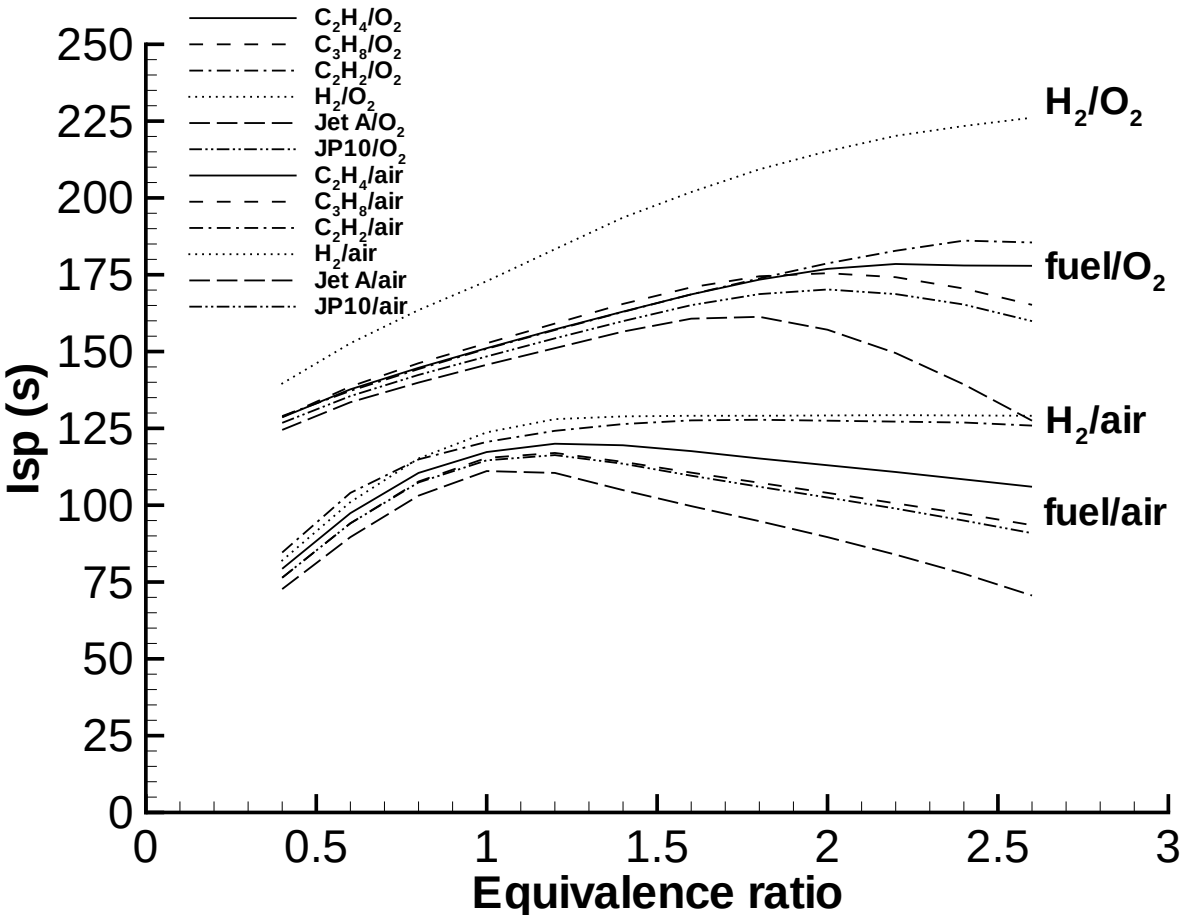

Figure 21: Variation of mixture-based specific impulse with equivalence ratio. Nominal initial conditions are $P_1 = 1$ bar, $T_1 = 300$ K.

dilution, which explains the nearly constant portion of the curve on the rich side. The variation of the I_{sp} with nitrogen dilution, Fig. 22, is the same for all fuels including hydrogen. The mixture-based specific impulse decreases as the nitrogen amount in the mixture increases.

7.3 Fuel-based specific impulse

The fuel-based specific impulse I_{spf} is plotted versus initial pressure, equivalence ratio, and nitrogen dilution in Figs. 23, 24, and 25, respectively. The variation of I_{spf} with initial pressure, Fig. 23, is very similar to the corresponding behavior of I_{sp}. The curves are individually shifted by a factor equal to the fuel mass fraction. Note the obvious shift of the hydrogen curves because of the very low mass fraction of hydrogen. The fuel-based specific impulse is about three times higher for hydrogen than for other fuels.

The plots on Fig. 24 show a monotonically decreasing I_{spf} with increasing equivalence ratio. This is due to the predominant influence of the fuel mass fraction, which goes

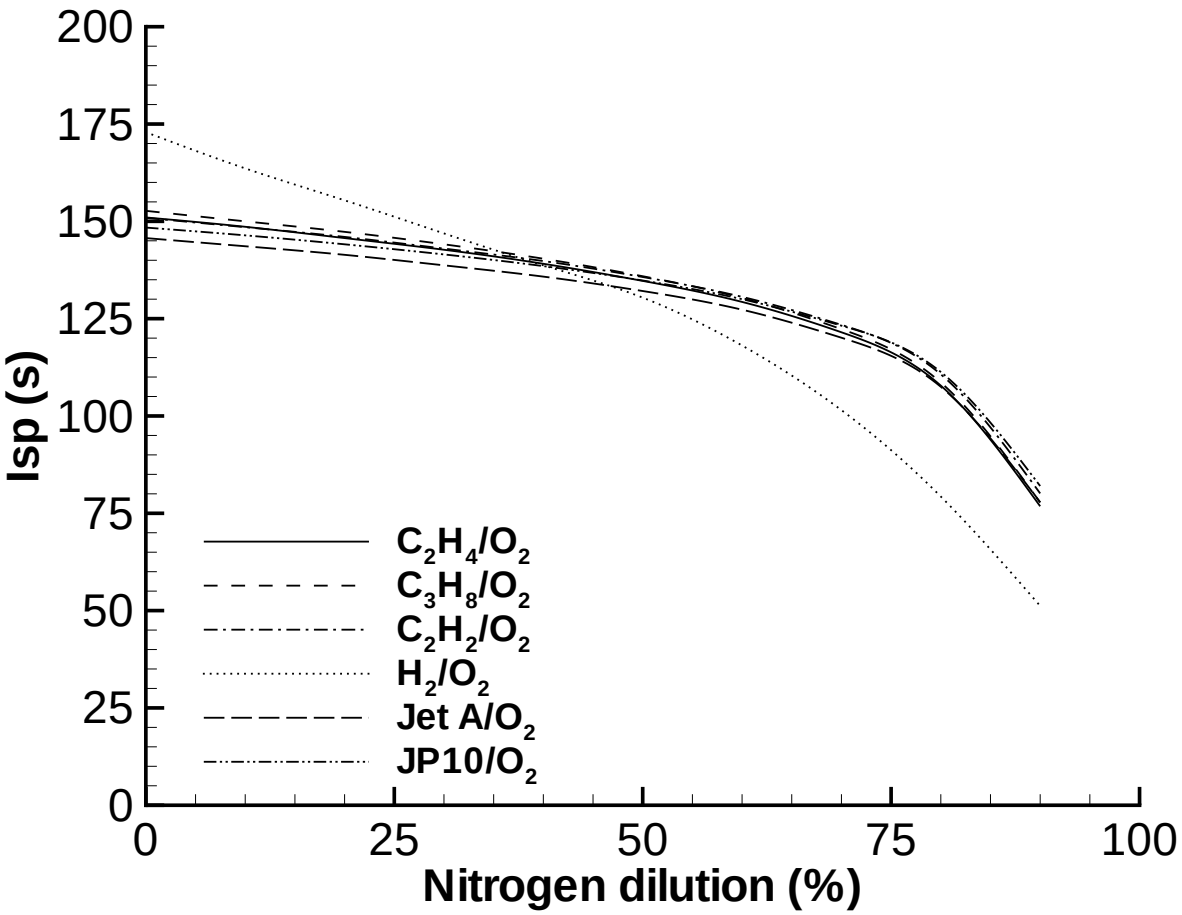

Figure 22: Variation of mixture-based specific impulse with nitrogen dilution. Nominal initial conditions are $P_1 = 1$ bar, $T_1 = 300$ K, stoichiometric fuel-oxygen ratio.

from low on the lean side to high on the rich side. The hydrogen mixtures again have much higher values compared to the hydrocarbon fuels due to the lower molar mass of hydrogen as compared to the hydrocarbon fuels. The values of I_{spf} shown in Fig. 25 exhibit a monotonically increasing behavior with increasing nitrogen dilution, due to the decrease in fuel mass fraction as the nitrogen amount increases.

7.4 Influence of initial temperature

Temperature is an initial parameter that may significantly affect the impulse, especially at values representative of stagnation temperature for supersonic flight or temperatures required to vaporize aviation fuels. The results shown in previous figures were for an initial temperature of 300 K. Calculations with initial temperatures from 300 to 600 K were carried out for stoichiometric JP10-air; JP10 is a low vapor pressure liquid ($C_{10}H_{16}$) at room temperature. The impulse per unit volume (Fig. 26) and the mixture-based specific impulse (Fig. 27) were calculated as a function of the initial temperature for

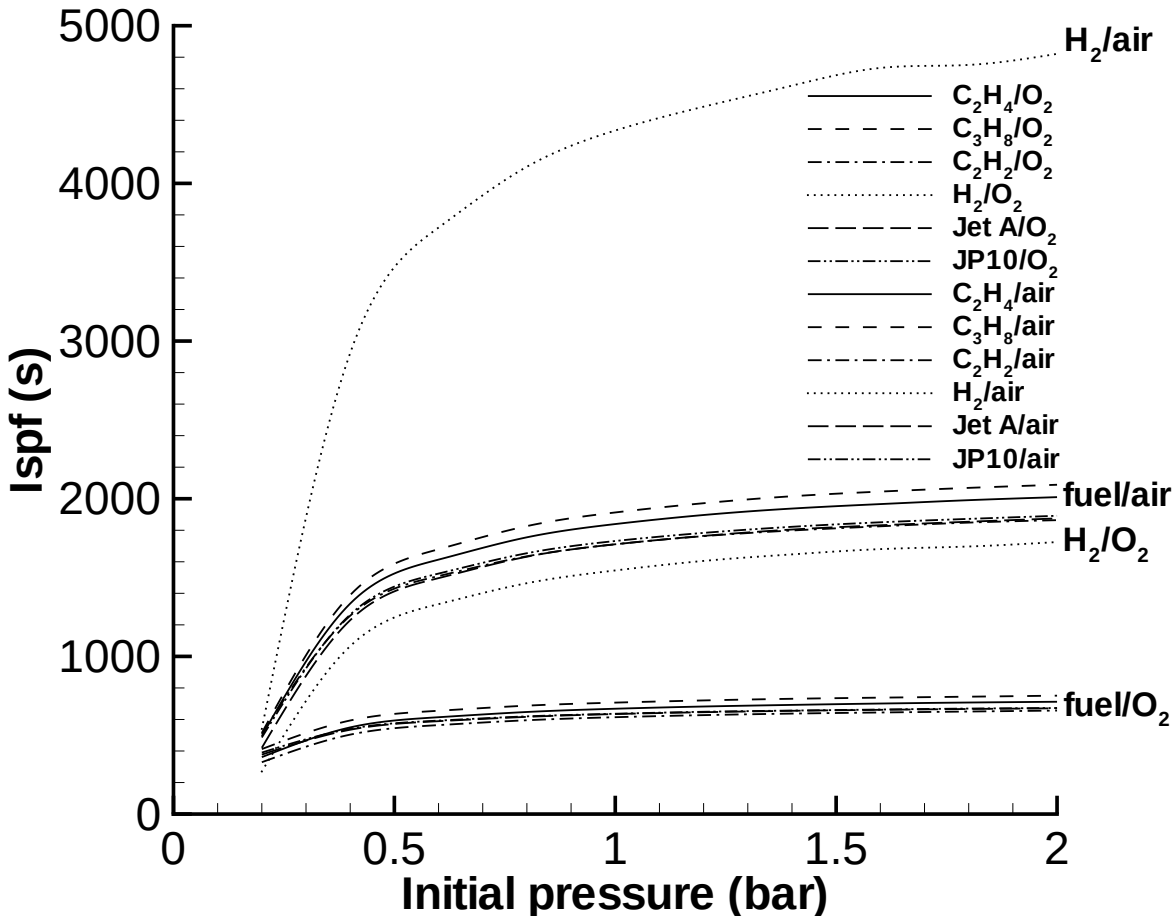

Figure 23: Variation of fuel-based specific impulse with initial pressure. Nominal initial conditions are $T_1 = 300$ K, stoichiometric fuel-oxygen ratio.

different pressures representative of actual stagnation pressure values in a real engine.

The impulse per unit volume decreases with increasing initial temperature, as predicted by Eq. 42. At fixed pressure and composition, this decrease is caused by the decrease of the initial mixture density. The mixture-based specific impulse is found to be approximately constant when initial temperature and initial pressure are varied (Fig. 27). The scaling predictions of Eq. 43 are verified for constant composition. The slight decrease of the specific impulse observed with increasing temperature and decreasing pressure can be attributed to the promotion of dissociation reactions under these conditions. Specific impulse is a useful parameter for estimating performance since at high enough initial pressures, it is almost independent of initial pressure and temperature.

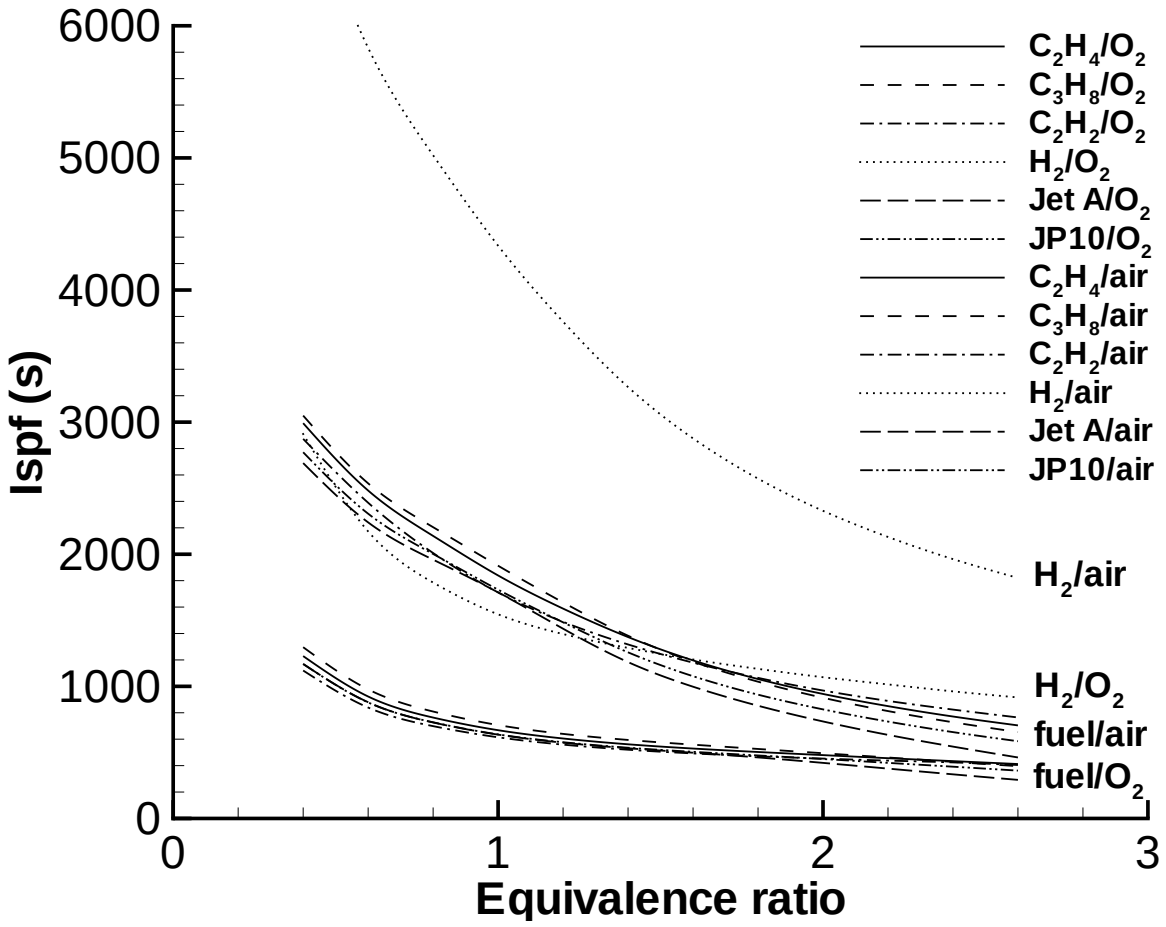

Figure 24: Variation of fuel-based specific impulse with equivalence ratio. Nominal initial conditions are $P_1 = 1$ bar, $T_1 = 300$ K.

8 Conclusions

An analytical model for the impulse of a pulse detonation tube has been developed using a simple one-dimensional gas dynamic analysis and empirical observations. The model offers the possibility to evaluate in a simple way the performance of the most basic form of a pulse detonation engine, consisting of a straight tube open at one end. The model predictions were compared with various experimental results, from direct single-cycle impulse measurements[12, 1] to multi-cycle thrust measurements[2, 3], and also numerical simulations. These show reasonable agreement (within $\pm 15\%$ or better in most cases) for comparisons of impulse per unit volume, specific impulse, and thrust. Parametric calculations were conducted for a wide range of initial conditions, including fuel type (hydrogen, acetylene, ethylene, propane, Jet A, and JP10), initial pressure (from 0.2 to 2 bar), equivalence ratio (from 0.4 to 2.6), and nitrogen dilution (from 0 to 90%).

The impulse of a detonation tube was found to scale directly with the mass of the explosive mixture in the tube and the square root of the effective energy release per

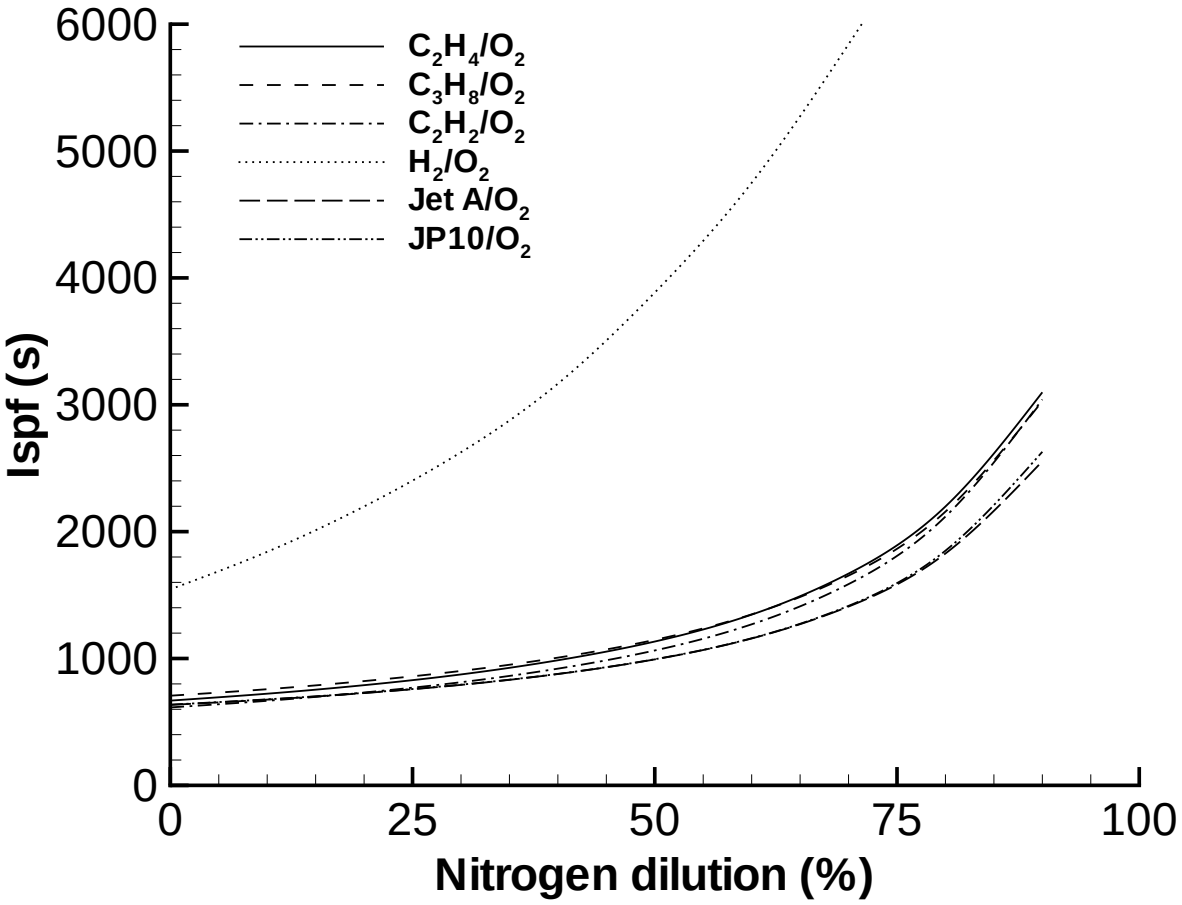

Figure 25: Variation of fuel-based specific impulse with nitrogen dilution. Nominal initial conditions are $P_1 = 1$ bar, $T_1 = 300$ K, stoichiometric fuel-oxygen ratio.

unit mass of the mixture. A procedure was given to account for product dissociation in determining the effective specific energy release. We derived scaling relationships and carried out equilibrium computations to verify the following conclusions:

1. At fixed composition and initial temperature, the impulse per unit volume varies linearly with initial pressure.

2. At fixed composition and initial pressure, the impulse per unit volume varies inversely with initial temperature.

3. At fixed composition and sufficiently high initial pressure, the specific impulse is approximately independent of initial pressure and initial temperature. This makes specific impulse the most useful parameter for estimating pulse detonation tube performance over a wide range of initial conditions.

The predicted values of the mixture-based specific impulse are on the order of 150 s for hydrocarbon-oxygen mixtures, 170 s for hydrogen-oxygen, and on the order of 115 to 130

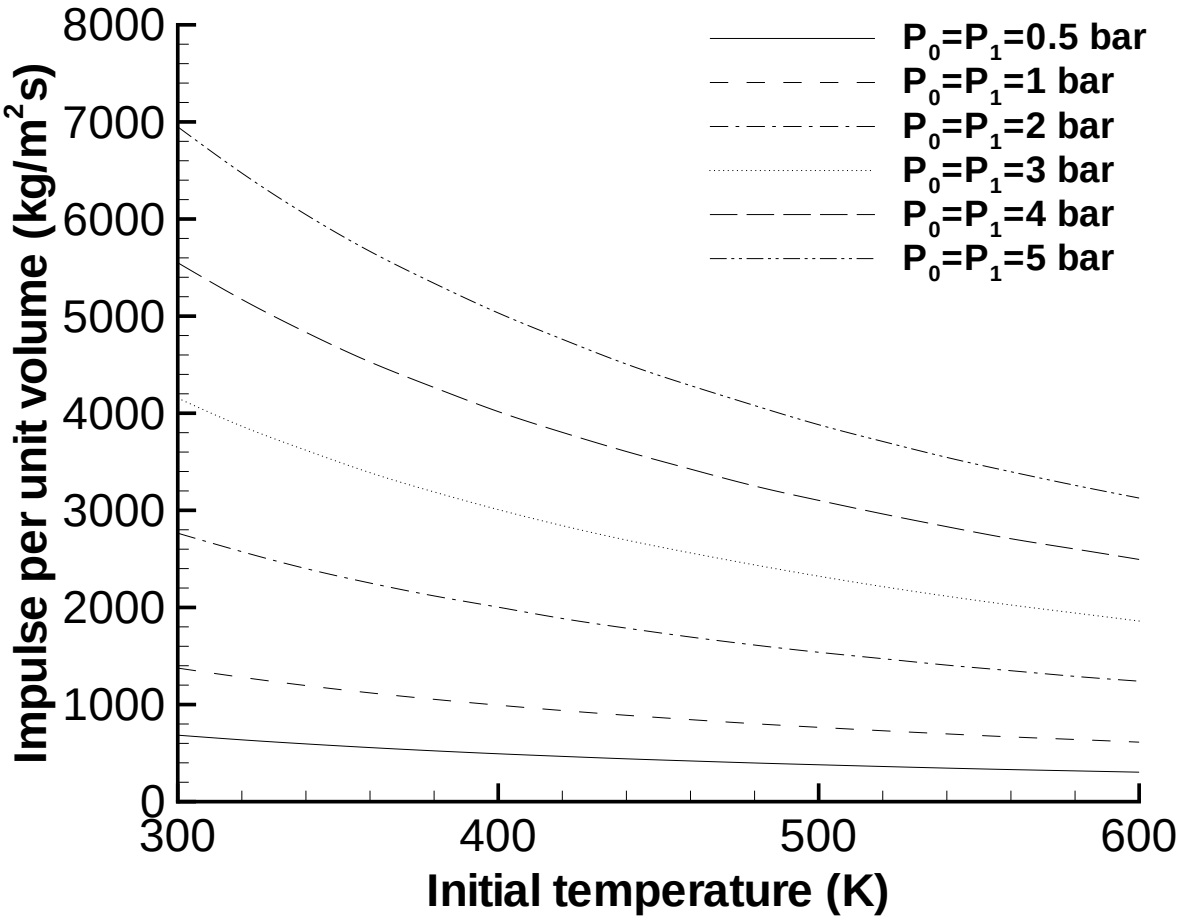

Figure 26: Variation of impulse per unit volume with initial temperature for different values of the stagnation pressure.

s for fuel-air mixtures at initial conditions of 1 bar and 300 K. These values are lower than the maximum impulses possible with conventional steady propulsion devices[33, 34]. As mentioned in the introduction, there are many other factors that should be considered in evaluating PDE performance and their potential applications. The present study provides some modeling ideas that could be used as a basis for more realistic engine simulations.

9 Acknowledgments

This work was supported by the Office of Naval Research Multidisciplinary University Research Initiative *Multidisciplinary Study of Pulse Detonation Engine* (grant 00014-99-1-0744, sub-contract 1686-ONR-0744), and General Electric contract GE-PO A02 81655 under DABT-63-0-0001. We are grateful to Prof. Hans Hornung for the numerical simulations. We thank Fred Schauer at the AFRL for sharing his data with us.

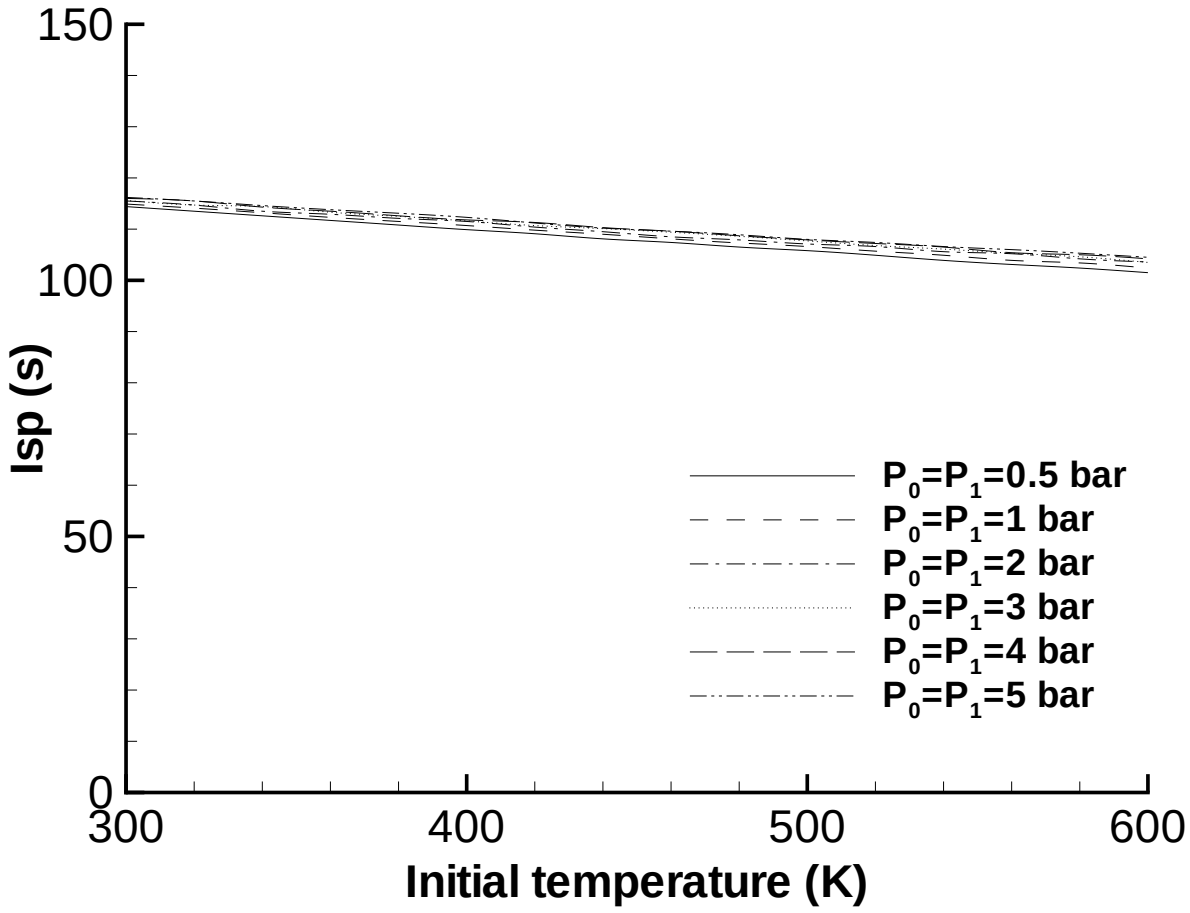

Figure 27: Variation of mixture-based specific impulse with initial temperature for different values of the stagnation pressure.

Part III
Measurements

This part is a reprint of a paper prepared for the Journal of Propulsion and Power. It describes experimental results of measuring impulse from a pulse detonation tube.

Direct experimental impulse measurements for detonations and deflagrations

M. Cooper, S. Jackson, J.M. Austin, E. Wintenberger, and J.E. Shepherd
Graduate Aeronautical Laboratories,
California Institute of Technology, Pasadena, CA 91125

Abstract

Direct impulse measurements were carried out by using a ballistic pendulum arrangement for detonations and deflagrations in a tube closed at one end. Three tubes of different lengths and inner diameters were tested with stoichiometric propane- and ethylene-oxygen-nitrogen mixtures. Results were obtained as a function of initial pressure and percent diluent. The experimental results were compared to predictions from an analytical model[4] and generally agreed to within 15%. The effect of internal obstacles on the transition from deflagration to detonation was studied. Three different extensions were tested to investigate the effect of exit conditions on the ballistic impulse for stoichiometric ethylene-oxygen-nitrogen mixtures as a function of initial pressure and percent diluent.

10 Nomenclature

A_{TS}	area of thrust surface
A_{lip}	area of lip at exit of tube
c_2	sound speed of burned gases just behind detonation wave
c_3	sound speed of burned gases behind Taylor wave
d	inner diameter of detonation tube
F	force exerted on detonation tube in direction of tube axis
g	standard earth gravitational acceleration
I	single-cycle impulse
I_{sp}	mixture-based specific impulse
I_V	impulse per unit volume
L	length of detonation tube filled with charge
L_p	length of pendulum arm
L_t	overall length of detonation tube and extension
m	pendulum mass
p	pitch of spiral obstacles
P_1	initial pressure of reactants
P_2	Chapman-Jouguet pressure
P_3	pressure of burned gases behind Taylor wave
P_{env}	environment pressure
P_{lip}	pressure on lip at exit of tube
P_{TS}	pressure on thrust surface in detonation tube interior
S	wetted surface area of tube's inner diameter
T_1	initial temperature of reactants
U_{CJ}	Chapman-Jouguet detonation velocity
V	internal volume of detonation tube
β	ratio of N_2 to O_2 concentration in initial mixture
Δx	horizontal pendulum displacement
γ	ratio of specific heats in combustion products
λ	cell size
ρ_1	density of combustible mixture at the initial temperature and pressure
τ	wall shear stress

11 Introduction

Impulse per cycle is one of the key performance measures of a pulse detonation engine. In order to evaluate the performance of the engine concept, it is necessary to have reliable estimates of the maximum impulse that can be obtained from the detonation of a given fuel-oxidizer combination at a specified initial temperature and pressure. While the overall performance of an engine will depend strongly on a number of other factors such as inlet losses, nonuniformity of the mixture in the detonation tube, and the details (nozzles, extensions, coflow, etc.) of the flow downstream of the detonation tube exit,

conclusive studies investigating the impulse available from a simple detonation tube must be completed. Many researchers have measured the impulse created by detonating a uniform mixture in a constant-area tube that is closed at one end and open at the other with a variety of experimental techniques.

The pioneering work measuring impulse was in 1957 by Nicholls et al.[14] who measured the specific impulse produced by a detonation tube using a ballistic pendulum technique. They measured the single-cycle specific impulse of acetylene- and hydrogen-oxygen mixtures and carried out some multi-cycle experiments using hydrogen-air; however, their experimental values are significantly lower than modern data[2, 1, 10].

Zitoun and Desbordes[12] made an experimental determination of the impulse of a detonation tube using a stoichiometric ethylene-oxygen mixture by integrating the pressure history at the closed end of the tube. They performed their experiments for single-cycle and multi-cycle cases and observed a 30% decrease in the level of impulse for multi-cycle experiments. They attributed this impulse deficit to inadequate filling of the detonation tube. Zhdan et al.[10] measured the impulse generated by a stoichiometric acetylene-oxygen mixture in a short (0.125 or 0.25 m long) cylindrical detonation tube during single-cycle operation using a ballistic pendulum technique. The detonation tube was, in some cases, partially filled with air.

Schauer et al.[2] used a damped thrust stand to measure the impulse of a multi-cycle pulse detonation tube operating with hydrogen-air and more recently, hydrocarbon-air mixtures. Harris et al.[13] studied the effect of deflagration-to-detonation transition (DDT) distance on the impulse of a detonation tube using a ballistic pendulum technique with stoichiometric propane-oxygen mixtures diluted with nitrogen. They showed that there is no significant difference in impulse between directly initiated tests and DDT-initiated tests as long as DDT occurred in the tube and none of the combustible mixture was expelled from the tube prior to detonation.

The present study (preliminary results were given in Cooper et al.[1]) reports single-cycle impulse measurements for ethylene- and propane-oxygen-nitrogen mixtures in three tubes with different lengths, inner diameters, and internal obstacles using a ballistic pendulum arrangement with varying initial pressure and diluent amount. In a companion paper[4], a simple model for impulse is developed and compared to both the present results and selected results from the experiment studies quoted above. This analytical model[4] provides estimates for the impulse per unit volume and specific impulse of a single-cycle pulse detonation engine for a wide range of fuels (including aviation fuels) and initial conditions.

One of the original motivations of this experimental work was to provide a database useful for the validation of both numerical and analytic models. When our studies were initiated in 1999, there was substantial controversy over the impulse that could be obtained from an open-ended detonation tube. The present results, taken together with our simple model[4], numerical simulations, and experiments of others (reviewed by Kailasanath[18]), demonstrate that at least for some fuels (ethylene), there is reasonable agreement of the impulse that can be obtained from a simple detonation tube.

The paper is organized as follows. First, we discuss the experimental details including

the setup and impulse measurement technique with its associated uncertainty analysis. Second, we present experimental results on different DDT regimes followed by single-cycle impulse values for tubes containing spiral obstacles, single-cycle impulse values for tubes containing orifice or blockage plate obstacles, and single-cycle impulse values for tubes with extensions. Third, we discuss the implications of these results for pulse detonation engine technology.

12 Experimental setup and procedure

The detonation tube of Figure 28 consisted of a constant area tube closed at one end by the thrust surface containing the ignition source and open at the other end but initially sealed with a 25 μm thick Mylar diaphragm. The tube was hung from the ceiling by four steel wires in a ballistic pendulum arrangement shown schematically in Figure 29. Direct measurements were made of the impulse delivered by a DDT-initiated detonation or a flame by measuring the maximum horizontal displacement of the tube. The tube was evacuated to a pressure less than 13 Pa at the beginning of each experiment. Using the method of partial pressures, the individual gases comprising the initial mixture were added to the tube and subsequently mixed for 5 minutes with a circulation pump to ensure mixture homogeneity. A spark plug and associated discharge system with 30 mJ of stored energy was used to ignite the combustible mixture at the tube's thrust surface. Combustion products were free to expand out from the open end of the tube into a large ($\simeq$ 50 m^3) blast-proof room. Pressure histories were measured at several locations along the tube length and at the thrust surface (Figure 30). Two of the tubes contained ionization gauges to measure the time-of-arrival of the flame or detonation front. The dimensions and diagonistic capabilities of the three detonation tubes tested are listed in Table 3.

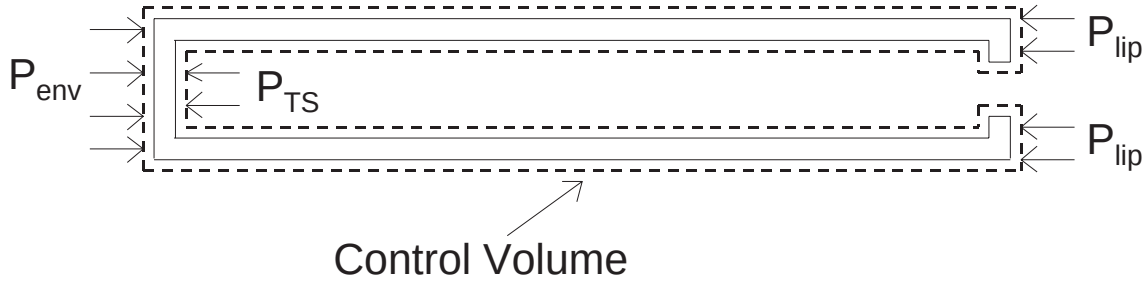

Figure 28: Pulse detonation engine control volume.

The experimental variables included fuel type, initial pressure, diluent amount, and internal obstacles (Table 4). The internal obstacles included Shchelkin spirals, blockage plates, and orifice plates, all with a blockage ratio of 0.43. The choice of blockage ratio, defined as the ratio of blocked area to the total area, was based on work by Lindstedt et al. who cite 0.44 as the optimal configuration[35]. No effort was made in this research to study the effect of blockage ratio on DDT or impulse.

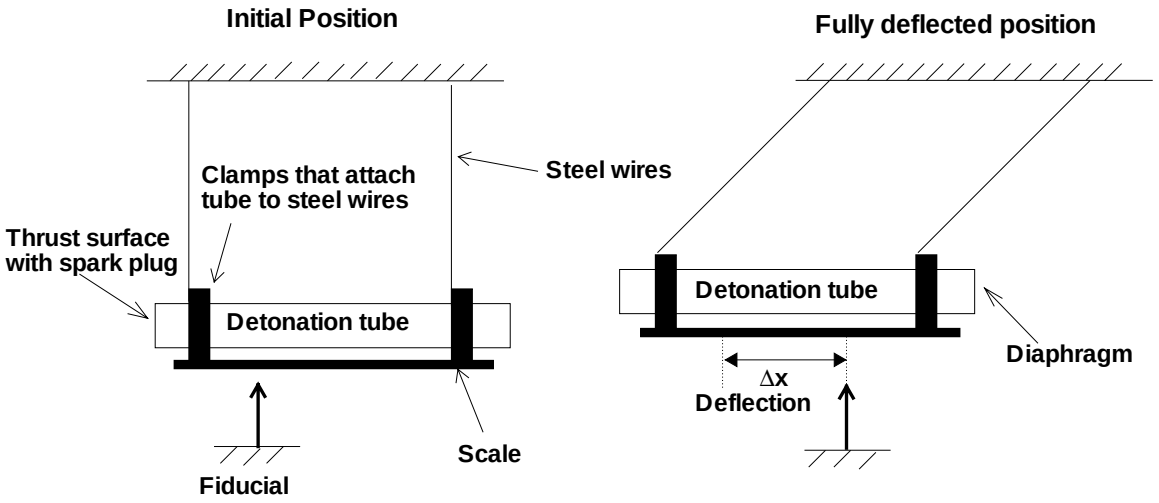

Figure 29: Ballistic pendulum arrangement for direct impulse measurement.

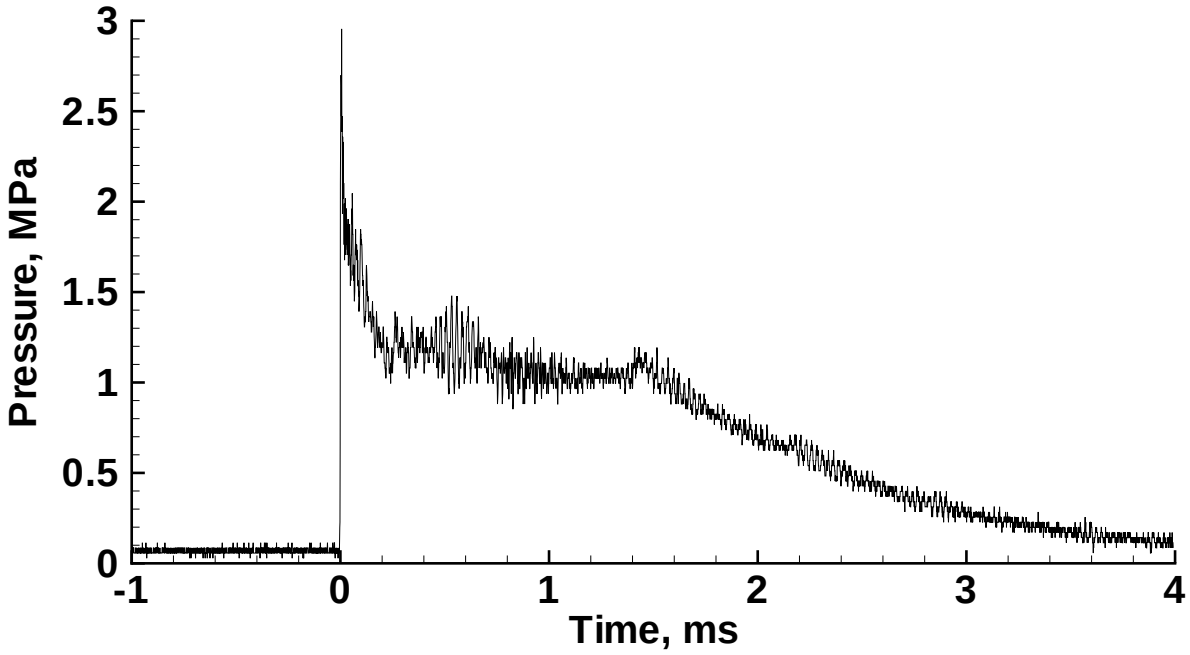

Figure 30: Sample pressure trace of stoichiometric C_2H_4-O_2 at 100 kPa initial pressure recorded at the thrust surface.

The Shchelkin spirals were constructed of stainless steel tubing, with a diameter

Length [m]	Diameter [mm]	Pressure Transducers	Ion Gauges
0.609	76.2	3 and 1 at Thrust Surface	4
1.016	76.2	3 and 1 at Thrust Surface	10
1.5	38.0	3	0

Table 3: Dimensions and diagnostic capabilities of tested detonation tubes.

necessary to yield a blockage ratio of 0.43, coiled to fit inside the detonation tube (Figure 31). The spiral's pitch, p, refers to the axial distance between successive coils of the tubing. The spiral's length refers to the portion of the detonation tube length containing the spiral.

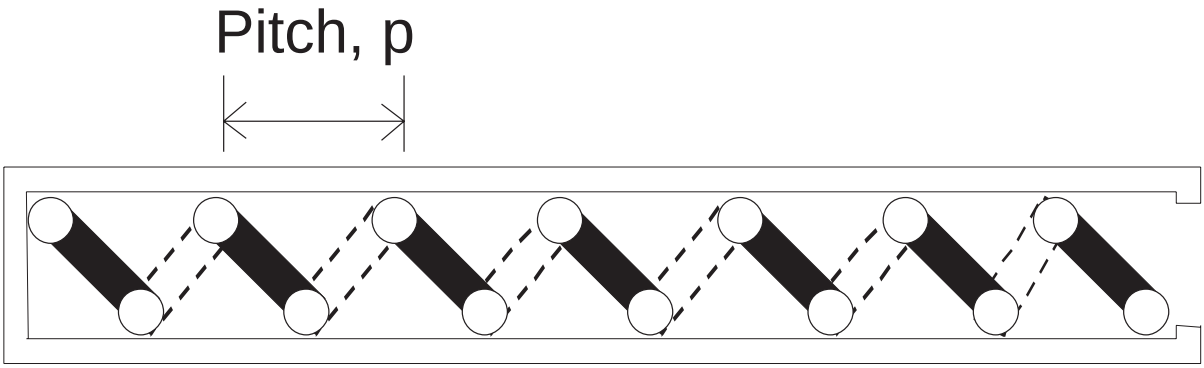

Figure 31: Arrangement of spiral obstacles inside detonation tube.

The blockage plate obstacles consisted of circular plates with an outer diameter smaller than the tube's inner diameter and of the size required to yield a blockage ratio of 0.43 (Figure 32). The blockage plates were suspended along the centerline of the detonation tube by a single threaded rod and spaced approximately one tube diameter apart. Their length refers to the length of the detonation tube containing the blockage plate obstacles.

The orifice plate obstacles consisted of a ring with an outer diameter equal to the inner diameter of the detonation tube and an inner diameter of the size necessary to yield a blockage ratio of 0.43 (Figure 33). The orifice plates were spaced approximately one tube diameter apart. Their length refers to the length of the detonation tube containing the orifice plate obstacles as measured from the thrust surface. The orifice plate obstacles that fill half of the detonation tube are referred to in the figures as "Half Orifice Plate" whereas the orifice plate obstacles that fill the entire tube length are referred to as "Orifice Plate" in the figures.

Three extensions attached to the open end of the 1.016 m length tube were tested and a description of each appears in a later section.

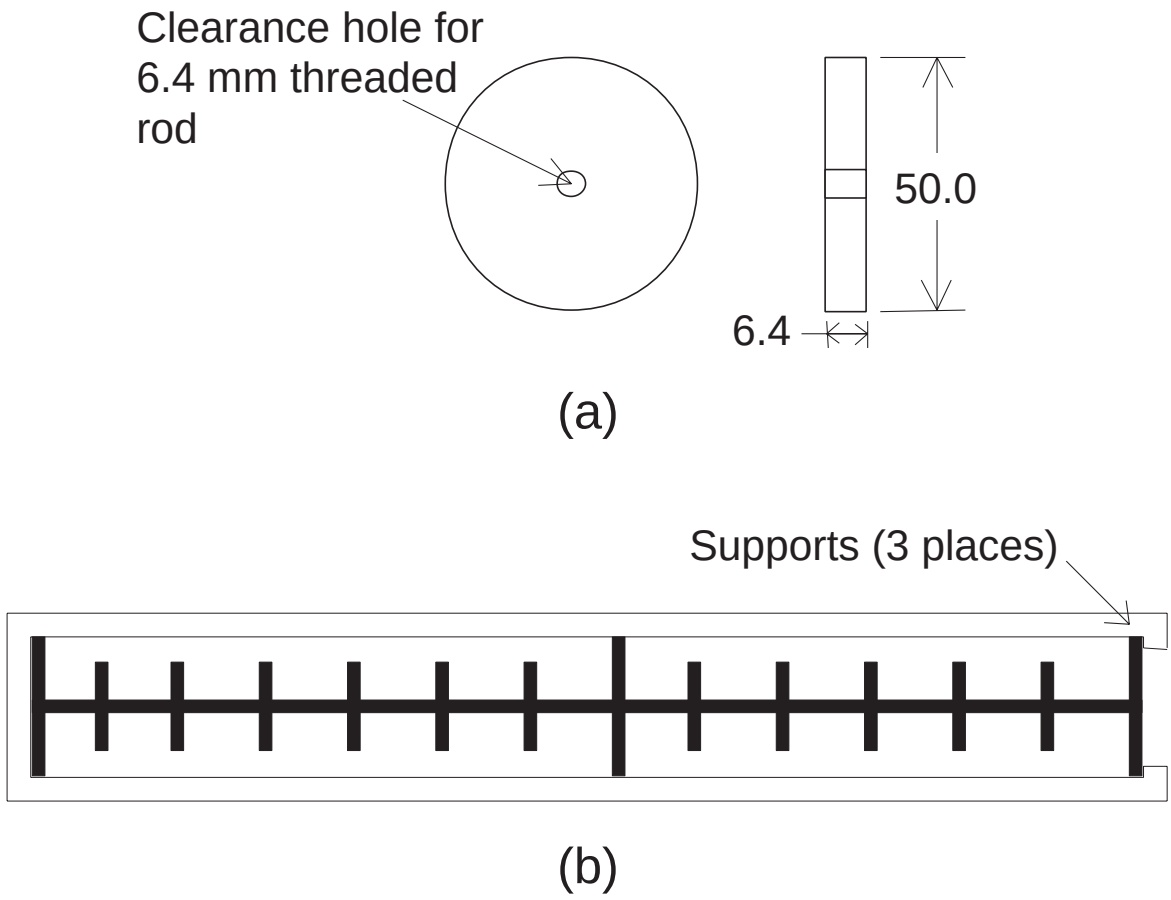

Figure 32: Blockage Plate Obstacles: a) Dimensions of blockage plates in millimeters. b) Arrangement of blockage plates inside detonation tube.

Length	Fuels Tested	Pressures [kPa]	Nitrogen [%]	Internal Obstacles
0.609 m	C_3H_8	50 - 100	0 - air	Spiral with length = 0.609 m, p = 28 mm Spiral with length = 0.609 m, p = 51 mm
1.016 m	C_2H_4	30 - 100	0 - air	No Internal Obstacles Blockage Plate with length = 1.016 m Orifice Plate with length = 1.016 m Half Orifice Plate with length = 0.508 m
1.5 m	C_3H_8	50 - 100	0 - air	Spiral with length = 0.305 m, p = 11 mm

Table 4: Experimental variables of tested detonation tubes.

12.1 Impulse measurement and computation

The impulse was determined by measuring the maximum horizontal deflection of the detonation tube, which is the oscillating mass of the ballistic pendulum. Each support

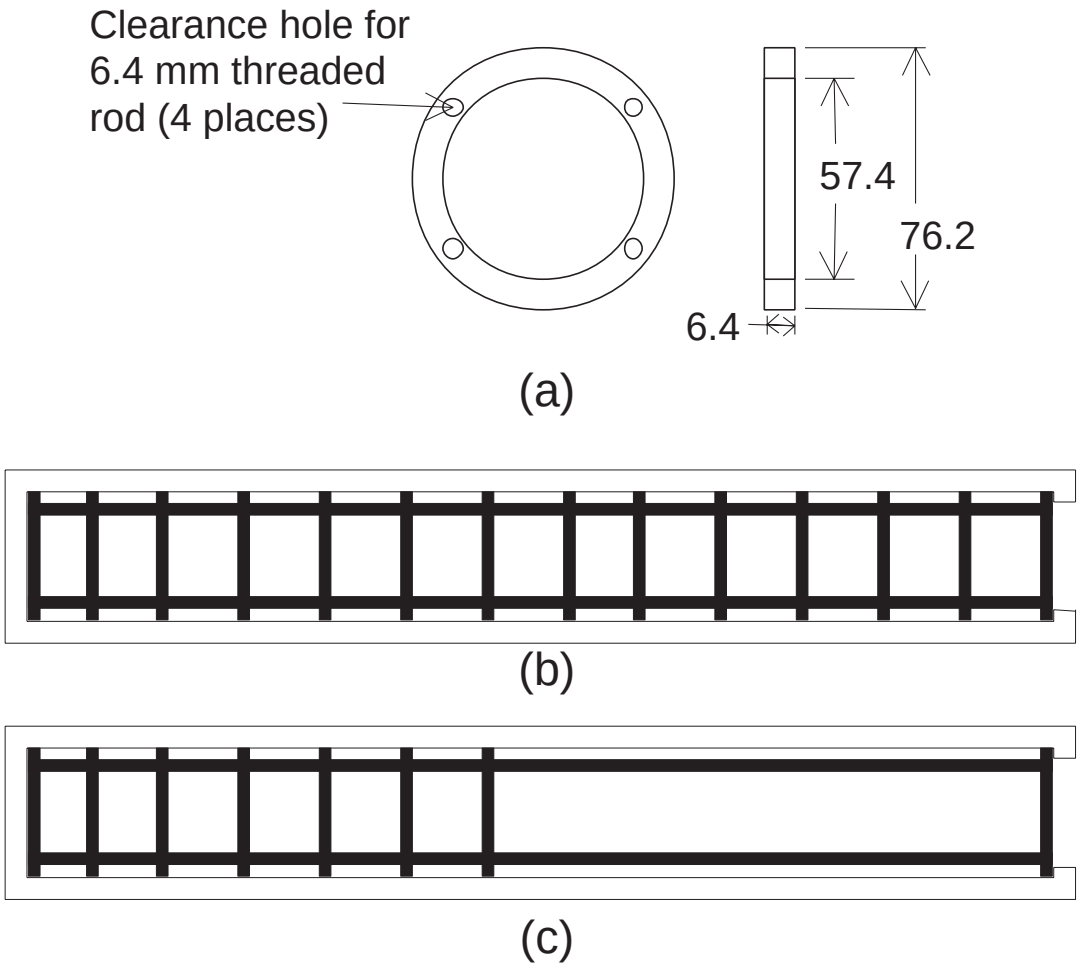

Figure 33: Orifice Plate Obstacles: a) Dimensions of orifice plates in millimeters. b) Arrangment of orifice plates inside detonation tube for the "Orifice Plate" configuration. c) Arrangement of orifice plates inside detonation tube for the "Half Orifice Plate" configuration.

wire was about 1.5 m in length so that the natural period of oscillation was about 2.45 s. During free oscillations, the maximum horizontal deflection occurs at a time equal to one-quarter of the period or 610 ms. The time over which the force is applied can be estimated[4] as $10t_1$, where $t_1 = L/U_{CJ}$ is the time required for the detonation to propagate the length of the tube. For the longest tube tested, the time over which the force is applied is approximately 7.5 ms, which is significantly less than one-quarter of the oscillation period. Therefore, the classical analysis of an impulsively-created motion can be applied and the conservation of energy can be used to relate the maximum horizontal deflection to the initial velocity of the pendulum. From elementary mechanics,

the impulse is given by

$$I = m\sqrt{2gL_p\left(1-\sqrt{1-\left(\frac{\Delta x}{L_p}\right)^2}\right)}\ . \tag{46}$$

This expression is exact given the assumptions discussed above and there are no limits on the values of Δx. Actual values of Δx observed in our experiments were between 50 and 300 mm. The impulse I measured in this fashion is referred to as the *ballistic* impulse, and is specific to a given tube size. Two measures of the impulse that are independent of tube size are the impulse per unit volume

$$I_V = I/V \tag{47}$$

and the specific impulse based on the total explosive mixture mass

$$I_{sp} = \frac{I}{g\rho_1 V}\ . \tag{48}$$

The impulse can also be calculated by placing a control volume around the detonation tube and considering the conservation of momentum. The conventional control volume used in rocket motor analysis is not suitable since the exit flow is unsteady and the required quantities (exit pressure and velocity) are unknown. It is more useful to place the control volume on the surface of the detonation tube (Figure 28) and write a force balance equation in the direction of the tube axis.

$$F = (P_{env} - P_{TS})A_{TS} + \sum_{obstacles}\int P\mathbf{n}\cdot\mathbf{x}\,dA + \int \tau\,dS + (P_{env} - P_{lip})A_{lip} \tag{49}$$

The first term on the right side of the equation is the force on the thrust surface, the second term is the drag (due to pressure differentials) over the obstacles, the third term is the viscous drag, and the last term represents the force over the tube wall thickness. The effect of heat transfer from the combustion products to the added surface area of the obstacles could also reduce the impulse due to a reduction of pressure internal to the detonation tube. We have not considered the role of heat transfer in the present investigation since our tubes are relatively short and the residence time is modest. We expect that heat transfer will become a significant issue for long tubes and/or tubes with exit restrictions that have long residence times for the hot products.

The impulse is obtained by integrating this force over a cycle,

$$I = \int F\,dt\ . \tag{50}$$

If all of the terms making up F can be computed or measured, the ballistic impulse and the impulse computed from this control volume integration should be identical. Previous studies[12] have used Equation 49 to analyze data from unobstructed tubes neglecting

all but the first contribution to the force. This is a resonable approximation when fast transition to detonation occurs; however, in the case of obstacles, the net contribution of the two drag terms may be substantial and using the first term alone can result[36] in overestimating the force and impulse by up to 50%. Since it is difficult to estimate or accurately measure all of the terms in Equation 49, direct measurement of the impulse is the only practical method for tubes with obstructions or other unusual features such as exit nozzles.

12.2 Experimental uncertainties

An analysis was performed to quantify experimental uncertainties associated with the experimental setup and initial conditions using the standard method[37] for estimating error propagation. Generally, the variance ΔI_V associated with the measured quantity $I_V(x_1, ...x_n)$ can be estimated as

$$\Delta I_V = \sqrt{\left(\frac{\partial I_V}{\partial x_1}\right)^2 (\Delta x_1)^2 + ... \left(\frac{\partial I_V}{\partial x_n}\right)^2 (\Delta x_n)^2} \, .$$

Using the expression for ballistic impulse in Equation 1, the uncertainty in the direct experimental measurements of the impulse per unit volume can be quantified. The estimated uncertainties in the pendulum arm length, measured pendulum deflection, pendulum mass, and the tube volume are given in Table 5. From this analysis, the total uncertainty in the direct impulse measurements due to the experimental setup was calculated to be at most ±4%.

Quantity	Range of values	Uncertainty
L_p	1.4-1.55 m	±0.0016 m
Δx	2-292 mm	±0.5 mm
m	12.808-55.483 kg	±0.001 kg
V	1.14-4.58×10^{-3} m^3	±4.5×10^{-8} m^3

Table 5: Uncertainties used in determining the error for experimentally measured impulse.

Uncertainties in the initial conditions were also quantified. The measured leak rate was 50 Pa/min from an initial pressure of 13 Pa. The maximum time required to complete the experiment was 15 minutes which results in a worst-case air contamination of 810 Pa. A study to identify the mixture most affected by this leak rate found stoichiometric ethylene-oxygen at an initial pressure of 30 kPa and initial temperature of 295 K to be the most sensitive case. An error analysis was then performed for this mixture to find the maximum uncertainty in initial conditions for all experiments. The analytical model[4] can be used to express I_V as a function of U_{CJ}, P_3, and c_3. The quantity ΔU_{CJ} is the difference in the Chapman-Jouguet velocity for a mixture containing an additional 810 Pa

of air as a result of the leak and the ideal case. STANJAN [21] was used to calculate U_{CJ} in each case. ΔP_3 and Δc_3 can then be found from differences in P_3 and c_3 for the two mixtures, where P_3 and c_3 are given by the relationships below, which are derived by using the method of characteristics to relate flow properties on either side of the Taylor wave[4],

$$\frac{P_3}{P_2} = \left(\frac{c_3}{c_2}\right)^{\frac{2\gamma}{\gamma-1}} = \left(\frac{\gamma+1}{2} - \frac{\gamma-1}{2}\frac{U_{CJ}}{c_2}\right)^{\frac{2\gamma}{\gamma-1}} . \tag{51}$$

Table 6 lists the calculated maximum changes in the flow parameters due to the leak rate. Also shown are the largest possible contributions due to uncertainty in the initial pressure because of gauge precision (±0.1 kPa) and due to uncertainty in the initial temperature (295-298 K). All uncertainties shown are calculated for comparison with the same ideal case specified above.

	Ideal	Dilution	Pressure	Temperature
P_1 (kPa)	30.0	30.0	30.1	30.0
T_1 (K)	295	295	295	298
U_{CJ} (m/s)	2317.9	2301.3	2307.5	2317.3
P_2 (kPa)	970.2	955.2	965.4	960.0
c_2 (m/s)	1249.	1240.	1243.	1249.
γ	1.23	1.23	1.23	1.23
P_3 (kPa)	318.5	314.8	317.2	315.3
c_3 (m/s)	1123.	1117.	1119.	1123.
ΔU_{CJ}(m/s)	-	16.6	10.4	0.6
ΔP_3 (Pa)	-	3620	1242	3185
Δc_3 (m/s)	-	6.2	4.6	0.040
ΔI_V	-	1.7%	0.6%	1.5%

Table 6: Variations in flow parameters resulting from uncertainty in initial conditions due to error in dilution (leak rate), initial pressure, and initial temperature as described in the text. The mixture chosen is stoichiometric C_2H_4-O_2 at an initial pressure of 30 kPa, which corresponds to the worst case of all the mixtures considered in experiments. The percentage error in I_V is based on the model predicted impulse.[4]

Combining the results in Table 6, the uncertainty in the impulse measurement due to the initial conditions is found to contribute at most ±2.3%, resulting in an overall maximum uncertainty of ±6.3% in ballistic measurements of the impulse.

Experimental repeatability was also considered. For experiments in which fast transition to detonation occurred, the impulse was repeatable to within ±0.7%. In cases where late DDT or fast flames were observed, the impulse in repeat experiments varied by as much as ±17% due to the turbulent nature of the flow during the initiation process. Additional experiments were conducted to verify that no out-of-plane motion existed during the initial pendulum swing.

The mass of the diaphragm was 0.27 g. For comparison, the mass of the ethylene-air mixture at 50 kPa (one of the lighter mixtures) is 3.3 g. Since the mass of the diaphragm is 8% of the total explosive mixture mass, we expect that in the worst case, this would have a tamping effect equivalent to adding an inert gas-filled extension that is 8% of the original tube length. We estimate[38] that this would have the effect of slightly (1-2%) increasing the impulse over the ideal (zero mass diaphragm) case. However, since the diaphragm is located at the end of the tube, the movement of the diaphragm away from the tube exit following the arrival of the detonation is expected to rapidly diminish the tamping effect.

Uncertainty in the DDT times was determined using the distance between two successive ionization probes and the Chapman-Jouguet velocity calculated with STANJAN[21] for each of the initial mixtures. In the experiments, transition to detonation was marked by a measured wave velocity greater than the calculated Chapman-Jouguet velocity followed by a relaxation to the expected detonation velocity. Thus, dividing the distance between two successive ionization gauges by the calculated detonation velocity (instead of the overdriven detonation velocity observed at the transition) results in an upper bound on the uncertainty of ± 46.4 μs.

13 Experimental Results

13.1 Detonation initiation regimes

As stated in the experimental setup, all mixtures were ignited by a spark with a discharge energy (30 mJ) less than the critical energy required for direct initiation of a detonation (approximately 283 kJ for propane-air mixtures[27] and approximately 56 kJ for ethylene-air mixtures[27] at atmospheric conditions). Thus, detonations were obtained only by transition from an initial deflagration. The presence of a deflagration is denoted by a gradual rise in the pressure histories as the unburned gas ahead of the flame is compressed due to the expansion of the burned gases behind the flame. If the correct conditions exist, this initial deflagration can transition to a detonation wave. Otherwise, transition will not occur and the deflagration wave will travel the entire length of the tube. An abrupt pressure jump (ΔP>2 MPa for hydrocarbon fuels) is indicative of this transition which can be quantified in terms of both the DDT time (from spark firing) and DDT distance (axial distance from ignition source location) required for the event to occur.

Through multiple experiments with varying mixtures and internal obstacles, pressure histories and ionization gauges data were used to identify several combustion regimes including the DDT process. The pressure transducers were protected by a layer of thermally-insulating vacuum grease. While this delays the onset of heating of the gauge surface, our experience is that eventually thermal artifacts will be produced in the signal. Although we have not quantified this for the present experiments, the pressure signals are reproducible and physically reasonable.

These different combustion regimes are categorized as fast transition to detonation (Figure 34), slow transition to detonation (Figure 35), fast flames (Figure 36), and slow

flames (Figure 37). Figure 34 illustrates the case of a fast transition to detonation, defined by an abrupt pressure increase before the first pressure transducer along the tube axis and the low DDT time. Figure 35 illustrates a slow transition to detonation case. An accelerating flame produces a gradual increase in pressure with time at the first and second pressure transducers, and transition to a detonation occurs between the second and third pressure transducers. In this case, the transition occurs late in the tube resulting in a longer DDT time. Figure 36 illustrates the case of a fast flame. The flame speed is fast enough to create significant compression waves but transition to detonation does not occur. Figure 37 illustrates the case of a slow flame. The flame speed is low and only smooth pressure waves of low amplitude (<0.5 MPa) are generated.

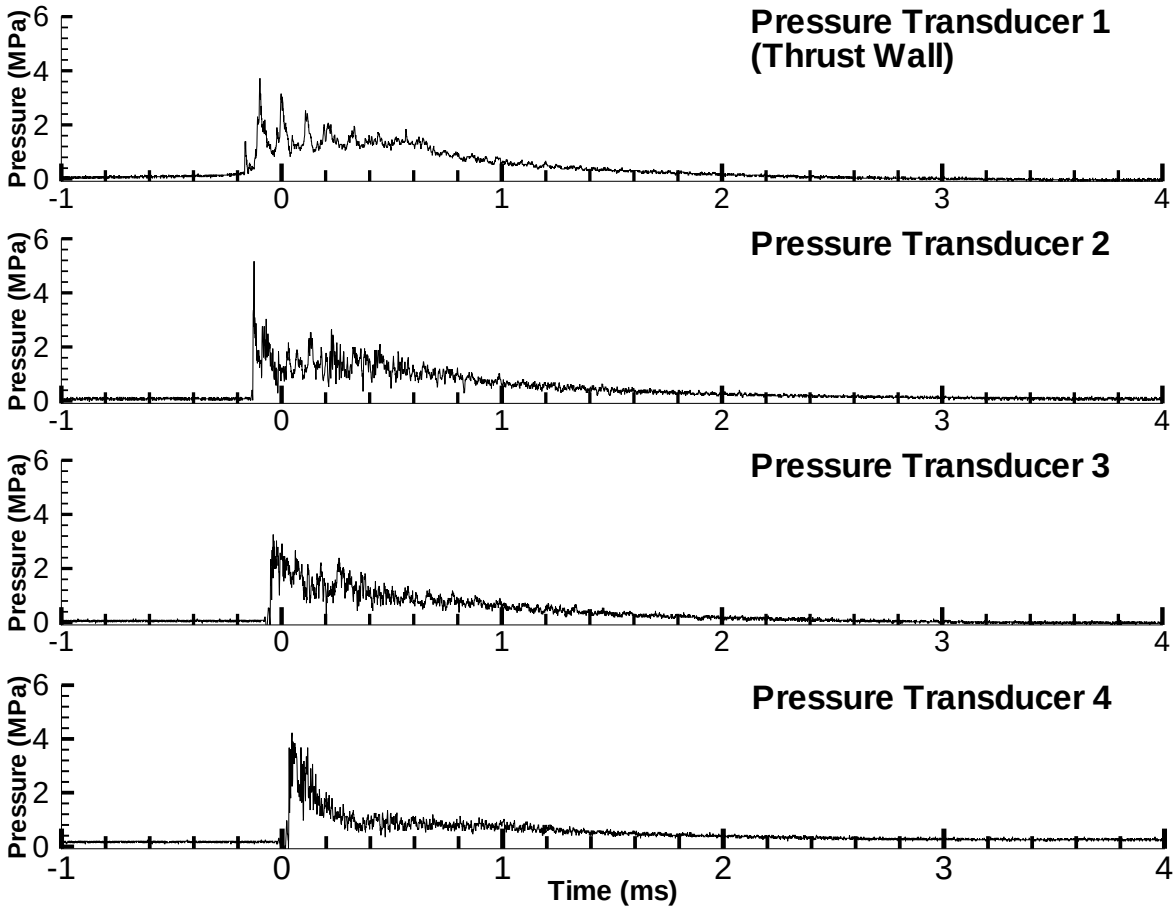

Figure 34: Pressure history recorded for a stoichiometric C_3H_8-O_2 mixture at 100 kPa initial pressure in the 0.609 m long tube illustrating the fast transition to detonation case.

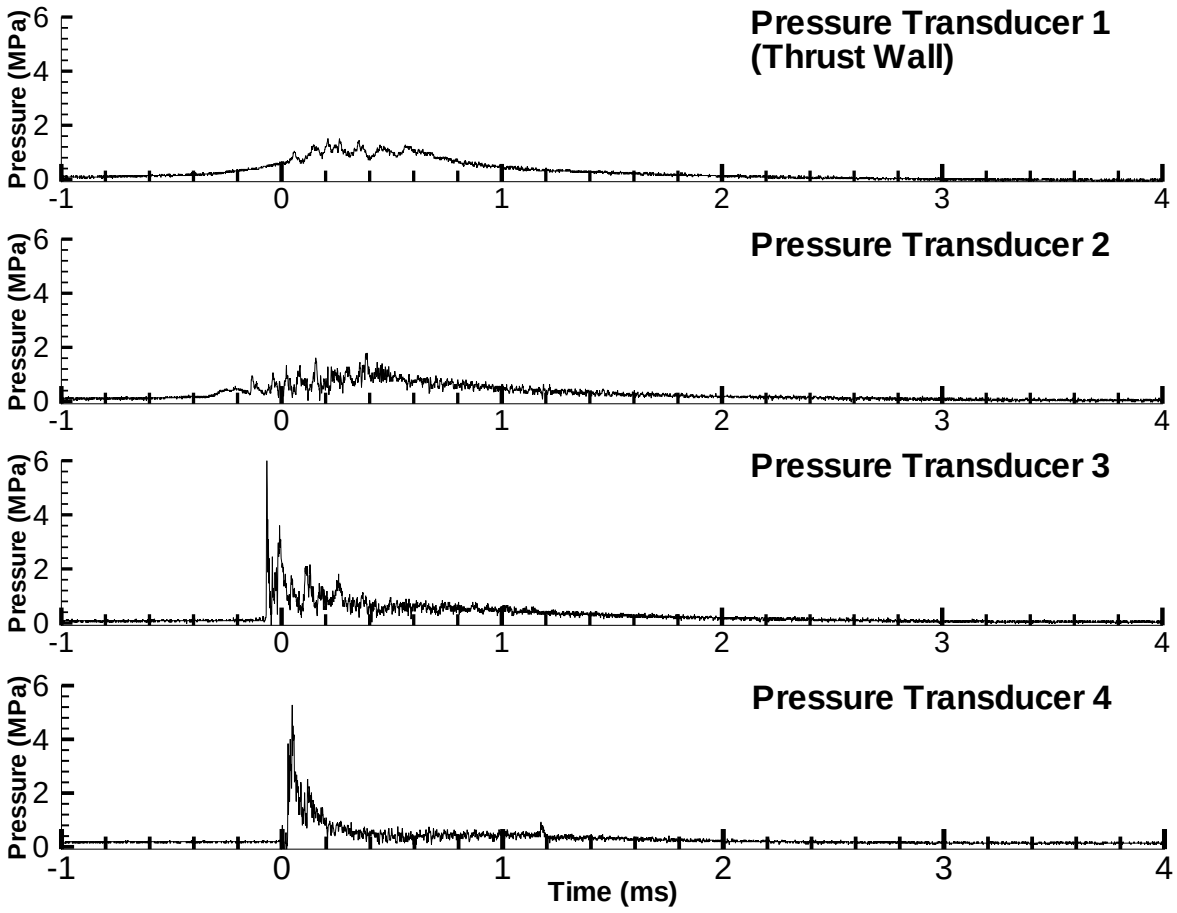

Figure 35: Pressure history recorded for a stoichiometric C_3H_8-O_2-N_2 mixture with $\beta = 1.5$ at 100 kPa initial pressure in the 0.609 m long tube illustrating the slow transition to detonation case.

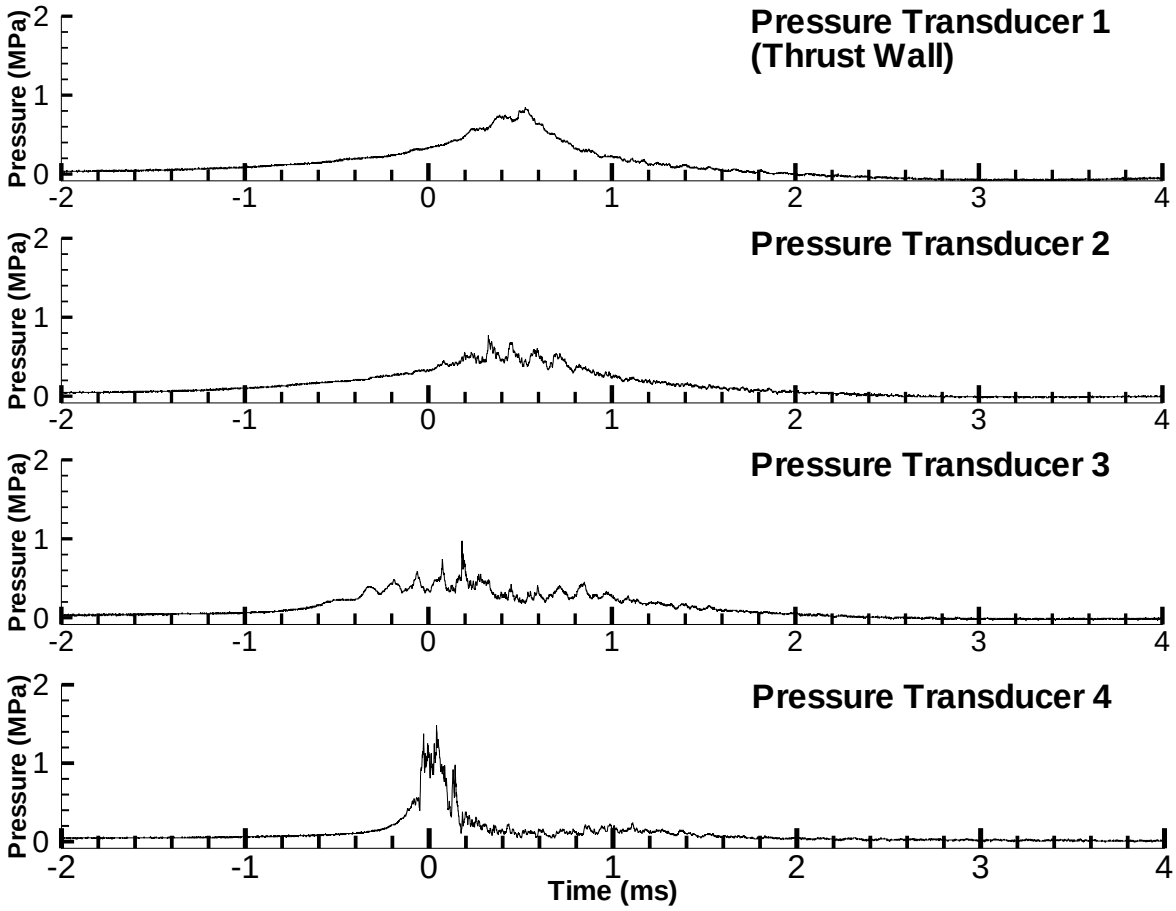

Figure 36: Pressure history recorded fpr a stoichiometric C_3H_8-O_2-N_2 mixture with $\beta = 3$ at 100 kPa initial pressure in the 0.609 m long tube illustrating the fast flame case.

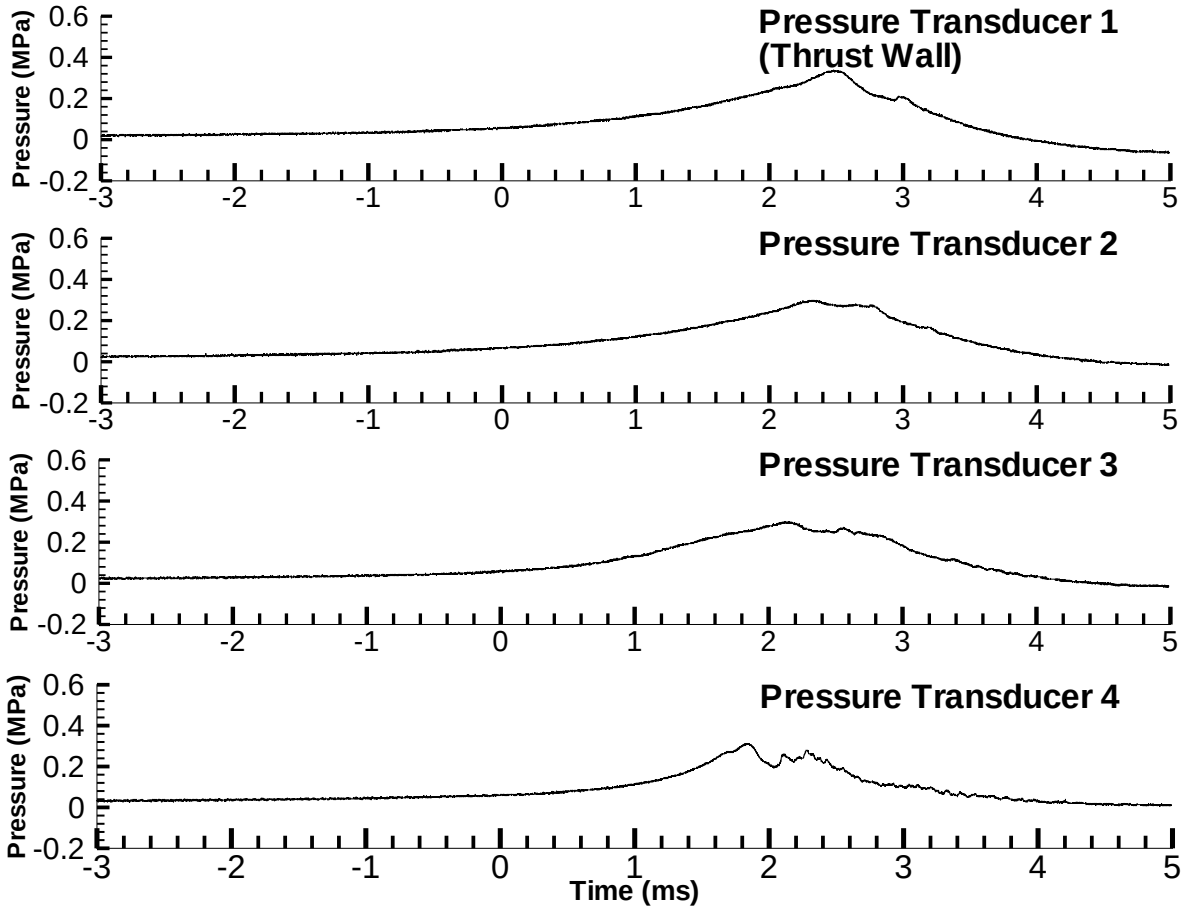

Figure 37: Pressure history recorded for a stoichiometric C_3H_8-air mixture at 100 kPa initial pressure in the 0.609 m long tube illustrating the slow flame case.

For cases when transition to detonation did occur, the DDT time was determined by measuring the combustion wave velocity and comparing this to the Chapman-Jouguet detonation velocity, U_{CJ}. The combustion wave velocity was estimated as the ratio of the distance between ionization probes to the time it took the reaction zone to pass from one ionization probe to the next. Transition is said to have occurred when this average combustion wave velocity is equal to or greater than the Chapman-Jouguet detonation velocity. The relative ability of the mixture to transition to detonation can be related to [31, 30] mixture properties such as the detonation cell size, expansion ratio, and deflagration speed. Necessary conditions for DDT are that the cell width be smaller than a specified fraction of the tube or obstacle dimensions, the expansion ratio (ratio of burned to unburned gas volume) must be larger than a minimum value, and that the deflagration speed exceeds a minimum threshold. For cases of a straight tube, transition to detonation is possible only if the detonation cell width is smaller than the tube diameter (unobstructed tube) or smaller than the obstacles' aperture (obstructed tube).

Figures 38 and 39 plot the DDT time for ethylene-oxygen-nitrogen mixtures in the 1.016 m long tube as a function of the initial pressure and diluent amount. Transition to detonation occurred in an unobstructed tube for mixtures at an initial pressure between 30 and 100 kPa and for mixtures up to 30% nitrogen. Since cell size increases with decreasing initial pressure and increasing dilution, the largest cell size was about 0.5 mm [27] corresponding to ethylene-oxygen at 30 kPa and about 0.6 mm [27] corresponding to ethylene-oxygen-nitrogen at 30% dilution. For these two cases, the inclusion of obstacles reduced the DDT time by an average of 65%. Additionally, the obstacles allowed DDT to occur in mixtures composed of up to 60% nitrogen (Figure 39), corresponding to an approximate cell size of 10 mm [27], as compared with DDT being achieved only up to 30% nitrogen in a tube with no obstacles. Thus, the presence of obstacles enabled mixtures with more diluent (less sensitive mixtures with a larger cell size) to transition to detonation, but there are limits to obstacle effectiveness. This is illustrated by the ethylene-air (74% nitrogen dilution) mixture with an approximate cell size of 29 mm [27] which did not transition to a detonation. Wintenberger et al.[4] have used the ideas of Dorofeev et al.[31] to estimate limits for DDT in obstructed tubes that are consistent with our observations.

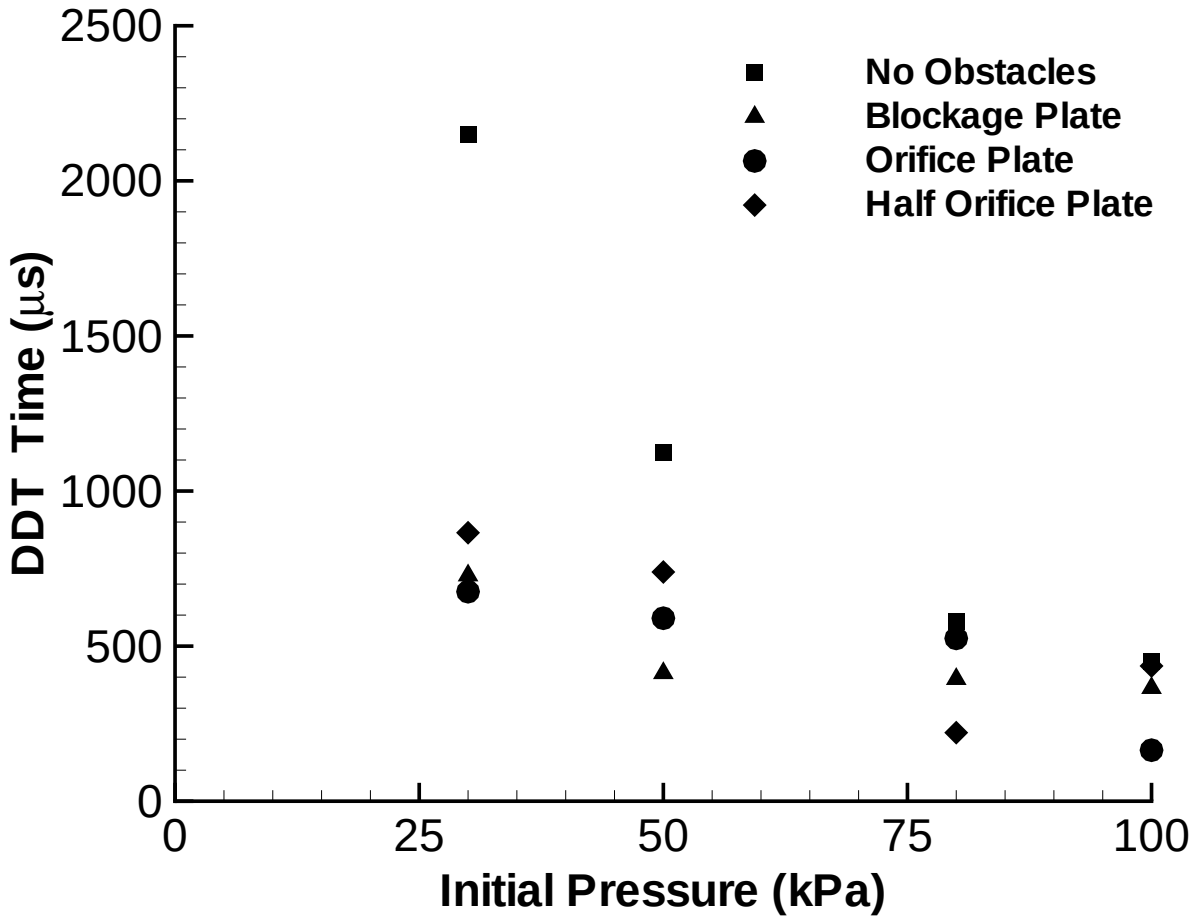

Figure 38: Measured DDT time for stoichiometric C_2H_4-O_2 mixtures with varying initial pressure for three obstacle configurations in the 1.016 m long tube.

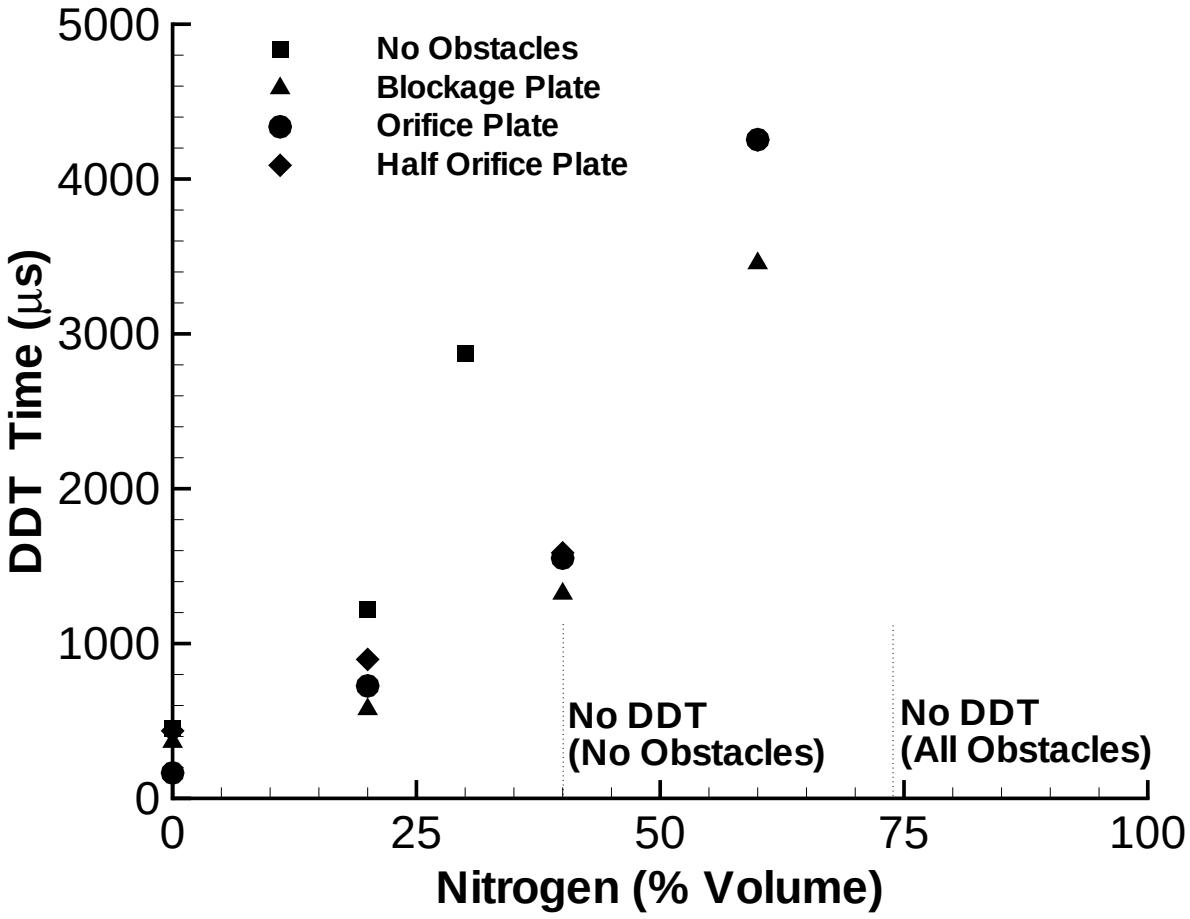

Figure 39: Measured DDT time for stoichiometric C_2H_4-O_2 mixtures with varying nitrogen dilution at 100 kPa initial pressure for three obstacle configurations in the 1.016 m long tube.

13.2 Impulse measurements

The following two sections present single-cycle impulse measurements with internal obstacles. To facilitate comparison between the different tube sizes, the results are given in terms of impulse normalized by the tube volume, I_V, as well as the mixture-based specific impulse, I_{sp}. The figures also show predicted impulse values from a model[4] that is based on analysis of the gas dynamic processes in the tube. The model impulse values are generally within 15% of the experimental impulse values over the range of pressures and diluent amounts studied. Wintenberger et al.[4] provide additional discussion of differences between the experimental and model impulse values. As seen in both the measured and model data[4], the impulse per unit volume increases linearly with increasing initial pressure while the specific impulse tends to a constant value. The measured and model data[4] also show that both the impulse per unit volume and specific impulse decrease with increasing nitrogen dilution. This is due to the reduced amount of fuel present in a given volume of mixture with increasing amounts of dilution, which reduces the total energy released during combustion.

13.2.1 Experiments with spiral obstacles

Direct impulse measurements for propane-oxygen-nitrogen mixtures were made in two tubes of lengths of 0.609 m and 1.5 m with different Shchelkin spiral configurations. Figure 40 shows impulse as a function of initial pressure for both tubes and Figure 41 shows impulse as a function of diluent amount for the 0.609 m tube only.

From Figure 40, it can be seen that the obstacles with a smaller pitch cause a greater reduction in impulse than those with a larger pitch. We attribute this loss in impulse as being due to a greater form drag associated with the flow around the obstacles as the spiral pitch decreases. At 100 kPa, a 5% reduction in the distance between successive coils causes a 13% reduction in impulse if the spirals extend over the entire tube length.

If DDT does not occur, the impulse is reduced (Figure 41). DDT limits were discussed in the previous section, but now the effect of late or no DDT on impulse can be investigated. As the mixture sensitivity decreases with increasing dilution, it becomes progressively more difficult to initiate a detonation within the tube. For large amounts of diluent, DDT does not occur within the tube and only deflagrations are observed (Figures 36 and 37). Deflagrations propagate down the tube at a relatively slower flame speed compressing the unburned gas ahead of the flame. This unburned gas compression is sufficient to rupture the thin diaphragm causing a considerable part of the mixture to be ejected outside the tube. Observations made by Jones and Thomas[39] clearly demonstrate the gas motion and compression waves ahead of the flame. The mixture ejected from the tube does not contribute to the impulse due to its unconfined burning. The effect of this mixture spillage due to no DDT can be seen in the cases with greater than 70% diluent where a 30-50% reduction in impulse is observed. The onset of a detonation wave can mitigate this effect due to its higher propagation speed. If DDT occurs early enough in the process, the detonation can overtake the compression waves created by the deflagration before they reach the diaphragm. The loss associated with this phenomenon

is expected to become significant when DDT occurs in the last quarter of the tube, so that the detonation does not have time to catch up with the deflagration compression waves. Cases of late or no DDT illustrate the importance of more sophisticated initiation methods for less sensitive fuels, such as storable liquid hydrocarbons (Jet A, JP-8, JP-5 or JP-10) with cell widths similar to propane. Experiments with more sensitive ethylene-oxygen-nitrogen mixtures show that using obstacles to induce DDT within the tube can be effective.

13.2.2 Experiments with orifice and blockage plate obstacles

Impulse measurements for ethylene-oxygen mixtures in the 1.016 m long tube appear in Figure 42 as a function of initial pressure and Figure 43 as a function of nitrogen dilution. Also shown are the analytical model predictions[4]. Without obstacles, detonation cannot be achieved in this tube for nitrogen dilutions of 40% or greater. A dramatic drop in measured impulse results for these mixtures (Figure 43). The addition of obstacles enabled DDT to occur in mixtures up to 60% nitrogen dilution. Beyond this point, the cell width is sufficiently large that transition to detonation occurs only in the latter portion of the tube and not all of the mixture burns within the tube.

Although obstacles can induce DDT in less sensitive mixtures and significantly increase the impulse, the obstacle drag can decrease the impulse by an average of 25% from the value measured without obstacles when fast transition to a detonation occurs (Figure 42). This impulse loss is due to additional drag from the obstacles and added heat transfer to the obstacles reducing the energy available for conversion into thrust.

14 Effect of extensions

Proposed concepts for pulse detonation engines have often included the addition of different kinds of extensions, including nozzles, to the basic straight detonation tube. In part, this is motivated by the effectiveness of converging-diverging nozzles in conventional rocket motors. The effectiveness of a converging-diverging nozzle is based on the steady flow conversion of the thermal to kinetic energy. However, the pulse detonation engine is an unsteady device that relies on waves to convert the thermal energy into kinetic energy. It is not obvious how a nozzle would affect performance since the diffraction of the detonation wave through a nozzle is a complex process that involves significant losses.

We have approached this problem experimentally by examining the effect of various exit treatments on the measured impulse. Previous experiments by Zhdan et al.[10] with straight cylindrical extensions indicate that the mixture-based specific impulse will increase as the ratio of the overall tube length, L_t, to the tube length filled with combustible gases, L, increases. Note that the mass of air in the extension volume is not included in the mixture mass used to compute the specific impulse. In our tests, as in Zhdan et al.[10], a thin diaphragm separates the tube length filled with the combustible mixture from the extension, which was filled with air at atmospheric conditions. This simulates the condition of having a single tube only partially filled with explosive mixture.

14.1 Extensions tested

Three different extensions were tested on the detonation tube with a length of 1.016 m in a ballistic pendulum arrangement to determine their effect on the impulse. Each extension modified the total tube length, L_t, while the charge length, L, remained constant.

The first extension was a flat plate ($L_t/L = 1$) or flange with an outer diameter of 0.381 m that extended radially in the direction perpendicular to the tube's exhaust flow. A hole located in the center of the plate matched the tube's inner diameter, thus increasing the apparent wall thickness at the exhaust end from 0.0127 m to 0.1524 m. The purpose of this flange was to see if the pressure behind the diffracting shock wave would contribute significantly to the specific impulse. In effect, this examines the role of the last term (wall thickness) of Equation 49 in the momentum control volume analysis. The second extension was a straight cylinder ($L_t/L = 1.6$) with a length of 0.609 m. This extension simulated a partial fill case. The third extension was a diverging conical nozzle ($L_t/L = 1.3$) with a half angle of eight degrees and a length of 0.3 m.

14.2 Impulse measurements

The flat plate and straight extension were tested with ethylene-oxygen-nitrogen mixtures on a tube that did not contain internal obstacles (Figure 44).

The flat plate extension yielded a maximum specific impulse increase of 5% at 0% nitrogen dilution which is within our uncertainty in measured impulse. This effect can be understood by recognizing that the flat plate or flange extension has a minimal effect on the impulse since the shock Mach number decays very quickly as the shock diffracts out from the open end. The amount of impulse contributed by the pressure of the decaying shock is relatively small compared to that obtained from the pressure of the detonation products on the thrust surface at the closed end of the tube. In addition, the rate of pressure decrease at the exit is relatively unaffected by the flange so that the rate of pressure decay at the thrust surface is very similar with and without the flat plate. At 40% nitrogen dilution, DDT did not occur and the flat plate extension decreased the impulse by 7%. This percentage decrease is within the experimental uncertainty for cases with late or no DDT, preventing any conclusion about the plate's performance for this test case.

The straight extension increased the measured specific impulse by 18% at 0% nitrogen dilution, whereas a 230% increase in the specific impulse was observed at 40% nitrogen dilution. This large increase in the specific impulse occurred since the additional tube length enabled DDT to occur in the extension's confined volume.

To better isolate the effect of the extensions over the range of diluent percentages tested, cases of late or no DDT were eliminated by the addition of the "Half orifice plate" obstacles (Figure 33). Both the straight extension and diverging nozzles were tested as a function of diluent amount (Figure 45). The flat plate extension was not retested due to its small effect on the measured impulse shown previously. The straight extension attached to a tube with internal obstacles increased the specific impulse by an average of 13%. As shown above, the straight extension attached to a tube without

internal obstacles increased the impulse by 18%. This 5% reduction in impulse is due to drag and heat transfer losses induced by the obstacles. The diverging nozzle had a minor effect, increasing the specific impulse by an average of 1%, which is within the experimental uncertainty.

The straight extension was more effective than the diverging nozzle in increasing impulse (Figure 45). One explanation[40, 10] of this effect is that the additional length of the straight extension as compared with the diverging extension delays the arrival of the expansion wave from the tube exit, effectively increasing the pressure relaxation time and the impulse. Standard gas dynamics considerations indicate that two reflected waves will be created when an extension filled with inert gas is added to a detonation tube. The first wave is due to the interaction of the detonation with the mixture-air interface and is much weaker than the wave created by the shock or detonation diffraction at the tube exit. Additionally, the continuous area change of the diverging nozzle creates expansion waves that propagate back to the thrust surface resulting in a gradual but continuous decrease in pressure that starts as soon as the detonation reaches the entrance to the diverging nozzle. Another way to interpret these impulse results with added extensions is that the added inert gas provides additional tamping[38] of the explosion which will increase the momentum transfer from the detonation products to the tube.

15 Summary and Conclusion

Single-cycle impulse measurements were made for deflagrations and detonations initiated with a 30 mJ spark in three tubes of different lengths and inner diameters. A ballistic pendulum arrangement was used and the measured impulse values were compared to those obtained from an analytical model[4]. The measured impulse values were estimated to have an uncertainty of $\pm 6.3\%$ in cases where DDT occurred sufficiently early within the tube. By studying the pressure histories measured at several locations in the tube, four internal flow regimes were identified. Internal obstacles, with a constant blockage ratio of 0.43, were used to reduce DDT times and initiate detonations in insensitive mixtures such as those with a high diluent amount. Times to transistion were measured with ionization probes. The internal obstacles were found to reduce DDT times for insensitive mixtures and even enable highly insensitive mixtures (up to 60% dilution in ethylene-oxygen mixtures) to transition. However, the effectiveness of the obstacles is limited since detonations could not be obtained in ethylene-air (75% dilution) in the 1.016 m tube. It was determined that those regimes in which slow or no transition to detonation occurred resulted in impulse values 30-50% lower than model[4] predictions. For cases of fast transition to detonation, the inclusion of obstacles decreased the measured impulse by an average of 25% as compared with the measured impulse for a tube without internal obstacles.

The effect of different exit arrangements was studied by using three different types of extensions. A relationship between the overall length-to-charge length (L_t/L) ratio and impulse was observed. The straight extension, with a L_t/L ratio of 1.6, resulted in

the greatest increase in impulse of 18% at 0% dilution and no internal obstacles. This increase in impulse is due to the increase in momentum transfer to the tube due to the additional mass contained in the extension.

The results of this experimental work have several significant implications for pulse detonation engine technology. The use of internal obstacles may be effective in initiating detonations in highly insensitive mixtures of larger cell widths such as all the storable liquid hydrocarbon fuels. However, because there are limits to obstacle effectiveness, their use will have to be optimized for a given mixture and application. The use of extensions may also be beneficial in augmenting the specific impulse obtainable from a given fuel-oxidizer mass. However, the maximum impulse is always obtained by filling the available tube volume entirely with the combustible mixture. Additional studies in progress are required to quantify the effect on impulse that could be obtained with diverging and converging-diverging nozzles.

16 Acknowledgment

This work was supported by the Office of Naval Research Multidisciplinary University Research Initiative *Multidisciplinary Study of Pulse Detonation Engine* (grant 00014-99-1-0744, sub-contract 1686-ONR-0744), and General Electric contract GE-PO A02 81655 under DABT-63-0-0001.

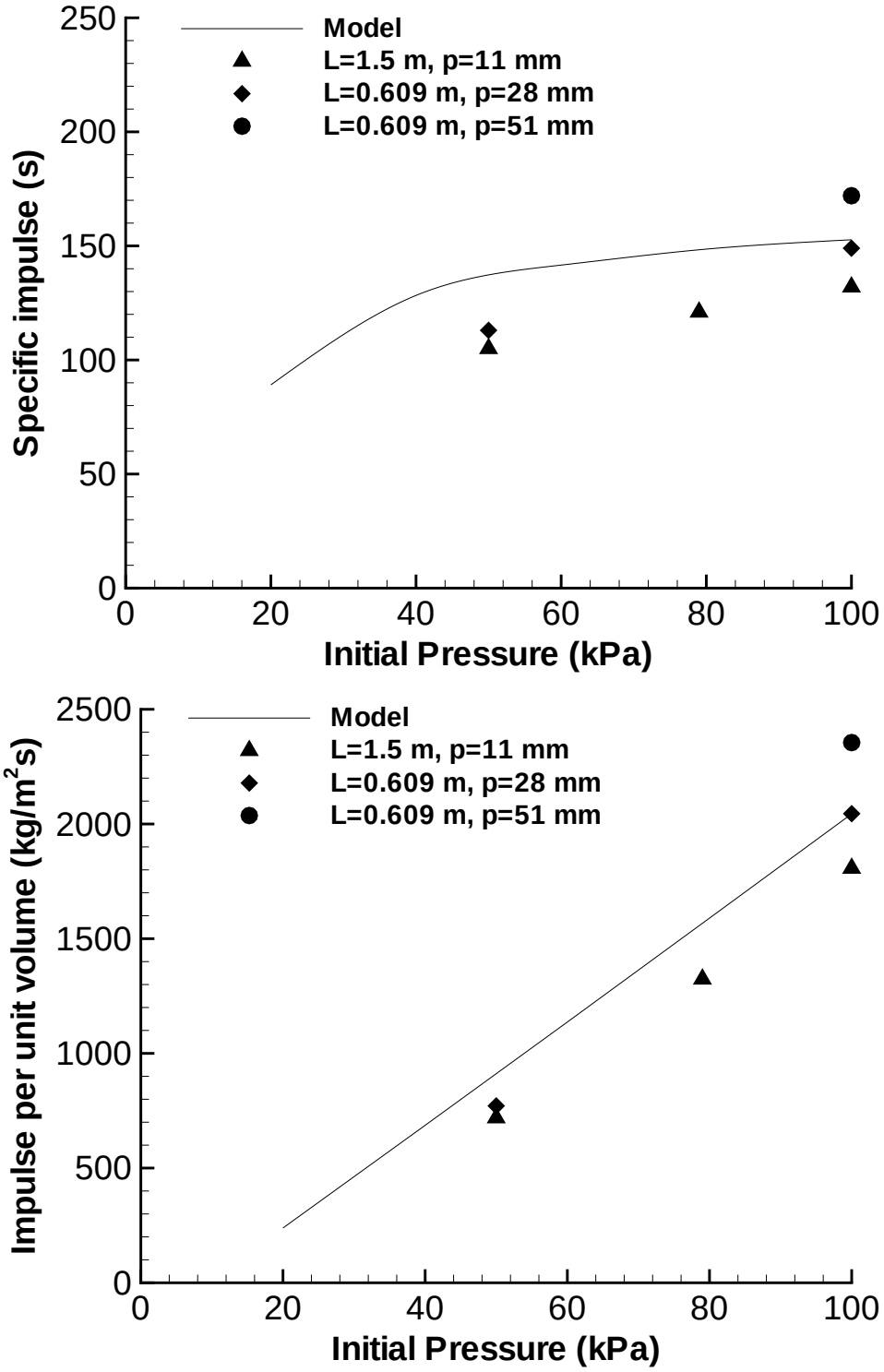

Figure 40: Impulse measurements for stoichiometric C_3H_8-O_2 mixtures with varying initial pressure in the 1.5 m and 0.609 m long tubes.

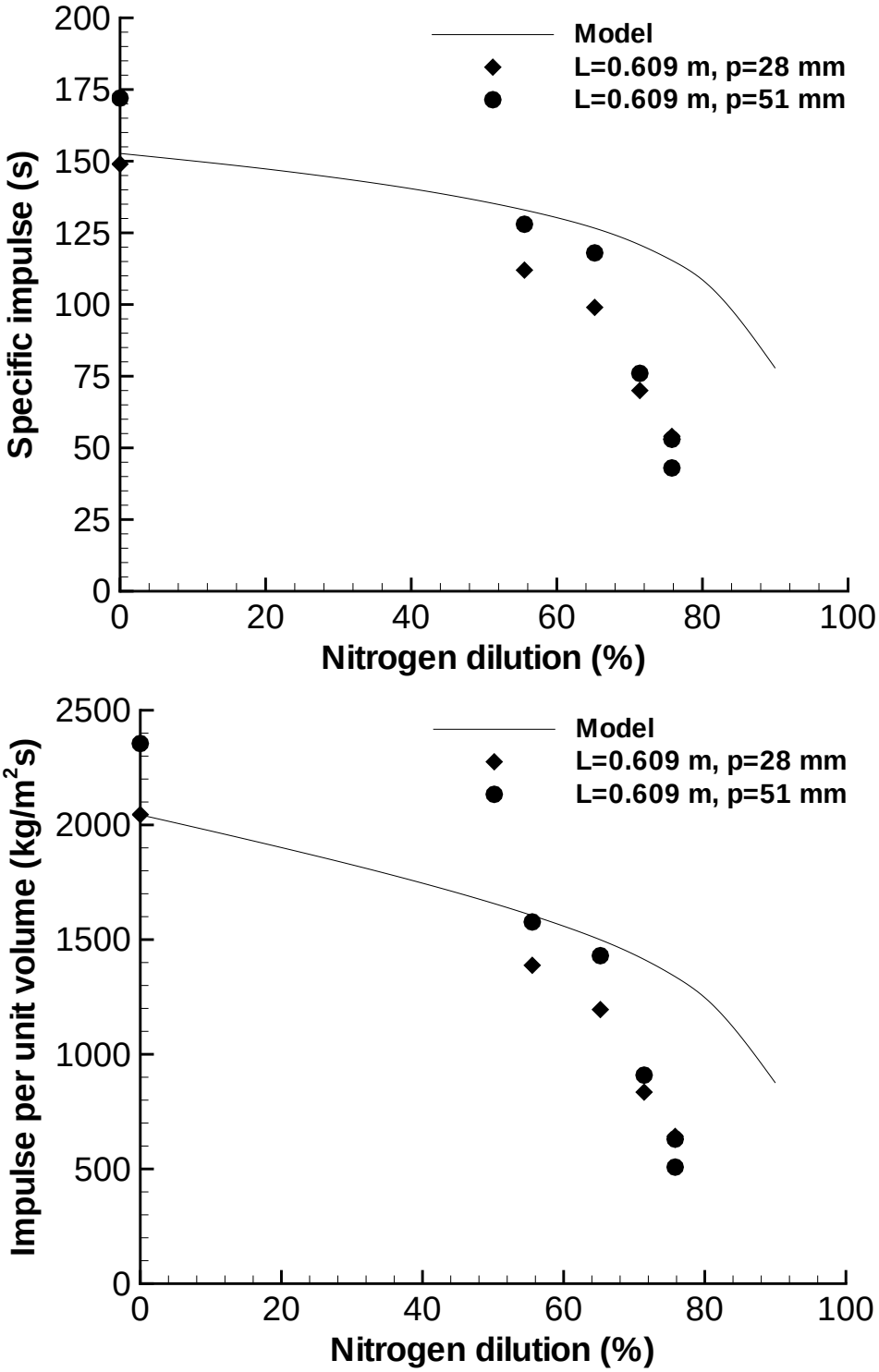

Figure 41: Impulse measurements for stoichiometric C_3H_8-O_2 mixtures with varying nitrogen dilution at 100 kPa initial pressure in the 0.609 m long tube.

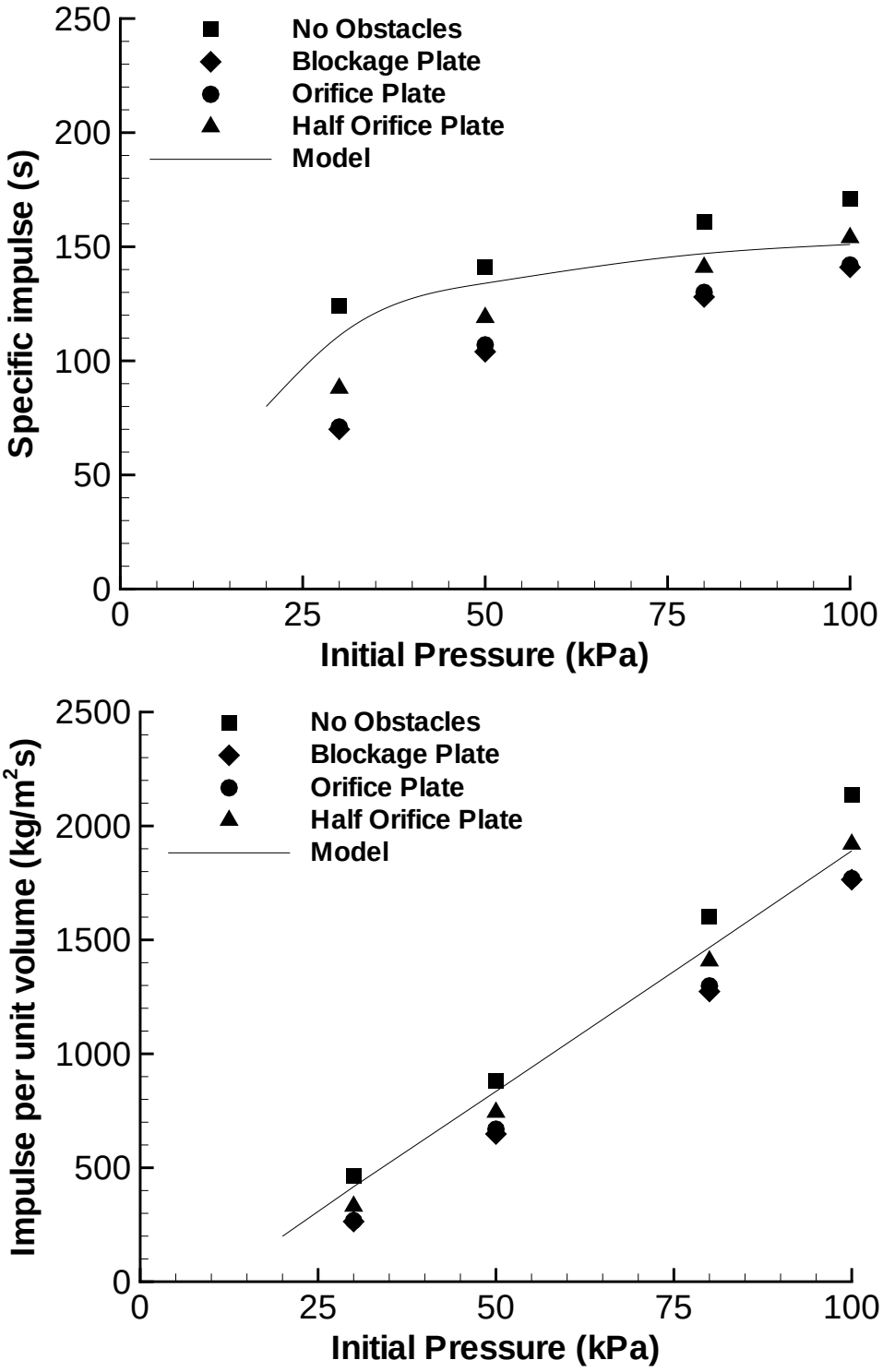

Figure 42: Impulse measurements for stoichiometric C_2H_4-O_2 mixtures with varying initial pressure in the 1.016 m long tube.

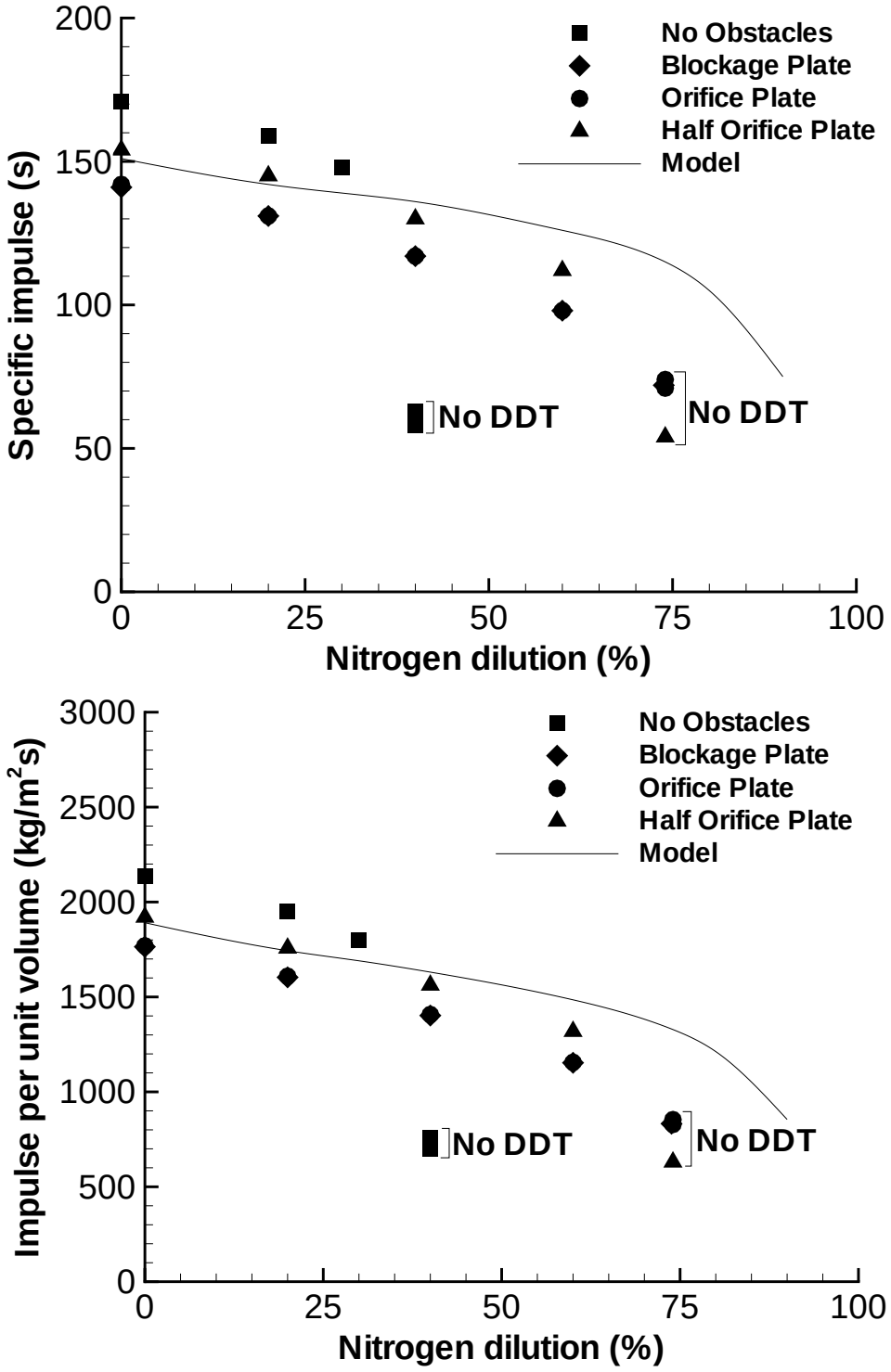

Figure 43: Impulse measurements for stoichiometric C_2H_4-O_2 mixtures with varying nitrogen dilution at 100 kPa initial pressure in the 1.016 m long tube.

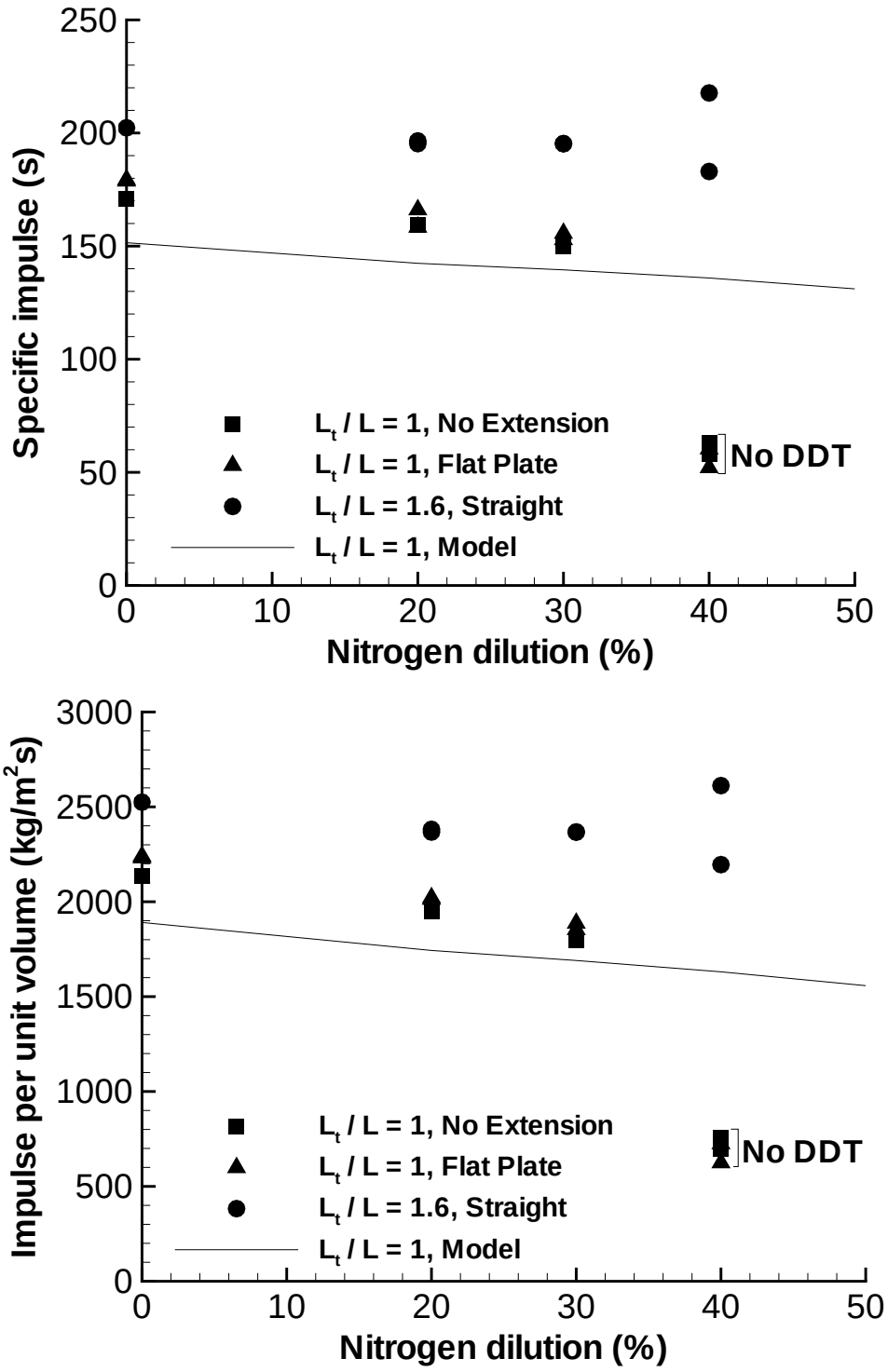

Figure 44: Specific impulse for stoichiometric C_2H_4-O_2 mixtures at 100 kPa initial pressure with varying diluent and no internal obstacles.

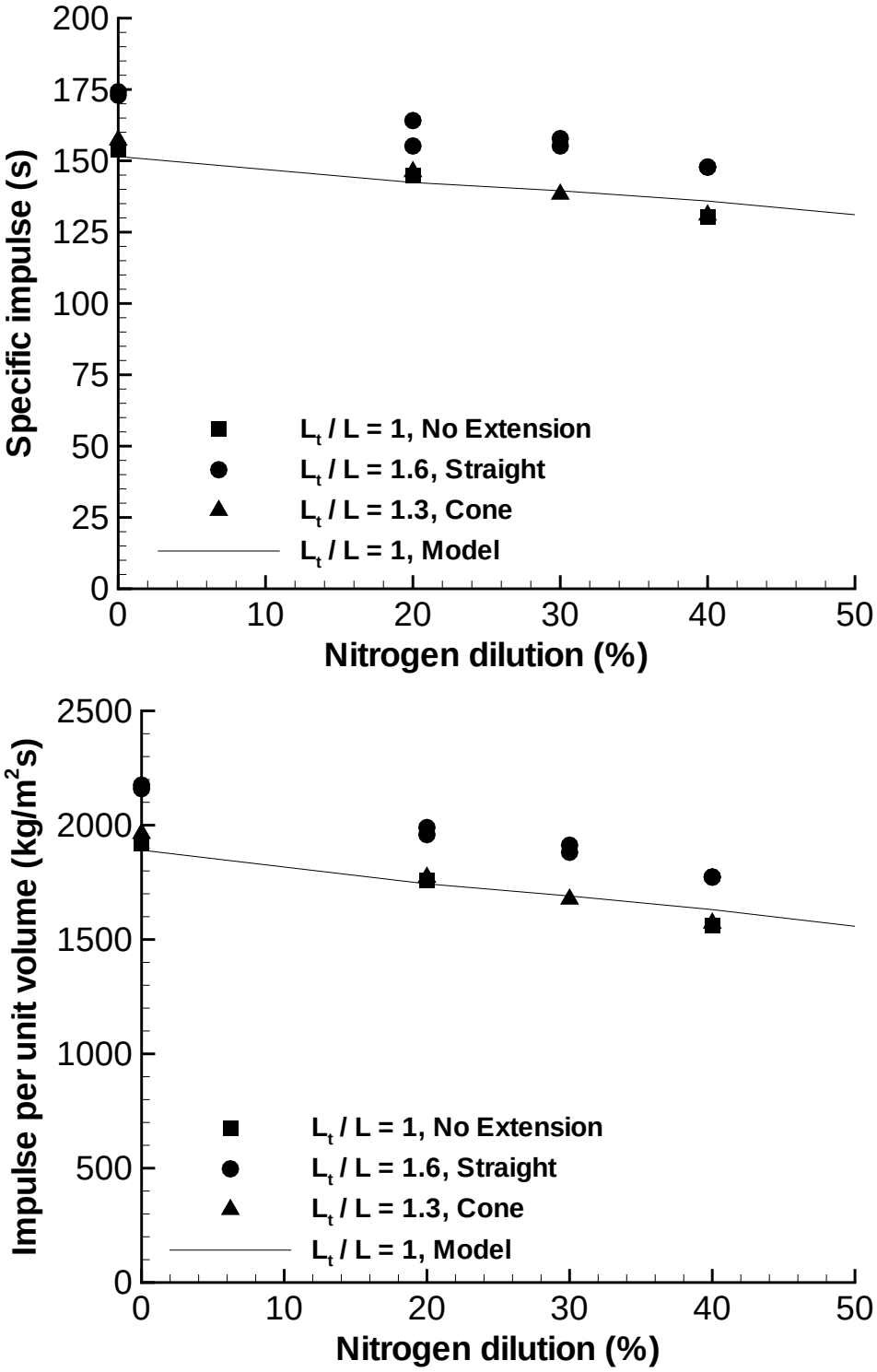

Figure 45: Specific impulse for stoichiometric C_2H_4-O_2 mixtures at 100 kPa initial pressure with varying diluent and "Half Orifice Plate" internal obstacles.

Part IV
References

References

[1] Cooper, M., Jackson, S., Austin, J., Wintenberger, E., and Shepherd, J. E., "Direct Experimental Impulse Measurements for Deflagrations and Detonations," 37th AIAA/ASME/SAE/ASEE Joint Propulsion Conference, July 8–11, 2001, Salt Lake City, UT, AIAA 2001-3812.

[2] Schauer, F., Stutrud, J., and Bradley, R., "Detonation Initiation Studies and Performance Results for Pulsed Detonation Engines," 39th AIAA Aerospace Sciences Meeting and Exhibit, January 8–11, 2001, Reno, NV, AIAA 2001-1129.

[3] Schauer, F., Stutrud, J., Bradley, R., Katta, V., and Hoke, J., "Detonation Initiation and Performance in Complex Hydrocarbon Fueled Pulsed Detonation Engines," 50th JANNAF Propulsion Meeting, Paper I-05, July 11–13, 2001, Salt Lake City, UT.

[4] Wintenberger, E., Austin, J., Cooper, M., Jackson, S., and Shepherd, J. E., "An Analytical Model for the Impulse of a Single-Cycle Pulse Detonation Engine," 37th AIAA/ASME/SAE/ASEE Joint Propulsion Conference, July 8–11, 2001, Salt Lake City, UT, AIAA 2001-3811.

[5] Sterling, J., Ghorbanian, K., Humphrey, J., Sobota, T., and Pratt, D., "Numerical Investigations of Pulse Detonation Wave Engines," 31st AIAA/ASME/SAE/ASEE Joint Propulsion Conference and Exhibit, July 10–12, 1995. San Diego, CA. AIAA 95–2479.

[6] Bussing, T. R. A. and Pappas, G., "Pulse Detonation Engine Theory and Concepts," *Developments in High-Speed Vehicle Propulsion Systems*, Vol. 165 of *Progress in Aeronautics and Astronautics*, AIAA, 1996, pp. 421–472.

[7] Bussing, T. R. A., Bratkovich, T. E., and Hinkey, J. B., "Practical Implementation of Pulse Detonation Engines," 33rd AIAA/ASME/SAE/ASEE Joint Propulsion Conference and Exhibit, July 6–9, 1997, Seattle, WA, AIAA 97-2748.

[8] Cambier, J. L. and Tegner, J. K., "Strategies for Pulsed Detonation Engine Performance Optimization," *Journal of Propulsion and Power*, Vol. 14, No. 4, 1998, pp. 489–498.

[9] Kailasanath, K. and Patnaik, G., "Performance Estimates of Pulsed Detonation Engines," *Proceedings of the 28th International Symposium on Combustion*, The Combustion Institute, 2000, pp. 595–601.

[10] Zhdan, S. A., Mitrofanov, V. V., and Sychev, A. I., "Reactive Impulse from the Explosion of a Gas Mixture in a Semi-infinite Space," *Combustion, Explosion and Shock Waves*, Vol. 30, No. 5, 1994, pp. 657–663.

[11] Heiser, W. H. and Pratt, D. T., "Thermodynamic Cycle Analysis of Pulse Detonation Engines," *Journal of Propulsion and Power*, Vol. 18, No. 1, 2002, pp. 68–76.

[12] Zitoun, R. and Desbordes, D., "Propulsive Performances of Pulsed Detonations," *Comb. Sci. Tech.*, Vol. 144, 1999, pp. 93–114.

[13] Harris, P. G., Farinaccio, R., and Stowe, R. A., "The Effect of DDT Distance on Impulse in a Detonation Tube," 37th AIAA/ASME/SAE/ASEE Joint Propulsion Conference and Exhibit, July 8–11, 2001, Salt Lake City, UT, AIAA 2001-3467.

[14] Nicholls, J. A., Wilkinson, H. R., and Morrison, R. B., "Intermittent Detonation as a Thrust-Producing Mechanism," *Jet Propulsion*, Vol. 27, No. 5, 1957, pp. 534–541.

[15] Endo, T. and Fujiwara, T., "A Simplified Analysis on a Pulse Detonation Engine," *Trans. Japan Soc. Aero. Space Sci.*, Vol. 44, No. 146, 2002, pp. 217–222.

[16] Stanyukovich, K. P., *Unsteady Motion of Continuous Media*, Pergamon Press, 1960, pp. 142–196.

[17] Kailasanath, K., Patnaik, G., and Li, C., "Computational Studies of Pulse Detonation Engines: A Status Report," 35th AIAA/ASME/SAE/ASEE Joint Propulsion Conference and Exhibit, 20-24 June, 1999, Los Angeles, CA, AIAA 1999-2634.

[18] Kailasanath, K., "Recent Developments in the Research on Pulse Detonation Engines," 40th AIAA Aerospace Sciences Meeting and Exhibit, January 14–17, 2002, Reno, NV, AIAA 2002-0470.

[19] Zel'dovich, Y. B., "On the Theory of the Propagation of Detonations in Gaseous Systems," *Journal of Experimental and Theoretical Physics*, Vol. 10, 1940, pp. 542–568, Available in translation as NACA TM 1261 (1950).

[20] Taylor, G. I., "The Dynamics of the Combustion Products behind Plane and Spherical Detonation Fronts in Explosives," *Proc. Roy. Soc.*, Vol. A200, 1950, pp. 235–247.

[21] Reynolds, W. C., "The Element Potential Method for Chemical Equilibrium Analysis: Implementation in the Interactive Program STANJAN, Version 3," Tech. rep., Dept. of Mechanical Engineering, Stanford University, Stanford, CA, January 1986.

[22] Thompson, P. A., *Compressible Fluid Dynamics*, Rensselaer Polytechnic Institute Bookstore, Troy, NY, 1988, pp. 347–359.

[23] Fickett, W. and Davis, W. C., *Detonation Theory and Experiment*, chap. 2, Dover Publications Inc., 2001, pp. 16–20.

[24] Glass, I. I. and Sislian, J. P., *Nonstationary Flows and Shock Waves*, chap. 4, Clarendon Press, Oxford Science Publications, 1994.

[25] Hornung, H., Computations carried out at GALCIT, California Institute of Technology, Pasadena, CA. August 2000.

[26] Quirk, J. J., "AMRITA - A Computational Facility (for CFD Modelling)," VKI 29th CFD Lecture Series, ISSN 0377-8312, 1998.

[27] Shepherd, J. E. and Kaneshige, M., "Detonation Database," Tech. Rep. GALCIT Report FM97-8, California Institute of Technology, 1997, Revised 2001 - see www.galcit.caltech.edu/detn_db/html for the most recent version.

[28] Zel'dovich, Y., Kogarko, S., and Simonov, N., "An Experimental Investigation of Spherical Detonation," *Soviet Phys. Tech. Phys.*, Vol. 1, No. 8, 1956, pp. 1689–1713.

[29] Lee, J., "Dynamic Parameters of Gaseous Detonations," *Ann. Rev. Fluid Mech.*, Vol. 16, 1984, pp. 311–316.

[30] Dorofeev, S., Kuznetsov, M., Alekseev, V., Efimenko, A., and Breitung, W., "Evaluation of Limits for Effective Flame Acceleration in Hydrogen Mixtures," *Journal of Loss Prevention in the Process Industries*, Vol. 14, No. 6, 2001, pp. 583–589.

[31] Dorofeev, S., Sidorov, V. P., Kuznetzov, M. S., Matsukov, I. D., and Alekseev, V. I., "Effect of Scale on the Onset of Detonations," *Shock Waves*, Vol. 10, 2000.

[32] Chao, T., Wintenberger, E., and Shepherd, J. E., "On the Design of Pulse Detonation Engines," GALCIT Report FM00-7, Graduate Aeronautical Laboratories, California Institute of Technology, Pasadena, CA 91125, 2001.

[33] Sutton, G. P., *Rocket Propulsion Elements*, Wiley-Interscience, 5th ed., 1986.

[34] Hill, P. G. and Peterson, C. R., *Mechanics and Thermodynamics of Propulsion*, Addison-Wesley, 2nd ed., 1992.

[35] Lindstedt, R. P. and Michels, H. J., "Deflagration to Detonation Transitions and Strong Deflagrations in Alkane and Alkene Air Mixtures," *Combust. Flame*, Vol. 76, 1989, pp. 169–181.

[36] Cooper, M., Jackson, S., and Shepherd, J. E., "Effect of Deflagration-to-Detonation Transition on Pulse Detonation Engine Impulse," GALCIT Report FM00-3, Graduate Aeronautical Laboratories, California Institute of Technology, Pasadena, CA 91125, 2000.

[37] Bevington, P. R., *Data Reduction and Error Analysis in the Physical Sciences*, McGraw-Hill, 1969.

[38] Kennedy, J. E., "The Gurney Model of Explosive Output for Driving Metal," *Explosive Effects and Applications*, edited by J. A. Zuker and W. P. Walters, chap. 7, Springer, New York, 1998, pp. 221–257.

[39] Jones, S. A. S. and Thomas, G. O., "Pressure Hot-Wire and Laser Doppler Anemometer Studies of Flame Acceleration in Long Tubes," *Combust. Flame*, Vol. 87, 1991, pp. 21–32.

[40] Chiping, L., Kailasanath, K., and Patnaik, G., "A Numerical Study of Flow Field Evolution in a Pulsed Detonation Engine," 38th AIAA Aerospace Sciences Meeting and Exhibit, January 10–13, 2000, Reno, NV, AIAA 2000–0314.

Part V
Appendices

A Ideal Detonation Model

The Chapman-Jouguet model of an ideal detonation can be combined with the Taylor-Zeldovich similarity solution to obtain an analytic solution to the flow field behind a steadily-propagating detonation in a tube. This solution can be constructed piecewise by considering the three regions shown on Figure 46; the stationary reactants ahead of the detonation mixture; the expansion wave behind the detonation; and the stationary products next to the closed end of the tube.

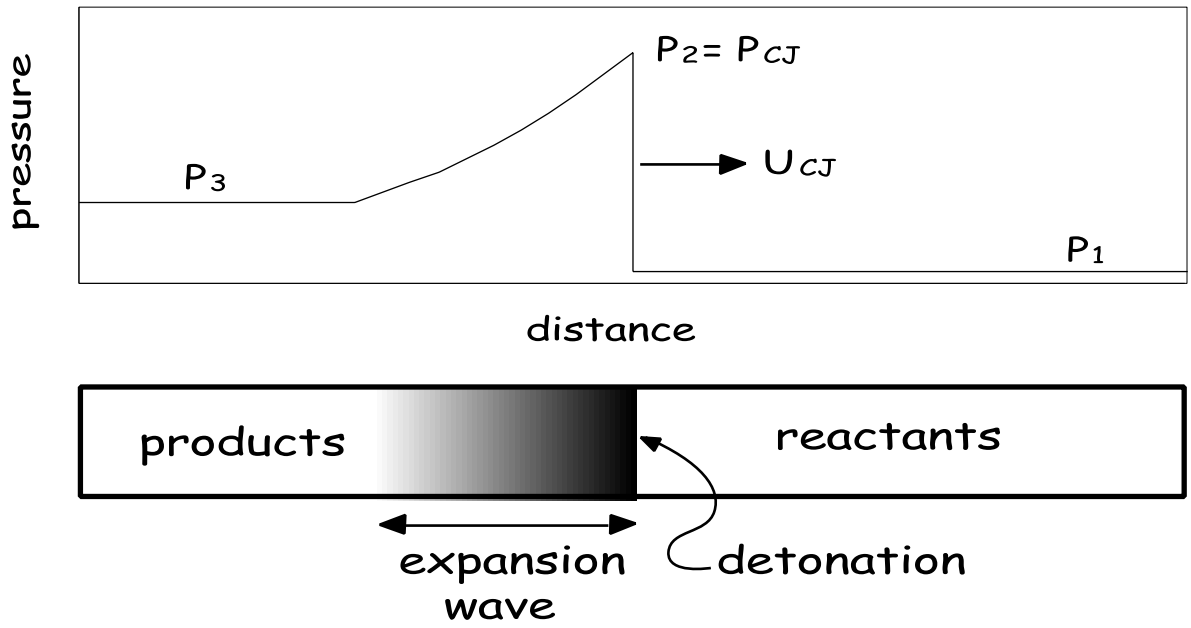

Figure 46: Detonation propagation in tube with a closed end.

In this model, the detonation travels down the tube at a constant speed U, equal to the Chapman-Jouguet velocity U_{CJ}. The corresponding peak pressure, p_2, is the Chapman-Jouguet pressure p_{CJ}. The structure of the reaction zone and the associated property variations such as the Von Nuemann presssure spike are neglected in this model.

B Chapman-Jouguet State

The Chapman-Jouguet state can be determined analytically by using an ideal gas equation of state and assuming constant heat capacity to solve the jump conditions that treat

the detonation as a discontinuity. The equations are most conveniently solved in a coordinate system that moves with the detonation wave speed U. The velocity components are

$$w_1 = U - u_1 \tag{52}$$

$$w_2 = U - u_2 \tag{53}$$

and the jump conditions are simply the conservation of mass, momentum and energy in this frame

$$\begin{aligned} \rho_1 w_1 &= \rho_2 w_2 && (54)\\ P_1 + \rho_1 w_1^2 &= P_2 + \rho_2 w_2^2 && (55)\\ h_1 + \frac{w_1^2}{2} &= h_2 + \frac{w_2^2}{2} && (56)\\ s_2 &\geq s_1 && (57) \end{aligned}$$

A widely used version of this model uses different properties in the reactants and products (see Thompson, Compressible Fluid Dynamics, pp. 347-359) and assumes a value of the energy release q, different values of γ and R in reactants and products. These parameters can be determined by equilibrium computations based on realistic thermochemical properties and a mixture of the relevant gas species in reactants and products. Examples of the results of these computations are given in Shepherd and Schultz.

$$\begin{aligned} h_1 &= c_{p1} T && (58)\\ h_2 &= c_{p2} T - q && (59)\\ P_1 &= \rho_1 R_1 T_1 && (60)\\ P_2 &= \rho_2 R_2 T_2 && (61)\\ c_{p1} &= \frac{\gamma_1 R_1}{\gamma_1 - 1} && (62)\\ c_{p2} &= \frac{\gamma_2 R_2}{\gamma_2 - 1} && (63)\\ & && (64) \end{aligned}$$

Substitute into the jump conditions to yield:

$$\frac{P_2}{P_1} = \frac{1 + \gamma_1 M_1^2}{1 + \gamma_2 M_2^2} \tag{65}$$

$$\frac{v_2}{v_1} = \frac{\gamma_2 M_2^2}{\gamma_1 M_1^2} \frac{1 + \gamma_1 M_1^2}{1 + \gamma_2 M_2^2} \tag{66}$$

$$\frac{T_2}{T_1} = \frac{\gamma_1 R_1}{\gamma_2 R_2} \frac{\dfrac{1}{\gamma_1 - 1} + \dfrac{1}{2} M_1^2 + \dfrac{q}{c_1^2}}{\dfrac{1}{\gamma_2 - 1} + \dfrac{1}{2} M_2^2} \tag{67}$$

Chapman-Jouguet Conditions Isentrope, Hugoniot and Rayleigh lines are all tangent at the CJ point

$$\frac{P_{CJ} - P_1}{v_{CJ} - V_1} = \frac{\partial P}{\partial v}\bigg)_{Hugoniot} = \frac{\partial P}{\partial v}\bigg)_{s} \tag{68}$$

which implies that the product velocity is *sonic relative to the wave*

$$w_{2,CJ} = c_2 \qquad \text{or} \qquad M_2 = 1 \tag{69}$$

Subsituting the CJ condition into the analytic solution for the detonation jump conditions yields an expression for the CJ velocity or Mach number.

$$M_{CJ} = \sqrt{\mathcal{H} + \frac{(\gamma_1 + \gamma_2)(\gamma_2 - 1)}{2\gamma_1(\gamma_1 - 1)}} + \sqrt{\mathcal{H} + \frac{(\gamma_2 - \gamma_1)(\gamma_2 + 1)}{2\gamma_1(\gamma_1 - 1)}} \tag{70}$$

where the parameter $\mathcal{H}$ is the nondimensional energy release

$$\mathcal{H} = \frac{(\gamma_2 - 1)(\gamma_2 + 1)q}{2\gamma_1 R_1 T_1} \tag{71}$$

The other properties can be found by substitution into the general solutions given above

$$\frac{P_{CJ}}{P_1} = \frac{\gamma_1 M_{CJ}^2 + 1}{\gamma_2 + 1}; \tag{72}$$

$$\frac{\rho_{CJ}}{\rho_1} = \frac{\gamma_1(\gamma_2 + 1)M_{CJ}^2}{\gamma_2(1 + \gamma_1 M_{CJ}^2)}; \tag{73}$$

$$\frac{T_{CJ}}{T_1} = \frac{P_{CJ}}{P_1}\frac{R_1\rho_1}{R_2\rho_{CJ}}; \tag{74}$$

$$u_{CJ} = U_{CJ}\left(1 - \frac{\rho_1}{\rho_2}\right) \tag{75}$$

One-γ Model

If we further simplify the model and use only a single value of γ and R common to reactants and products, then the properties at the CJ state are

$$M_{CJ} = \sqrt{\mathcal{H} + 1} + \sqrt{\mathcal{H}} \tag{76}$$

where

$$\mathcal{H} = \frac{(\gamma^2 - 1)q}{2\gamma R T_1} \tag{77}$$

and

$$\frac{P_{CJ}}{P_1} = \frac{\gamma M_{CJ}^2 + 1}{\gamma + 1}; \tag{78}$$

$$\frac{\rho_{CJ}}{\rho_1} = \frac{(\gamma+1)M_{CJ}^2}{(1+\gamma M_{CJ}^2)}; \tag{79}$$

$$\frac{T_{CJ}}{T_1} = \frac{P_{CJ}}{P_1}\frac{\rho_1}{\rho_{CJ}}. \tag{80}$$

A further approximation is to assume that the detonation Mach number is much larger than unity, in which case we have the "strong detonation" approximate solution:

$$U_{CJ} \approx \sqrt{2(\gamma_2^2-1)q} \tag{81}$$

$$\rho_{CJ} \approx \frac{\gamma_2+1}{\gamma_2}\rho_1 \tag{82}$$

$$P_{CJ} \approx \frac{1}{\gamma_2+1}\rho_1 U_{CJ}^2 \tag{83}$$

$$T_{CJ} \approx \frac{2\gamma(\gamma-1)}{\gamma+1}\frac{q}{R} \tag{84}$$

$$u_{CJ} \approx \frac{U_{CJ}}{\gamma+1} \tag{85}$$

$$\tag{86}$$

C Taylor-Zeldovich Expansion Wave

The properties within the expansion wave can be calculated by assuming a similarity solution. For a planar flow, the simplest method of finding explicit solutions is with the method of characteristics (Taylor (1950), Zeldovich (1940)). There are two sets of characteristics, C^+ and C^- defined by

$$C^+ \qquad \frac{dx}{dt} = u + c \tag{87}$$

$$C^- \qquad \frac{dx}{dt} = u - c \tag{88}$$

$$\tag{89}$$

On the characteristics C^+

$$\frac{dx}{dt} = u + x = \frac{x}{t} \qquad \text{for} \qquad c_0 < \frac{x}{t} < v_{CJ} \tag{90}$$

$$\frac{dx}{dt} = c_0 \qquad \text{for} \qquad 0 < \frac{x}{t} < c_0 \quad .$$

The characteristics C^- span the region between the detonation and the stationary gas

$$J_- = u - \frac{2}{\gamma-1}c = -\frac{2}{\gamma-1}c_0 = u_2 - \frac{2}{\gamma-1}c_2 \quad . \tag{91}$$

The CJ condition is

$$u_2 = U_{CJ} - c_{CJ} \quad . \tag{92}$$

This gives

$$c_0 = \frac{\gamma+1}{2} c_{CJ} - \frac{\gamma-1}{2} U_{CJ} \quad . \tag{93}$$

The values of γ and the isentropic sound speed c_{CJ} are determined with the STANJAN program (Reynolds (1986)) and depend on, for instance, the chemical composition of the mixture and the partial pressures. In the expansion wave

$$\begin{aligned} u + c &= \frac{x}{t} \\ u - \frac{2}{\gamma-1} c &= -\frac{2}{\gamma-1} c_0 \\ c\left(1 + \frac{2}{\gamma-1}\right) &= \frac{x}{t} + \frac{2}{\gamma-1} c_0 \\ \frac{c}{c_0}\left(\frac{\gamma+1}{\gamma-1}\right) &= \frac{2}{\gamma-1} + \frac{x}{c_0 t} \quad . \end{aligned} \tag{94}$$

This finally gives

$$\frac{c}{c_0} = \frac{2}{\gamma+1} + \frac{\gamma-1}{\gamma+1}\frac{x}{c_0 t} = \; 1 - \frac{\gamma-1}{\gamma+1}\left(1 - \frac{x}{c_o t}\right) \tag{95}$$

The other properties are found from the following isentropic relations

$$\frac{c}{c_0} = \left(\frac{T}{T_0}\right)^{\frac{1}{2}} \quad ; \quad \frac{p}{p_0} = \left(\frac{\rho}{\rho_0}\right)^{\gamma} \quad ; \quad \frac{T}{T_0} = \left(\frac{\rho}{\rho_0}\right)^{\gamma} \quad . \tag{96}$$

The Chapman-Jouguet model of an ideal detonation can be combined with the Taylor-Zeldovich similarity solution to obtain an analytic solution to the flow field behind a steadily-propagating detonation in a tube. This solution can be constructed piecewise by considering the three regions shown on Figure 46: the stationary reactants ahead of the detonation mixture; the expansion wave behind the detonation; and the stationary products next to the closed end of the tube. In this model, the detonation travels down the tube at a constant speed v, equal to the Chapman-Jouguet velocity U_{CJ}. The corresponding peak pressure, p_2, is the Chapman-Jouguet pressure p_{CJ}. The Von Neumann presssure spike is neglected in this model.

The sound speed distribution within the expansion wave can be calculated with the method of characteristics.

$$\frac{c}{c_3} = \frac{2}{\gamma+1} + \frac{\gamma-1}{\gamma+1}\frac{x}{c_3 t} = \; 1 - \frac{\gamma-1}{\gamma+1}\left(1 - \frac{x}{c_3 t}\right) \quad , \tag{97}$$

where c_3 is calculated from

$$c_3 = \frac{\gamma+1}{2} c_{CJ} - \frac{\gamma-1}{2} U_{CJ} \quad . \tag{98}$$

Expression (97) is valid in the expansion wave, *i.e.* for $c_3 t \leq x \leq U_{CJ} t$. The values of the ratio of specific heats, γ, and the isentropic sound speed, c_{CJ}, are determined with the STANJAN program and depend on, for instance, the chemical composition of the mixture and the partial pressures. The other properties are found from the following isentropic relations

$$\frac{c}{c_3} = \left(\frac{T}{T_3}\right)^{\frac{1}{2}} \quad ; \quad \frac{p}{p_3} = \left(\frac{\rho}{\rho_3}\right)^{\gamma} \quad ; \quad \frac{T}{T_3} = \left(\frac{\rho}{\rho_3}\right)^{\gamma-1} \tag{99}$$

where T is the temperature, ρ is the density and p is the pressure. The subscript $_3$ refers to the conditions at the end of the expansion wave. The pressure p_3 is calculated from

$$p_3 = p_{CJ} \left(\frac{c_3}{c_{CJ}}\right)^{\frac{2\gamma}{\gamma-1}} \quad . \tag{100}$$

This finally gives for the pressure in the expansion wave

$$p = p_3 \left(1 - \left(\frac{\gamma-1}{\gamma+1}\right)\left[1 - \frac{x}{c_3 t}\right]\right)^{\frac{2\gamma}{\gamma-1}} \quad . \tag{101}$$

D Tables of experimental conditions and results.

Three different tubes were used in this study. Dimensions are given in Table D.1. A variety of internal obstacles were investigated. These are described in Table D.1. All obstacles begin at the thrust wall and extend downstream the length indicated below.

Wave classification is based on pressure histories and wave speeds. 'Det.' indicates a detonation was initiated in the first half of the tube. All other cases that transitioned to detonation are labeled 'DDT'. A 'fast flame' pressure history shows shocks as well as the pressure rise due to a flame, with wave speeds typically on the order of 500-1000 m/s.

Various exit geometries were studied. Two converging-diverging nozzles, with nominal (steady flow) exit Mach numbers of 3 and 5, are denoted M3(nom.) and M5(nom.) respectively. Both nozzles had a 15mm throat and a 10^o half angle. A 'straight' exit configuration indicates no area change at the diaphragm with the tube length as given in Table D.1. 'Extension' indicates a 76 mm diameter, 0.609 m long constant area extension was mounted to the downstream end of the tube. 'Nozzle' is an 8^o half-angle, 0.3 m long diverging cone mounted to the downstream end of the tube. The effect of an essentially infinite downstream flange thickness was investigated in the 'flat plate' series This series was aimed at determining the contribution, if any, to the impulse of the blast wave pushing back on the downstream flange.

In some cases a driver was used to initiate less sensitive mixtures. The volume of the driver used is shown as a percentage of the total tube volume. Unless otherwise indicated, the driver volume was measured at the temperature T_1.

D.1 Table Notes

[a] This spiral geometry was modified to include a couple of cross bars which obstruct the core flow. The actual blockage ratio will be slightly higher than shown here.
[b] Data lost.
[c] DDT was observed due to the extension.
[d] A decaying blast wave was observed due to the driver.
[e] Measured at 297 K.

Table 7: Tube configurations

Tube	Diameter (mm)	Length (m)	L/d
1	38	1.5	40
2	76	0.609	8
3	76	1.016	13

Table 8: Obstacle configurations.

Obstacle	Geometry	Blockage ratio	Pitch (mm)	Length (m)
A	Spiral	0.38 [a]	11	0.305
B	Spiral	0.43	28	0.609
C	Spiral	0.43	51	0.609
D	Blockage plates	0.43	78	1.016
E	Orifice plates	0.43	78	1.016
F	Orifice plates	0.43	78	0.468

Table 9: Direct impulse measurements: H_2 (T_1=297K)

Shot no.	Mixture	P_1 (kPa)	Wave type	I_V (kg/m^{2}s)	I_{SP} (s)	Tube config	Obstacles	Exit config.
105	$2H_2$+O_2	100	det.	922	191	3	none	straight
106	$2H_2$+O_2	100	det.	707	146	3	F	straight
107	$2H_2$+O_2	100	det.	986	204	3	F	extension

Table 10: Direct impulse measurements: C_2H_2 (T_1=297K)

Shot no.	Mixture	P_1 (kPa)	Wave type	I_V (kg/m^{2}s)	I_{SP} (s)	Tube config	Obstacles	Exit config.
35	C_2H_2+2.5O_2	100	det.	2465	202	2	none	straight

Table 11: Direct impulse measurements: C_2H_4 (T_1=297K)

Shot no.	Mixture	P_1 (kPa)	Wave type	I_V (kg/m^{2}s)	I_{SP} (s)	Tube config.	Obstacles	Exit config.
6	C_2H_4+3O_2	98.8	det.	1665	133	1	A	straight
7	C_2H_4+3O_2	79	det.	1230	123	1	A	straight
8	C_2H_4+3O_2	50	det.	662	106	1	A	straight
9	C_2H_4+3O_2	100	det.	1646	132	1	A	straight
13	C_2H_4+3O_2+7.5N_2	100	fast flame	643	55	1	A	straight
14	2.2C_2H_4+3O_2	100	det.	1797	147	1	A	straight
10	C_2H_4+3O_2	50	det.	346	55	1	A	M3(nom.)
11	C_2H_4+3O_2	79	det.	729	73	1	A	M3(nom.)
12	C_2H_4+3O_2	100	det.	1056	85	1	A	M3(nom.)
19	C_2H_4+3O_2	50	det.	229	37	1	A	M5(nom.)
21	C_2H_4+3O_2	79	det.	499	50	1	A	M5(nom.)
20	C_2H_4+3O_2	100	det.	769	62	1	A	M5(nom.)
39	C_2H_4+3O_2	30	DDT	466	124	3	none	straight
37	C_2H_4+3O_2	50	det.	882	141	3	none	straight
38	C_2H_4+3O_2	50	det.	882	141	3	none	straight
53	C_2H_4+3O_2	50	det.	882	141	3	none	straight
40	C_2H_4+3O_2	80	det.	1606	161	3	none	straight
41	C_2H_4+3O_2	100	det.	2136	171	3	none	straight
42	C_2H_4+3O_2+N_2	100	det.	1951	159	3	none	straight
44	C_2H_4+3O_2+1.71N_2	100	DDT	1797	148	3	none	straight
43	C_2H_4+3O_2+2.67N_2	100	fast flame	699	58	3	none	straight
54	C_2H_4+3O_2+2.67N_2	100	fast flame	758	63	3	none	straight
45	C_2H_4+3O_2+2.67N_2	100	det.	1402	117	3	D	straight
46	C_2H_4+3O_2+6N_2	100	DDT	1153	98	3	D	straight
47	C_2H_4+3O_2+11.27N_2	100	fast flame	832	72	3	D	straight
48	C_2H_4+3O_2+N_2	100	det.	1603	131	3	D	straight
49	C_2H_4+3O_2	100	det.	1764	141	3	D	straight
50	C_2H_4+3O_2	30	det.	264	70	3	D	straight
51	C_2H_4+3O_2	50	det.	648	104	3	D	straight
52	C_2H_4+3O_2	80	det.	1274	128	3	D	straight
55	C_2H_4+3O_2+11.27N_2	100	- [b]	854	74	3	E	straight
56	C_2H_4+3O_2+6N_2	100	DDT	1155	98	3	E	straight

Table 12: Direct impulse measurements: C_2H_4 (T_1=297K)

Shot no.	Mixture	P_1 (kPa)	Wave type	I_V (kg/m^{2}s)	I_{SP} (s)	Tube config.	Obstacles	Exit config.
57	C_2H_4+3O_2+2.67N_2	100	det.	1407	117	3	E	straight
58	C_2H_4+3O_2+N_2	100	det.	1609	131	3	E	straight
59	C_2H_4+3O_2	30	det.	268	71	3	E	straight
60	C_2H_4+3O_2	50	det.	669	107	3	E	straight
61	C_2H_4+3O_2	80	det.	1298	130	3	E	straight
62	C_2H_4+3O_2	100	det.	1769	142	3	E	straight
63	C_2H_4+3O_2+11.27N_2	100	- [b]	829	71	3	E	straight
64	C_2H_4+3O_2+11.27N_2	100	- [b]	630	54	3	F	straight
65	C_2H_4+3O_2+6N_2	100	DDT	1319	112	3	F	straight
66	C_2H_4+3O_2+2.67N_2	100	det.	1562	130	3	F	straight
67	C_2H_4+3O_2+N_2	100	det.	1757	144	3	F	straight
68	C_2H_4+3O_2	30	det.	331	88	3	F	straight
69	C_2H_4+3O_2	50	det.	744	119	3	F	straight
70	C_2H_4+3O_2	80	det.	1408	141	3	F	straight
71	C_2H_4+3O_2	100	det.	1920	154	3	F	straight
73	C_2H_4+3O_2	100	det.	2232	179	3	none	flat plate
80	C_2H_4+3O_2	100	det.	2240	179	3	none	flat plate
74	C_2H_4+3O_2+N_2	100	det.	2013	164	3	none	flat plate
79	C_2H_4+3O_2+N_2	100	det.	2021	165	3	none	flat plate
75	C_2H_4+3O_2+1.71N_2	100	DDT	1853	153	3	none	flat plate
81	C_2H_4+3O_2+1.71N_2	100	DDT	1887	156	3	none	flat plate
78	C_2H_4+3O_2+1.71N_2	100	DDT	1921	158	3	none	flat plate
76	C_2H_4+3O_2+2.67N_2	100	flame	625	52	3	none	flat plate
77	C_2H_4+3O_2+2.67N_2	100	flame	725	60	3	none	flat plate
89	C_2H_4+3O_2	100	det.	2525	202	3	none	extension
87	C_2H_4+3O_2+N_2	100	det.	2382	195	3	none	extension
88	C_2H_4+3O_2+N_2	100	det.	2367	193	3	none	extension
85	C_2H_4+3O_2+1.71N_2	100	DDT	2367	195	3	none	extension
86	C_2H_4+3O_2+1.71N_2	100	DDT	2367	195	3	none	extension
82	C_2H_4+3O_2+2.67N_2	100	DDT[c]	2612	218	3	none	extension
84	C_2H_4+3O_2+2.67N_2	100	DDT[c]	2196	183	3	none	extension

Table 13: Direct impulse measurements: C_2H_4 (T_1=297K)

Shot no.	Mixture	P_1 (kPa)	Wave type	I_V (kg/m^{2}s)	I_{SP} (s)	Tube config.	Obstacles	Exit config.
83	C_2H_4+3O_2+2.67N_2	100	fast flame[c]	2224	185	3	none	extension
96	C_2H_4+3O_2	100	det	2175	174	3	F	extension
97	C_2H_4+3O_2	100	det.	2160	173	3	F	extension
94	C_2H_4+3O_2+N_2	100	det.	1959	160	3	F	extension
95	C_2H_4+3O_2+N_2	100	det.	1990	163	3	F	extension
92	C_2H_4+3O_2+1.71N_2	100	det.	1912	158	3	F	extension
93	C_2H_4+3O_2+1.71N_2	100	det.	1881	155	3	F	extension
90	C_2H_4+3O_2+2.67N_2	100	det.	1773	148	3	F	extension
91	C_2H_4+3O_2+2.67N_2	100	det.	1773	148	3	F	extension
102	C_2H_4+3O_2	100	det.	1964	157	3	F	8^o nozzle
101	C_2H_4+3O_2+N_2	100	det.	1772	145	3	F	8^o nozzle
100	C_2H_4+3O_2+1.71N_2	100	det.	1677	138	3	F	8^o nozzle
99	C_2H_4+3O_2+2.67N_2	100	det.	1572	131	3	F	8^o nozzle

Table 14: Direct impulse measurements: C_3H_8

Shot no.	Mixture	P_1 (kPa)	T_1 (K)	Wave type	I_V (kg/m^{2}s)	I_{SP} (s)	Initiator config.	Tube	Obstacles	Exit config.
15	C_3H_8+5O_2	50	297	det.	719	105	spark	1	A	straight
16	C_3H_8+5O_2	79	297	det.	1324	121	spark	1	A	straight
17	C_3H_8+5O_2	100	297	det.	1807	132	spark	1	A	straight
18	1.9C_3H_8+5O_2	100	297	det.	2043	144	spark	1	A	straight
23	C_3H_8+5O_2	50	297	det.	771	113	spark	2	B	straight
26	C_3H_8+5O_2	100	297	det.	2045	149	spark	2	B	straight
27	C_3H_8+5O_2+7.5N_2	100	297	DDT	1388	112	spark	2	B	straight
28	C_3H_8+5O_2+11.25N_2	100	297	DDT	1195	99	spark	2	B	straight
29	C_3H_8+5O_2+15N_2	100	297	fast flame	835	70	spark	2	B	straight
24	C_3H_8+5O_2+18.8N_2	100	297	flame	630	53	spark	2	B	straight
25	C_3H_8+5O_2+18.8N_2	100	297	flame	642	54	spark	2	B	straight
30	C_3H_8+5O_2	100	297	det.	2355	172	spark	2	C	straight
31	C_3H_8+5O_2+7.5N_2	100	297	DDT	1577	128	spark	2	C	straight
32	C_3H_8+5O_2+11.25N_2	100	297	DDT	1430	118	spark	2	C	straight
33	C_3H_8+5O_2+15N_2	100	297	fast flame	909	76	spark	2	C	straight
34	C_3H_8+5O_2+18.8N_2	100	297	- [b]	508	43	spark	2	C	straight
35	C_3H_8+5O_2+18.8N_2	100	297	flame	628	53	spark	2	C	straight
113	C_3H_8+5O_2+18.8N_2	100	297	decaying blast[d]	91	8	C_3H_8-O_2,2.2%	3	none	straight
114	C_3H_8+5O_2+9N_2	100	297	decaying blast [d]	91	7	C_3H_8-O_2,2.2%	3	none	straight
115	C_3H_8+5O_2+4N_2	100	297	decaying blast [d]	273	21	C_3H_8-O_2,2.2%	3	none	straight
116	C_3H_8+5O_2+1.5N_2	100	297	det.	1419	107	C_3H_8-O_2,2.2%	3	none	straight
117	C_3H_8+5O_2+4N_2	100	297	decaying blast [d]	109	9	C_3H_8-O_2,2.2%	3	none	straight
118	C_3H_8+5O_2	100	297	det.	1201	126	C_3H_8-O_2,2.2%	3	none	straight
119	C_3H_8+5O_2+18.8N_2	100	297	decaying blast [d]	109	9	C_3H_8-O_2,2.2%	3	none	straight
120	C_3H_8+5O_2+18.8N_2	100	297	det.	1201	100	C_3H_8-O_2,6%	3	none	straight
127	C_3H_8+5O_2+18.8N_2	100	323	decaying blast [d]	276	26	C_3H_8-O_2,3.7%	3	none	straight
124	C_3H_8+5O_2	100	297	det.	1781	130	C_3H_8-O_2,2.2%	3	none	straight

Table 15: Direct impulse measurements: JP-10

Shot no.	Mixture	T_1 (K)	P_1 (kPa)	Wave type	I_V (kg/m^{2}s)	I_{SP} (s)	Initiator	Tube config	Obstacles	Exit config
125	$C_{10}H_{16}$+14O_2+52.6N_2	323	100	decaying blast [d]	61	6	C_3H_8-O_2,2.2%[e]	3	none	straight
126	$C_{10}H_{16}$+14O_2+52.6N_2	323	100	decaying blast [d]	246	22	C_3H_8-O_2,3.7%	3	none	straight
136	$C_{10}H_{16}$+14O_2+14N_2	323	100	det.	1259	112	C_2H_2-O_2,11%	3	none	straight
139	$C_{10}H_{16}$+14O_2+28N_2	323	100	det.	136	106	C_2H_2-O_2,11%	3	none	straight
138	$C_{10}H_{16}$+14O_2+52.6N_2	323	100	decaying blast [d]	491	45	C_2H_2-O_2,11%	3	none	straight

E Tables of impulse model predictions.

Impulse model predicted values are given for fuels including C_2H_4, C_3H_8, C_2H_2, H_2, Jet A and JP10 with oxygen and air for different initial pressures, equivalence ratios and diluent amounts. The different parameters varied in the tables are listed below:

P_1	initial pressure
T_1	initial temperature
U_{CJ}	Chapman-Jouguet detonation velocity
P_2	Chapman-Jouguet pressure
c_2	sound speed in the burnt gases just behind the detonation wave
γ	specific heat ratio of products
u_2	flow velocity just behind the detonation wave
c_3	sound speed in the burnt gases at rest behind the Taylor expansion wave
P_3	pressure behind the Taylor expansion wave
α	non-dimensional time of the first reflected characteristic at the open end
I_V	impulse of the single-cycle pulse detonation engine per unit volume
V	specific volume of the initial mixture
I_{SP}	specific impulse relative to mixture mass
X_F	fuel mass fraction in the initial mixture
I_{SPF}	specific impulse relative to fuel mass

The calculations were carried out assuming the values for the following parameters:

$\beta = 0.53$ - characteristic non-dimensional time of the expansion in the non-simple region

$P_0 = 1.01325$ bar - ambient pressure outside the tube

Table 16: Impulse model predictions for C_2H_4-O_2 mixtures

P_1 (bar)	T_1 (K)	Mixture	U_{CJ} (m/s)	P_2 (bar)	c_2 (m/s)	γ	u_2 (m/s)	c_3(m/s)	P_3 (bar)	α	I_V(kg/m^{2}s)	V(m^3/kg)	I_{SP} (s)	X_F	I_{SPF} (s)
0.2	300	C2H4+3O2	2298.1	6.26	1237.3	1.2342	1060.8	1113.1	2.05	1.120	199.3	4.02	81.7	0.22615	361.1
0.4	300	C2H4+3O2	2331.3	12.86	1256.8	1.2349	1074.5	1130.6	4.23	1.120	606.8	2.01	124.3	0.22615	549.7
0.6	300	C2H4+3O2	2350.9	19.59	1268.4	1.2352	1082.5	1141.1	6.45	1.119	1017.1	1.34	138.9	0.22615	614.3
0.8	300	C2H4+3O2	2364.9	26.4	1276.8	1.2354	1088.1	1148.7	8.71	1.119	1429.4	1.005	146.4	0.22615	647.5
1	300	C2H4+3O2	2375.8	33.27	1283.5	1.2356	1092.3	1154.8	10.99	1.119	1843.5	0.804	151.1	0.22615	668.1
1.2	300	C2H4+3O2	2384.7	40.2	1288.7	1.2357	1096	1159.5	13.28	1.119	2258.9	0.67	154.3	0.22615	682.2
1.4	300	C2H4+3O2	2392.2	47.2	1292.8	1.2359	1099.4	1163.1	15.59	1.119	2676.0	0.574	156.6	0.22615	692.4
1.6	300	C2H4+3O2	2398.8	54.2	1296.5	1.2359	1102.3	1166.5	17.91	1.118	3092.4	0.503	158.6	0.22615	701.1
1.8	300	C2H4+3O2	2404.5	61.25	1299.9	1.236	1104.6	1169.6	20.25	1.118	3511.4	0.447	160.0	0.22615	707.5
2	300	C2H4+3O2	2409.6	68.32	1303	1.2361	1106.6	1172.4	22.60	1.118	3931.0	0.402	161.1	0.22615	712.3
1	300	0.2C2H4+3O2	1719	17.85	948.9	1.1726	770.1	882.4	6.66	1.108	1375.5	0.785	110.1	0.05522	1993.3
1	300	0.4C2H4+3O2	1974	23.55	1070.4	1.1792	903.6	989.4	8.36	1.116	1595.4	0.791	128.6	0.10466	1229.1
1	300	0.6C2H4+3O2	2137.6	27.38	1155.5	1.2054	982.1	1054.6	9.37	1.118	1697.2	0.796	137.7	0.14919	923.1
1	300	0.8C2H4+3O2	2267.5	30.55	1224.7	1.2244	1042.8	1107.7	10.21	1.119	1774.8	0.8	144.7	0.18949	763.8
1	300	1C2H4+3O2	2375.8	33.27	1283.5	1.2356	1092.3	1154.8	10.99	1.119	1843.5	0.804	151.1	0.22615	668.1
1	300	1.2C2H4+3O2	2467	35.62	1333.2	1.2393	1133.8	1197.5	11.72	1.119	1908.2	0.808	157.2	0.25964	605.3
1	300	1.4C2H4+3O2	2542.9	37.61	1374.9	1.2361	1168	1237.0	12.44	1.118	1971.5	0.811	163.0	0.29035	561.4
1	300	1.6C2H4+3O2	2604	39.17	1410.2	1.2278	1193.8	1274.2	13.13	1.117	2032.0	0.814	168.6	0.31861	529.2
1	300	1.8C2H4+3O2	2650.3	40.3	1438.4	1.2184	1211.9	1306.1	13.73	1.116	2082.5	0.817	173.4	0.34471	503.1
1	300	2C2H4+3O2	2681.8	40.98	1459.6	1.2118	1222.2	1330.2	14.16	1.115	2116.3	0.82	176.9	0.36888	479.5
1	300	2.2C2H4+3O2	2699.3	41.2	1474.5	1.2094	1224.8	1346.3	14.40	1.113	2130.5	0.822	178.5	0.39133	456.2
1	300	2.4C2H4+3O2	2704.2	41.03	1483.5	1.2112	1220.7	1354.6	14.46	1.111	2127.4	0.825	178.9	0.41224	434.0
1	300	2.6C2H4+3O2	2698.5	40.54	1487.1	1.216	1211.4	1356.3	14.37	1.110	2110.3	0.827	177.9	0.43176	412.0
1	300	C2H4+3O2	2375.8	33.27	1283.5	1.2356	1092.3	1154.8	10.99	1.119	1843.5	0.804	151.1	0.22615	668.1
1	300	C2H4+3O2+0.44N2	2316.2	31.38	1251.2	1.2217	1065	1133.1	10.53	1.118	1794.7	0.812	148.6	0.20554	722.7
1	300	C2H4+3O2+N2	2258.3	29.57	1220.7	1.2099	1037.6	1111.8	10.07	1.118	1743.4	0.82	145.7	0.18449	789.9
1	300	C2H4+3O2+1.71N2	2197.8	27.77	1189.3	1.1985	1008.5	1089.2	9.61	1.117	1690.4	0.828	142.7	0.16315	874.5
1	300	C2H4+3O2+2.67N2	2131.9	25.89	1155.3	1.1873	976.6	1063.8	9.10	1.116	1630.8	0.837	139.1	0.14108	986.2
1	300	C2H4+3O2+4N2	2059.9	23.94	1118.7	1.1773	941.2	1035.3	8.55	1.115	1564.0	0.845	134.7	0.11882	1133.8
1	300	C2H4+3O2+6N2	1976.8	21.82	1077.4	1.1694	899.4	1001.2	7.93	1.114	1484.9	0.854	129.3	0.09603	1346.0
1	300	C2H4+3O2+9.33N2	1873.8	19.37	1028.3	1.1682	845.5	957.2	7.16	1.111	1381.3	0.863	121.5	0.07279	1669.4
1	300	C2H4+3O2+11.28N2	1824.6	18.25	1005.8	1.1717	818.8	935.5	6.79	1.109	1328.3	0.866	117.3	0.06375	1839.3
1	300	C2H4+3O2+16N2	1722.7	16.04	961.8	1.1898	760.9	889.6	6.03	1.104	1212.3	0.872	107.8	0.04902	2198.2
1	300	C2H4+3O2+36N2	1404.2	10.27	823	1.2782	581.2	742.2	3.97	1.086	854.6	0.881	76.8	0.02477	3098.4

Table 17: Impulse model predictions for C_3H_8-O_2 mixtures

P_1 (bar)	T_1 (K)	Mixture	U_{CJ} (m/s)	P_2 (bar)	c_2 (m/s)	γ	u_2 (m/s)	c_3(m/s)	P_3 (bar)	α	I_V(kg/m^{2}s)	V(m^3/kg)	I_{SP} (s)	X_F	I_{SPF} (s)
0.2	300	C3H8+5O2	2287.1	6.81	1227.9	1.2196	1059.2	1111.6	2.25	1.121	238.7	3.66	89.1	0.21607	412.2
0.4	300	C3H8+5O2	2318.2	13.96	1246.3	1.2198	1071.9	1128.5	4.64	1.121	686.4	1.83	128.3	0.21607	593.6
0.6	300	C3H8+5O2	2336.5	21.24	1257	1.22	1079.5	1138.3	7.07	1.120	1136.6	1.22	141.6	0.21607	655.3
0.8	300	C3H8+5O2	2349.5	28.61	1264.7	1.22	1084.8	1145.4	9.53	1.120	1589.7	0.92	148.6	0.21607	687.7
1	300	C3H8+5O2	2359.6	36.04	1270.7	1.2201	1088.9	1150.9	12.02	1.120	2044.1	0.73	152.7	0.21607	706.9
1.2	300	C3H8+5O2	2367.9	43.53	1275.6	1.2201	1092.3	1155.4	14.53	1.120	2500.5	0.61	155.7	0.21607	720.8
1.4	300	C3H8+5O2	2374.9	51.05	1279.8	1.2201	1095.1	1159.3	17.05	1.120	2957.6	0.52	158.0	0.21607	731.2
1.6	300	C3H8+5O2	2380.9	58.61	1283.7	1.22	1097.2	1163.0	19.61	1.119	3417.6	0.46	159.6	0.21607	738.4
1.8	300	C3H8+5O2	2386.3	66.21	1286.9	1.22	1099.4	1166.0	22.16	1.119	3877.4	0.41	160.9	0.21607	744.5
2	300	C3H8+5O2	2391.1	73.84	1289.7	1.2201	1101.4	1168.5	24.72	1.119	4337.5	0.37	162.3	0.21607	751.0
1	300	0.2C3H8+5O2	1692.1	17.62	937.4	1.178	754.7	870.2	6.59	1.107	1377.4	0.77	108.0	0.052243	2066.8
1	300	0.4C3H8+5O2	1956.7	24.13	1060.4	1.1706	896.3	983.9	8.64	1.116	1665.9	0.76	128.7	0.099299	1296.3
1	300	0.6C3H8+5O2	2122.3	28.68	1145.3	1.193	977	1051.0	9.92	1.118	1815.8	0.75	138.6	0.1419	977.0
1	300	0.8C3H8+5O2	2252.4	32.59	1213.6	1.2104	1038.8	1104.3	11.00	1.119	1935.9	0.74	146.2	0.18066	809.4
1	300	1C3H8+5O2	2359.6	36.04	1270.7	1.2201	1088.9	1150.9	12.02	1.120	2044.1	0.73	152.7	0.21607	706.9
1	300	1.2C3H8+5O2	2448.1	39.07	1318.6	1.2211	1129.5	1193.7	13.02	1.120	2149.8	0.73	159.1	0.24854	640.1
1	300	1.4C3H8+5O2	2518.6	41.62	1357.7	1.2138	1160.9	1233.6	14.02	1.119	2254.6	0.72	165.5	0.27843	594.3
1	300	1.6C3H8+5O2	2570.2	43.54	1388.3	1.2025	1181.9	1268.6	14.93	1.118	2348.8	0.71	171.0	0.30603	558.6
1	300	1.8C3H8+5O2	2601.4	44.73	1410.3	1.1947	1191.1	1294.3	15.61	1.116	2417.3	0.71	174.5	0.3316	526.1
1	300	2C3H8+5O2	2611.8	45.13	1423.2	1.1946	1188.6	1307.5	15.94	1.114	2448.8	0.70	175.5	0.35535	493.8
1	300	2.2C3H8+5O2	2602.7	44.77	1427.6	1.2021	1175.1	1308.9	15.93	1.111	2444.4	0.70	174.2	0.37747	461.4
1	300	2.4C3H8+5O2	2575.7	43.75	1423.3	1.2151	1152.4	1299.4	15.63	1.108	2410.5	0.69	170.5	0.39813	428.3
1	300	2.6C3H8+5O2	2531.7	42.11	1411.1	1.2335	1120.6	1280.3	15.06	1.105	2349.4	0.69	165.2	0.41745	395.8
1	300	C3H8+5O2	2359.6	36.04	1270.7	1.2201	1088.9	1150.9	12.02	1.120	2044.1	0.73	152.7	0.21607	706.9
1	300	C3H8+5O2+0.67N2	2305.2	33.84	1241.8	1.2088	1063.4	1130.8	11.44	1.119	1973.6	0.75	150.1	0.19797	758.1
1	300	C3H8+5O2+1.5N2	2251.3	31.73	1213.8	1.1992	1037.5	1110.5	10.87	1.119	1901.3	0.76	147.3	0.17918	822.1
1	300	C3H8+5O2+2.57N2	2194	29.61	1184.4	1.1897	1009.6	1088.6	10.28	1.118	1826.2	0.77	144.1	0.15972	902.1
1	300	C3H8+5O2+4N2	2131.4	27.45	1152.4	1.1806	979	1064.0	9.67	1.117	1746.0	0.79	140.4	0.13948	1006.8
1	300	C3H8+5O2+6N2	2061.4	25.2	1117.3	1.1724	944.1	1035.9	9.01	1.116	1658.4	0.80	135.9	0.11849	1147.1
1	300	C3H8+5O2+9N2	1979.9	22.79	1077.3	1.1661	902.6	1002.3	8.28	1.114	1558.7	0.82	130.3	0.096659	1347.9
1	300	C3H8+5O2+14N2	1878	20.06	1029.2	1.1663	848.8	958.6	7.41	1.111	1434.8	0.84	122.3	0.073954	1653.4
1	300	C3H8+5O2+18.8N2	1800.6	18.15	994.4	1.174	806.2	924.3	6.76	1.108	1338.5	0.85	115.4	0.060345	1912.9
1	300	C3H8+5O2+24N2	1728.2	16.48	963.7	1.1886	764.5	891.6	6.18	1.104	1247.1	0.85	108.6	0.050315	2157.7
1	300	C3H8+5O2+54N2	1413.7	10.52	827	1.2757	586.7	746.1	4.06	1.086	875.2	0.87	77.8	0.025685	3028.9

Table 18: Impulse model predictions for C_2H_2-O_2 mixtures

P_1 (bar)	T_1 (K)	Mixture	U_{CJ} (m/s)	P_2 (bar)	c_2 (m/s)	γ	u_2 (m/s)	c_3(m/s)	P_3 (bar)	α	I_V(kg/m^{2}s)	V(m^3/kg)	I_{SP} (s)	X_F	I_{SPF} (s)
0.2	300	C2H2+2.5O2	2335.9	6.29	1263.4	1.2579	1072.5	1125.1	2.03	1.119	192.5	4.116	80.8	0.24556	328.9
0.4	300	C2H2+2.5O2	2373.5	12.94	1285.9	1.2605	1087.6	1144.2	4.18	1.118	589.8	2.058	123.7	0.24556	503.9
0.6	300	C2H2+2.5O2	2395.8	19.75	1299	1.2614	1096.8	1155.6	6.39	1.117	990.8	1.372	138.6	0.24556	564.3
0.8	300	C2H2+2.5O2	2411.8	26.65	1308.7	1.2626	1103.1	1163.9	8.63	1.117	1393.2	1.029	146.1	0.24556	595.1
1	300	C2H2+2.5O2	2424.2	33.63	1316.3	1.2633	1107.9	1170.4	10.90	1.117	1798.3	0.823	150.9	0.24556	614.4
1.2	300	C2H2+2.5O2	2434.4	40.66	1322.4	1.2639	1112	1175.7	13.18	1.117	2203.9	0.686	154.1	0.24556	627.6
1.4	300	C2H2+2.5O2	2443.1	47.74	1327.7	1.2644	1115.4	1180.2	15.48	1.116	2611.0	0.588	156.5	0.24556	637.3
1.6	300	C2H2+2.5O2	2450.6	54.87	1332.2	1.2648	1118.4	1184.1	17.80	1.116	3019.5	0.514	158.2	0.24556	644.3
1.8	300	C2H2+2.5O2	2457.3	62.03	1336.2	1.2652	1121.1	1187.5	20.13	1.116	3428.1	0.457	159.7	0.24556	650.4
2	300	C2H2+2.5O2	2463.2	69.23	1339.7	1.2655	1123.5	1190.6	22.47	1.116	3838.3	0.412	161.2	0.24556	656.5
1	300	0.2C2H2+2.5O2	1763.5	18.74	968.6	1.1699	794.9	901.1	6.93	1.110	1411.9	0.790	113.7	0.06112	1860.3
1	300	0.4C2H2+2.5O2	2008.3	24.06	1090	1.198	918.3	999.1	8.39	1.116	1581.9	0.800	129.0	0.11520	1119.8
1	300	0.6C2H2+2.5O2	2173.7	27.75	1178.4	1.2297	995.3	1064.1	9.31	1.117	1665.2	0.808	137.2	0.16338	839.5
1	300	0.8C2H2+2.5O2	2308.5	30.89	1251.8	1.2502	1056.7	1119.6	10.13	1.117	1735.4	0.816	144.4	0.20659	698.8
1	300	1C2H2+2.5O2	2424.2	33.63	1316.3	1.2633	1107.9	1170.4	10.90	1.117	1798.3	0.823	150.9	0.24556	614.4
1	300	1.2C2H2+2.5O2	2525.5	36.08	1373.3	1.2706	1152.2	1217.4	11.64	1.116	1857.3	0.829	157.0	0.28088	558.8
1	300	1.4C2H2+2.5O2	2614.9	38.27	1424.3	1.2736	1190.6	1261.4	12.36	1.116	1913.4	0.835	162.9	0.31304	520.3
1	300	1.6C2H2+2.5O2	2693.8	40.22	1469.9	1.2732	1223.9	1302.7	13.05	1.115	1966.9	0.841	168.6	0.34244	492.4
1	300	1.8C2H2+2.5O2	2763.2	41.93	1511.1	1.2708	1252.1	1341.6	13.72	1.114	2017.3	0.845	173.8	0.36943	470.4
1	300	2C2H2+2.5O2	2823.7	43.38	1548.4	1.2676	1275.3	1377.8	14.35	1.112	2062.4	0.850	178.7	0.39430	453.2
1	300	2.2C2H2+2.5O2	2875.6	44.57	1581.8	1.2652	1293.8	1410.2	14.90	1.111	2099.6	0.854	182.8	0.41727	438.0
1	300	2.4C2H2+2.5O2	2918.8	45.49	1611.6	1.2648	1307.2	1438.5	15.37	1.109	2127.6	0.858	186.1	0.43857	424.3
1	300	2.6C2H2+2.5O2	2902.2	44.75	1603.8	1.2599	1298.4	1435.1	15.23	1.109	2113.8	0.861	185.5	0.45837	404.7
1	300	C2H2+2.5O2	2424.2	33.63	1316.3	1.2633	1107.9	1170.4	10.90	1.117	1798.3	0.823	150.9	0.24556	614.4
1	300	C2H2+2.5O2+0.39N2	2368.9	31.91	1286.7	1.251	1082.2	1150.9	10.50	1.116	1756.9	0.829	148.5	0.22268	666.7
1	300	C2H2+2.5O2+0.88N2	2310.5	30.17	1255.4	1.238	1055.1	1129.8	10.08	1.116	1713.5	0.836	146.0	0.19945	732.1
1	300	C2H2+2.5O2+1.5N2	2248.2	28.37	1222.8	1.2251	1025.4	1107.4	9.64	1.115	1666.1	0.842	143.0	0.17587	813.1
1	300	C2H2+2.5O2+2.33N2	2180.7	26.53	1187.1	1.2115	993.6	1082.0	9.18	1.115	1615.1	0.849	139.8	0.15192	920.1
1	300	C2H2+2.5O2+3.5N2	2106.1	24.58	1148.4	1.1982	957.7	1053.5	8.66	1.114	1556.8	0.855	135.7	0.12759	1063.4
1	300	C2H2+2.5O2+5.25N2	2020.5	22.46	1104.6	1.1863	915.9	1019.3	8.07	1.113	1486.2	0.862	130.6	0.10287	1269.5
1	300	C2H2+2.5O2+8.17N2	1915.3	20.01	1052.5	1.1791	862.8	975.2	7.33	1.110	1392.7	0.869	123.4	0.07777	1586.5
1	300	C2H2+2.5N2+9.4N2	1878.8	19.2	1035.2	1.1793	843.6	959.6	7.08	1.109	1358.7	0.871	120.6	0.07050	1711.2
1	300	C2H2+2.5O2+14N2	1764.3	16.73	983.1	1.1906	781.2	908.7	6.25	1.105	1240.0	0.876	110.7	0.05226	2118.7
1	300	C2H2+2.5O2+31.5N2	1446.6	10.86	844.7	1.2741	601.9	762.2	4.18	1.087	890.1	0.883	80.1	0.02634	3041.5

Table 19: Impulse model predictions for H_2-O_2 mixtures

P_1 (bar)	T_1 (K)	Mixture	U_{CJ} (m/s)	P_2 (bar)	c_2 (m/s)	γ	u_2 (m/s)	c_3(m/s)	P_3 (bar)	α	I_V(kg/m^{2}s)	V(m^3/kg)	I_{SP} (s)	X_F	I_{SPF} (s)
0.2	300	2H2+O2	2751.6	3.53	1493.8	1.2253	1257.8	1352.1	1.19	1.116	28.6	10.38	30.2	0.11190	270.2
0.4	300	2H2+O2	2789.7	7.25	1515.7	1.2243	1274	1372.8	2.46	1.116	225.3	5.19	119.2	0.11190	1065.2
0.6	300	2H2+O2	2812.1	11.03	1528.7	1.2238	1283.4	1385.1	3.75	1.116	422.4	3.46	149.0	0.11190	1331.5
0.8	300	2H2+O2	2828.1	14.86	1538	1.2234	1290.1	1393.9	5.06	1.115	620.6	2.59	163.9	0.11190	1464.3
1	300	2H2+O2	2840.4	18.72	1545.2	1.2231	1295.2	1400.7	6.38	1.115	819.4	2.07	172.9	0.11190	1545.1
1.2	300	2H2+O2	2850.5	22.61	1551	1.2228	1299.5	1406.2	7.71	1.115	1018.8	1.73	179.7	0.11190	1605.6
1.4	300	2H2+O2	2859.2	26.58	1556	1.2226	1303.2	1411.0	9.07	1.115	1221.6	1.48	184.3	0.11190	1647.0
1.6	300	2H2+O2	2866.5	30.45	1560.2	1.2223	1306.3	1415.0	10.40	1.115	1418.9	1.3	188.0	0.11190	1680.4
1.8	300	2H2+O2	2873	34.4	1564	1.2221	1309	1418.6	11.76	1.115	1619.9	1.15	189.9	0.11190	1697.0
2	300	2H2+O2	2878.8	38.36	1567.3	1.2219	1311.5	1421.8	13.12	1.115	1820.8	1.04	193.0	0.11190	1725.1
1	300	0.4H2+O2	1825.3	14.94	1012.1	1.1698	813.2	943.1	5.64	1.106	1057.1	1.06	114.2	0.02458	4646.7
1	300	0.8H2+O2	2185.9	17.24	1193.6	1.17	992.3	1109.3	6.29	1.113	1022.3	1.34	139.6	0.04798	2910.1
1	300	1.2H2+O2	2446	18.1	1331.9	1.1935	1114.1	1224.1	6.39	1.114	942.2	1.59	152.7	0.07029	2172.7
1	300	1.6H2+O2	2659.9	18.52	1447.2	1.214	1212.7	1317.4	6.38	1.115	871.8	1.84	163.5	0.09157	1785.6
1	300	2H2+O2	2840.4	18.72	1545.2	1.2231	1295.2	1400.7	6.38	1.115	819.4	2.07	172.9	0.11190	1545.1
1	300	2.4H2+O2	2993.5	18.74	1629.2	1.2193	1364.3	1479.6	6.42	1.115	782.0	2.3	183.3	0.13135	1395.8
1	300	2.8H2+O2	3123.2	18.63	1701.7	1.2085	1421.5	1553.5	6.48	1.114	753.6	2.52	193.6	0.14995	1290.9
1	300	3.2H2+O2	3233.4	18.43	1764.6	1.1976	1468.8	1619.5	6.51	1.113	728.2	2.72	201.9	0.16778	1203.4
1	300	3.6H2+O2	3327.2	18.16	1819.6	1.1894	1507.6	1676.8	6.51	1.112	703.3	2.92	209.3	0.18488	1132.3
1	300	4H2+O2	3407.4	17.85	1868	1.1844	1539.4	1726.1	6.47	1.111	678.8	3.11	215.2	0.20128	1069.1
1	300	4.4H2+O2	3476.1	17.51	1910.9	1.1823	1565.2	1768.2	6.40	1.110	654.6	3.3	220.2	0.21704	1014.6
1	300	4.8H2+O2	3535.2	17.16	1948.7	1.1819	1586.5	1804.4	6.31	1.109	631.5	3.47	223.4	0.23219	962.0
1	300	5.2H2+O2	3586.2	16.8	1982.5	1.183	1603.7	1835.8	6.22	1.108	609.2	3.64	226.1	0.24677	916.1
1	300	2H2+O2	2840.4	18.72	1545.2	1.2231	1295.2	1400.7	6.38	1.115	819.4	2.07	172.9	0.11190	1545.1
1	300	2H2+O2+0.33N2	2641.8	18.35	1438	1.204	1203.8	1315.2	6.40	1.115	877.3	1.83	163.7	0.08889	1841.1
1	300	2H2+O2+0.75N2	2474	17.98	1348.4	1.1892	1125.6	1241.9	6.39	1.114	929.5	1.64	155.4	0.07069	2198.4
1	300	2H2+O2+1.29N2	2324.9	17.53	1269.8	1.1775	1055.1	1176.2	6.34	1.113	973.9	1.48	146.9	0.05596	2625.8
1	300	2H2+O2+2N2	2186.5	16.95	1198.3	1.1699	988.2	1114.4	6.23	1.111	1007.7	1.35	138.7	0.04380	3166.0
1	300	2H2+O2+3N2	2050.5	16.14	1130.5	1.1695	920	1052.5	6.02	1.109	1023.7	1.25	130.4	0.03358	3884.5
1	300	2H2+O2+3.76N2	1970.7	15.51	1092.3	1.1746	878.4	1015.6	5.82	1.106	1019.4	1.19	123.7	0.02852	4335.4
1	300	2H2+O2+4.5N2	1904.3	14.91	1061.5	1.1826	842.8	984.6	5.63	1.104	1007.8	1.15	118.1	0.02488	4749.3
1	300	2H2+O2+7N2	1722.9	12.88	981.4	1.2228	741.5	898.8	4.91	1.096	930.3	1.07	101.5	0.01737	5841.9
1	300	2H2+O2+12N2	1469.7	9.88	862.3	1.276	607.4	778.5	3.84	1.085	778.3	1	79.3	0.01083	7323.9
1	300	2H2+O2+27N2	1119.4	6.15	685	1.3203	434.4	615.4	2.54	1.071	534.7	0.94	51.2	0.00509	10070.0

Table 20: Impulse model predictions for Jet A-O_2 mixtures

P_1 (bar)	T_1 (K)	Mixture	U_{CJ} (m/s)	P_2 (bar)	c_2 (m/s)	γ	u_2 (m/s)	c_3(m/s)	P_3 (bar)	α	I_V(kg/m^{2}s)	V(m^3/kg)	I_{SP} (s)	X_F	I_{SPF} (s)
0.2	300	JetA+13O2	2163.4	6.91	1160.5	1.2098	1002.9	1055.3	2.31	1.121	262.8	3.233	86.6	0.22964	377.1
0.4	300	JetA+13O2	2191.9	14.16	1177.3	1.2103	1014.6	1070.6	4.74	1.121	745.6	1.616	122.8	0.22964	534.9
0.6	300	JetA+13O2	2208.8	21.54	1187.2	1.2107	1021.6	1079.6	7.23	1.121	1231.3	1.078	135.3	0.22964	589.2
0.8	300	JetA+13O2	2220.7	29	1194.2	1.2109	1026.5	1086.0	9.74	1.120	1719.1	0.808	141.6	0.22964	616.6
1	300	JetA+13O2	2230	36.53	1199.7	1.2111	1030.3	1091.0	12.28	1.120	2209.1	0.647	145.7	0.22964	634.5
1.2	300	JetA+13O2	2237.6	44.11	1204.1	1.2112	1033.5	1095.0	14.83	1.120	2700.3	0.539	148.4	0.22964	646.1
1.4	300	JetA+13O2	2244	51.74	1207.9	1.2113	1036.1	1098.4	17.41	1.120	3193.7	0.462	150.4	0.22964	655.0
1.6	300	JetA+13O2	2249.5	59.39	1211.2	1.2114	1038.3	1101.5	20.00	1.120	3687.2	0.404	151.8	0.22964	661.2
1.8	300	JetA+13O2	2254.4	67.08	1214.2	1.2115	1040.2	1104.2	22.60	1.120	4182.4	0.359	153.1	0.22964	666.5
2	300	JetA+13O2	2258.8	74.8	1216.8	1.2115	1042	1106.6	25.21	1.120	4678.5	0.323	154.0	0.22964	670.8
1	300	0.2JetA+13O2	1640.1	16.97	912.8	1.1856	727.3	845.3	6.36	1.105	1360.1	0.75	104.0	0.05626	1848.2
1	300	0.4JetA+13O2	1888.3	23.74	1023.8	1.1667	864.5	951.7	8.55	1.116	1701.8	0.718	124.6	0.10653	1169.2
1	300	0.6JetA+13O2	2031.9	28.5	1095.9	1.1866	936	1008.6	9.91	1.119	1892.5	0.692	133.5	0.15172	879.9
1	300	0.8JetA+13O2	2141.4	32.69	1152.9	1.2028	988.5	1052.7	11.11	1.120	2054.5	0.668	139.9	0.19255	726.6
1	300	1JetA+13O2	2230	36.53	1199.7	1.2111	1030.3	1091.0	12.28	1.120	2209.1	0.647	145.7	0.22964	634.5
1	300	1.2JetA+13O2	2301.3	40.01	1238.1	1.2106	1063.2	1126.1	13.46	1.120	2364.1	0.627	151.1	0.26346	573.5
1	300	1.4JetA+13O2	2354.6	42.99	1268.4	1.2017	1086.2	1158.9	14.65	1.119	2520.8	0.609	156.5	0.29444	531.5
1	300	1.6JetA+13O2	2385.5	45.11	1289.5	1.1905	1096	1185.1	15.70	1.118	2658.2	0.593	160.7	0.32292	497.6
1	300	1.8JetA+13O2	2386.5	45.94	1299	1.1896	1087.5	1195.9	16.28	1.114	2738.3	0.578	161.3	0.34920	462.0
1	300	2JetA+13O2	2352.7	45.22	1293.8	1.2044	1058.9	1185.6	16.15	1.110	2738.2	0.563	157.1	0.37350	420.7
1	300	2.2JetA+13O2	2283.8	43.01	1271.5	1.2303	1012.3	1154.9	15.40	1.105	2666.4	0.55	149.5	0.39606	377.4
1	300	2.4JetA+13O2	2180.7	39.55	1229.2	1.2601	951.5	1105.5	14.15	1.101	2539.6	0.538	139.3	0.41705	334.0
1	300	2.6JetA+13O2	2046.5	35.18	1166.4	1.2877	880.1	1039.8	12.58	1.096	2374.1	0.527	127.5	0.43663	292.1
1	300	JetA+13O2	2230	36.53	1199.7	1.2111	1030.3	1091.0	12.28	1.120	2209.1	0.647	145.7	0.22964	634.5
1	300	JetA+13O2+1.56N2	2188.1	34.26	1177.5	1.2009	1010.6	1076.0	11.66	1.120	2119.0	0.665	143.6	0.21248	676.0
1	300	JetA+13O2+3.5N2	2146.8	32.09	1156.3	1.1923	990.5	1061.1	11.05	1.119	2028.1	0.684	141.4	0.19435	727.6
1	300	JetA+13O2+6N2	2102.2	29.9	1133.6	1.1839	968.6	1044.5	10.43	1.119	1933.4	0.704	138.7	0.17513	792.2
1	300	JetA+13O2+9.33N2	2052.5	27.68	1108.7	1.176	943.8	1025.6	9.78	1.118	1835.0	0.726	135.8	0.15472	877.7
1	300	JetA+13O2+14N2	1995.7	25.38	1080.6	1.1686	915.1	1003.5	9.09	1.116	1730.0	0.749	132.1	0.13302	993.0
1	300	JetA+13O2+21N2	1927.7	22.92	1047.8	1.1632	879.9	976.0	8.33	1.115	1612.9	0.774	127.3	0.10990	1157.9
1	300	JetA+13O2+32.7N2	1839.9	20.15	1007.1	1.1636	832.8	939.0	7.44	1.112	1472.9	0.8	120.1	0.08522	1409.5
1	300	JetA+13O2+48.9N2	1743.3	17.51	965.3	1.1766	778	896.6	6.55	1.107	1327.8	0.821	111.1	0.06495	1711.0
1	300	JetA+13O2+56N2	1705.7	16.58	949.7	1.1853	756	879.7	6.22	1.105	1273.3	0.828	107.5	0.05880	1827.6
1	300	JetA+13O2+126N2	1409.6	10.63	823.5	1.2728	586.1	743.6	4.10	1.087	889.9	0.858	77.8	0.03047	2554.5

Table 21: Impulse model predictions for JP10-O_2 mixtures

P_1 (bar)	T_1 (K)	Mixture	U_{CJ} (m/s)	P_2 (bar)	c_2 (m/s)	γ	u_2 (m/s)	c_3(m/s)	P_3 (bar)	α	I_V(kg/m^{2}s)	V(m^3/kg)	I_{SP} (s)	X_F	I_{SPF} (s)
0.2	300	JP10+14O2	2221.3	7.34	1192.7	1.2241	1028.6	1077.4	2.42	1.121	278.6	3.202	90.9	0.23319	390.0
0.4	300	JP10+14O2	2252.2	15.05	1210.9	1.2249	1041.3	1093.8	4.97	1.121	772.9	1.6	126.1	0.23319	540.6
0.6	300	JP10+14O2	2270.5	22.91	1221.7	1.2254	1048.8	1103.5	7.58	1.120	1270.8	1.067	138.2	0.23319	592.7
0.8	300	JP10+14O2	2283.5	30.87	1229.5	1.2256	1054	1110.6	10.22	1.120	1771.9	0.8	144.5	0.23319	619.7
1	300	JP10+14O2	2293.6	38.89	1235.6	1.2259	1058	1116.1	12.89	1.120	2274.2	0.64	148.4	0.23319	636.2
1.2	300	JP10+14O2	2301.9	46.98	1240.7	1.226	1061.2	1120.8	15.59	1.120	2779.4	0.534	151.3	0.23319	648.8
1.4	300	JP10+14O2	2308.9	55.12	1244.8	1.2262	1064.1	1124.5	18.30	1.119	3285.2	0.457	153.0	0.23319	656.3
1.6	300	JP10+14O2	2315	63.3	1248.2	1.2263	1066.8	1127.5	21.02	1.119	3791.5	0.4	154.6	0.23319	663.0
1.8	300	JP10+14O2	2320.3	71.54	1251.1	1.2265	1069.2	1130.0	23.76	1.119	4299.7	0.356	156.0	0.23319	669.1
2	300	JP10+14O2	2325.1	79.79	1253.8	1.2265	1071.3	1132.5	26.50	1.119	4808.3	0.32	156.8	0.23319	672.6
1	300	0.2JP10+14O2	1681.6	17.95	930.7	1.1774	750.9	864.1	6.70	1.107	1415.3	0.745	107.5	0.05733	1874.8
1	300	0.4JP10+14O2	1928.1	24.84	1044.5	1.1743	883.6	967.5	8.85	1.116	1740.2	0.715	126.8	0.10845	1169.5
1	300	0.6JP10+14O2	2078.8	29.95	1121.6	1.1984	957.2	1026.6	10.29	1.119	1935.3	0.687	135.5	0.15430	878.3
1	300	0.8JP10+14O2	2196.4	34.57	1183.4	1.216	1013	1074.0	11.60	1.120	2107.5	0.663	142.4	0.19567	727.9
1	300	1JP10+14O2	2293.6	38.89	1235.6	1.2259	1058	1116.1	12.89	1.120	2274.2	0.64	148.4	0.23319	636.2
1	300	1.2JP10+14O2	2374.5	42.93	1279.7	1.228	1094.8	1154.9	14.21	1.120	2441.4	0.62	154.3	0.26735	577.1
1	300	1.4JP10+14O2	2440.2	46.61	1316.2	1.223	1124	1190.9	15.55	1.119	2609.4	0.601	159.9	0.29861	535.4
1	300	1.6JP10+14O2	2489.5	49.75	1345.4	1.2133	1144.1	1223.4	16.87	1.118	2772.8	0.584	165.1	0.32730	504.3
1	300	1.8JP10+14O2	2520.1	52.15	1366.2	1.2047	1153.9	1248.1	17.99	1.117	2913.7	0.568	168.7	0.35374	476.9
1	300	2JP10+14O2	2530	53.59	1378.6	1.203	1151.4	1261.7	18.76	1.114	3013.3	0.554	170.2	0.37818	450.0
1	300	2.2JP10+14O2	2519	54.02	1381.6	1.2095	1137.4	1262.5	19.07	1.112	3064.5	0.54	168.7	0.40084	420.8
1	300	2.4JP10+14O2	2488.8	53.5	1375.4	1.2224	1113.4	1251.6	18.97	1.108	3071.8	0.528	165.3	0.42191	391.9
1	300	2.6JP10+14O2	2440.8	52.09	1360.5	1.2404	1080.3	1230.6	18.50	1.105	3039.9	0.516	159.9	0.44154	362.1
1	300	JP10+14O2	2293.6	38.89	1235.6	1.2259	1058	1116.1	12.89	1.120	2274.2	0.64	148.4	0.23319	636.2
1	300	JP10+14O2+1.67N2	2248.4	36.39	1211.2	1.2145	1037.2	1100.0	12.22	1.120	2179.8	0.659	146.4	0.21593	678.1
1	300	JP10+14O2+3.75N2	2203.9	34	1188.1	1.2048	1015.8	1084.1	11.57	1.119	2084.8	0.678	144.1	0.19765	729.0
1	300	JP10+14O2+6.43N2	2156	31.6	1163.4	1.1953	992.6	1066.5	10.90	1.118	1985.8	0.699	141.5	0.17824	793.9
1	300	JP10+14O2+10N2	2103	29.18	1136.4	1.1856	966.6	1046.7	10.21	1.118	1884.2	0.721	138.5	0.15761	878.7
1	300	JP10+14O2+15N2	2042.8	26.69	1106.1	1.1766	936.7	1023.4	9.48	1.117	1775.7	0.745	134.8	0.13563	994.2
1	300	JP10+14O2+22.5N2	1971.5	24.06	1071	1.1686	900.5	995.1	8.68	1.115	1657.0	0.77	130.1	0.11217	1159.5
1	300	JP10+14O2+35N2	1881.2	21.14	1028	1.1653	853.2	957.5	7.76	1.112	1516.3	0.797	123.2	0.08707	1414.9
1	300	JP10+14O2+52.64N2	1783.5	18.4	983.9	1.1727	799.6	914.9	6.85	1.108	1372.5	0.819	114.6	0.06617	1731.8
1	300	JP10+14O2+60N2	1748	17.49	968.9	1.1793	779.1	899.1	6.54	1.107	1321.4	0.826	111.3	0.06015	1849.9
1	300	JP10+14O2+135N2	1458.5	11.4	847.4	1.2651	611.1	766.4	4.37	1.089	939.1	0.857	82.0	0.03120	2629.3

Table 22: Impulse model predictions for C_2H_4-air mixtures

P_1 (bar)	T_1 (K)	Mixture	U_{CJ} (m/s)	P_2 (bar)	c_2 (m/s)	γ	u_2 (m/s)	c_3(m/s)	P_3 (bar)	α	I_V(kg/m^{2}s)	V(m^3/kg)	I_{SP} (s)	X_F	I_{SPF} (s)
0.2	300	C2H4+3O2+11.28N2	1791.6	3.54	984	1.1629	807.6	918.2	1.32	1.110	71.5	4.33	31.6	0.06375	495.0
0.4	300	C2H4+3O2+11.28N2	1806.2	7.18	993.5	1.1666	812.7	925.8	2.67	1.110	385.7	2.165	85.1	0.06375	1335.0
0.6	300	C2H4+3O2+11.28N2	1814.5	10.85	998.9	1.1688	815.6	930.1	4.04	1.109	699.4	1.443	102.9	0.06375	1613.8
0.8	300	C2H4+3O2+11.28N2	1820.2	14.54	1002.8	1.1704	817.4	933.2	5.41	1.109	1013.6	1.083	111.9	0.06375	1755.3
1	300	C2H4+3O2+11.28N2	1824.6	18.25	1005.8	1.1717	818.8	935.5	6.79	1.109	1328.3	0.866	117.3	0.06375	1839.3
1.2	300	C2H4+3O2+11.28N2	1828.2	21.97	1008.2	1.1727	820	937.4	8.17	1.109	1643.0	0.722	120.9	0.06375	1896.7
1.4	300	C2H4+3O2+11.28N2	1831.2	25.7	1010.2	1.1736	821	938.9	9.56	1.108	1957.7	0.619	123.5	0.06375	1937.6
1.6	300	C2H4+3O2+11.28N2	1833.7	29.44	1011.9	1.1744	821.8	940.2	10.95	1.108	2272.8	0.541	125.3	0.06375	1966.0
1.8	300	C2H4+3O2+11.28N2	1835.9	33.19	1013.4	1.175	822.5	941.4	12.34	1.108	2588.5	0.481	126.9	0.06375	1990.8
2	300	C2H4+3O2+11.28N2	1837.9	36.94	1014.7	1.1756	823.2	942.4	13.73	1.108	2903.3	0.433	128.1	0.06375	2010.1
1	300	0.4C2H4+3O2+11.28N2	1424.6	10.8	829.6	1.2652	595	750.7	4.16	1.088	899.7	0.865	79.3	0.02652	2992.0
1	300	0.6C2H4+3O2+11.28N2	1623.8	14.16	922.2	1.2227	701.6	844.1	5.36	1.097	1104.9	0.865	97.4	0.03925	2482.1
1	300	0.8C2H4+3O2+11.28N2	1749.7	16.7	973.1	1.1837	776.6	901.8	6.26	1.105	1251.5	0.866	110.5	0.05166	2138.5
1	300	1C2H4+3O2+11.28N2	1824.6	18.25	1005.8	1.1717	818.8	935.5	6.79	1.109	1328.3	0.866	117.3	0.06375	1839.3
1	300	1.2C2H4+3O2+11.28N2	1868.1	19.04	1031.6	1.1783	836.5	957.0	7.06	1.108	1359.2	0.866	120.0	0.07554	1588.4
1	300	1.4C2H4+3O2+11.28N2	1887.2	19.2	1051.3	1.1983	835.9	968.4	7.12	1.105	1353.8	0.866	119.5	0.08704	1373.1
1	300	1.6C2H4+3O2+11.28N2	1888	18.99	1062.1	1.2217	825.9	970.5	7.03	1.101	1330.2	0.867	117.6	0.09825	1196.6
1	300	1.8C2H4+3O2+11.28N2	1878.7	18.64	1064.7	1.2399	814	967.1	6.90	1.098	1303.8	0.867	115.2	0.10919	1055.3
1	300	2C2H4+3O2+11.28N2	1864.2	18.24	1062.3	1.2533	801.9	960.7	6.75	1.096	1278.3	0.867	113.0	0.11986	942.5
1	300	2.2C2H4+3O2+11.28N2	1846.3	17.8	1056.9	1.2644	789.4	952.5	6.59	1.095	1252.2	0.868	110.8	0.13029	850.3
1	300	2.4C2H4+3O2+11.28N2	1825.8	17.33	1049.5	1.2745	776.3	943.0	6.41	1.093	1225.2	0.868	108.4	0.14047	771.7
1	300	2.6C2H4+3O2+11.28N2	1802.8	16.83	1040.4	1.2838	762.4	932.2	6.23	1.092	1197.4	0.868	105.9	0.15041	704.4

Table 23: Impulse model predictions for C_3H_8-air mixtures

P_1 (bar)	T_1 (K)	Mixture	U_{CJ} (m/s)	P_2 (bar)	c_2 (m/s)	γ	u_2 (m/s)	c_3(m/s)	P_3 (bar)	α	I_V(kg/m^{2}s)	V(m^3/kg)	I_{SP} (s)	X_F	I_{SPF} (s)
0.2	300	C3H8+5O2+18.8N2	1771.1	3.53	974.4	1.1645	796.7	908.9	1.32	1.109	72.0	4.23	31.1	0.06035	514.7
0.4	300	C3H8+5O2+18.8N2	1784.2	7.15	983.3	1.1687	800.9	915.7	2.67	1.109	388.6	2.116	83.8	0.06035	1389.1
0.6	300	C3H8+5O2+18.8N2	1791.6	10.8	988.3	1.1711	803.3	919.6	4.03	1.108	705.1	1.41	101.3	0.06035	1679.4
0.8	300	C3H8+5O2+18.8N2	1796.7	14.47	991.7	1.1726	805	922.2	5.39	1.108	1021.9	1.058	110.2	0.06035	1826.4
1	300	C3H8+5O2+18.8N2	1800.6	18.15	994.4	1.174	806.2	924.3	6.76	1.108	1338.5	0.846	115.4	0.06035	1912.9
1.2	300	C3H8+5O2+18.8N2	1803.7	21.84	996.6	1.1751	807.1	925.9	8.14	1.108	1655.4	0.705	119.0	0.06035	1971.5
1.4	300	C3H8+5O2+18.8N2	1806.3	25.54	998.4	1.1761	807.9	927.3	9.52	1.108	1972.3	0.605	121.6	0.06035	2015.7
1.6	300	C3H8+5O2+18.8N2	1808.5	29.24	999.9	1.1769	808.6	928.4	10.89	1.108	2288.8	0.529	123.4	0.06035	2045.3
1.8	300	C3H8+5O2+18.8N2	1810.5	32.95	1001.3	1.1776	809.2	929.4	12.27	1.107	2605.7	0.47	124.8	0.06035	2068.8
2	300	C3H8+5O2+18.8N2	1812.2	36.67	1002.5	1.1783	809.7	930.3	13.66	1.107	2923.0	0.423	126.0	0.06035	2088.6
1	300	0.4C3H8+5O2+18.8N2	1388.9	10.35	811.7	1.2704	577.2	733.7	4.00	1.087	874.2	0.857	76.4	0.02505	3049.4
1	300	0.6C3H8+5O2+18.8N2	1587.7	13.68	906.2	1.2332	681.5	826.7	5.18	1.095	1082.3	0.853	94.1	0.03710	2536.4
1	300	0.8C3H8+5O2+18.8N2	1721.5	16.39	961.7	1.1923	759.8	888.6	6.15	1.103	1243.4	0.85	107.7	0.04887	2204.7
1	300	1C3H8+5O2+18.8N2	1800.6	18.15	994.4	1.174	806.2	924.3	6.76	1.108	1338.5	0.846	115.4	0.06035	1912.9
1	300	1.2C3H8+5O2+18.8N2	1835.6	18.78	1018.8	1.1871	816.8	942.4	6.98	1.106	1361.6	0.843	117.0	0.07155	1635.3
1	300	1.4C3H8+5O2+18.8N2	1834.1	18.52	1032	1.2197	802.1	943.9	6.88	1.101	1332.5	0.84	114.1	0.08249	1383.1
1	300	1.6C3H8+5O2+18.8N2	1813.5	17.99	1029.9	1.2424	783.6	934.9	6.67	1.097	1297.3	0.836	110.6	0.09318	1186.5
1	300	1.8C3H8+5O2+18.8N2	1785.3	17.39	1020.1	1.2572	765.2	921.7	6.45	1.095	1263.4	0.833	107.3	0.10362	1035.3
1	300	2C3H8+5O2+18.8N2	1752.5	16.74	1006.4	1.2685	746.1	906.2	6.22	1.093	1229.0	0.83	104.0	0.11382	913.6
1	300	2.2C3H8+5O2+18.8N2	1716.1	16.06	989.8	1.2781	726.3	888.8	5.97	1.092	1193.8	0.827	100.6	0.12380	812.9
1	300	2.4C3H8+5O2+18.8N2	1676.4	15.34	971	1.2869	705.4	869.8	5.72	1.090	1156.4	0.825	97.2	0.13355	728.2
1	300	2.6C3H8+5O2+18.8N2	1633.3	14.58	950	1.2951	683.3	849.2	5.45	1.089	1116.4	0.822	93.5	0.14308	653.8

Table 24: Impulse model predictions for C_2H_2-air mixtures

P_1 (bar)	T_1 (K)	Mixture	U_{CJ} (m/s)	P_2 (bar)	c_2 (m/s)	γ	u_2 (m/s)	c_3(m/s)	P_3 (bar)	α	I_V(kg/m^{2}s)	V(m^3/kg)	I_{SP} (s)	X_F	I_{SPF} (s)
0.2	300	C2H2+2.5O2+9.4N2	1838	3.7	1009.1	1.1706	828.9	938.4	1.37	1.110	80.7	4.355	35.8	0.07050	508.3
0.4	300	C2H2+2.5O2+9.4N2	1855.8	7.52	1020.4	1.1744	835.4	947.6	2.77	1.110	399.4	2.178	88.7	0.07050	1258.0
0.6	300	C2H2+2.5O2+9.4N2	1866.1	11.39	1027	1.1766	839.1	952.9	4.20	1.109	718.9	1.452	106.4	0.07050	1509.5
0.8	300	C2H2+2.5O2+9.4N2	1873.3	15.28	1031.6	1.1781	841.7	956.6	5.63	1.109	1038.2	1.089	115.2	0.07050	1634.8
1	300	C2H2+2.5O2+9.4N2	1878.8	19.2	1035.2	1.1793	843.6	959.6	7.08	1.109	1358.7	0.871	120.6	0.07050	1711.2
1.2	300	C2H2+2.5O2+9.4N2	1883.3	23.13	1038.1	1.1802	845.2	961.9	8.53	1.109	1679.0	0.726	124.3	0.07050	1762.6
1.4	300	C2H2+2.5O2+9.4N2	1887.1	27.08	1040.5	1.1811	846.6	963.8	9.98	1.109	1999.7	0.622	126.8	0.07050	1798.5
1.6	300	C2H2+2.5O2+9.4N2	1890.3	31.03	1042.6	1.1818	847.7	965.5	11.44	1.109	2320.1	0.544	128.7	0.07050	1825.1
1.8	300	C2H2+2.5O2+9.4N2	1893.1	35	1044.4	1.1825	848.7	967.0	12.90	1.109	2641.3	0.484	130.3	0.07050	1848.6
2	300	C2H2+2.5O2+9.4N2	1895.6	38.98	1046.1	1.183	849.5	968.4	14.37	1.108	2963.5	0.435	131.4	0.07050	1864.1
1	300	0.4C2H2+2.5O2+9.4N2	1497.1	11.84	869.3	1.268	627.8	785.2	4.52	1.089	957.2	0.867	84.6	0.02944	2873.1
1	300	0.6C2H2+2.5O2+9.4N2	1696.9	15.47	956.4	1.2115	740.5	878.1	5.81	1.100	1174.1	0.869	104.0	0.04352	2389.7
1	300	0.8C2H2+2.5O2+9.4N2	1807.8	17.76	1001.4	1.1825	806.4	927.8	6.61	1.107	1295.9	0.87	114.9	0.05720	2009.2
1	300	1C2H2+2.5O2+9.4N2	1878.8	19.2	1035.2	1.1793	843.6	959.6	7.08	1.109	1358.7	0.871	120.6	0.07050	1711.2
1	300	1.2C2H2+2.5O2+9.4N2	1930.9	20.2	1063.6	1.1833	867.3	984.1	7.41	1.109	1396.8	0.872	124.2	0.08342	1488.4
1	300	1.4C2H2+2.5O2+9.4N2	1970.3	20.9	1088.3	1.1908	882	1004.2	7.65	1.108	1420.6	0.873	126.4	0.09599	1317.1
1	300	1.6C2H2+2.5O2+9.4N2	1999.1	21.33	1109.7	1.2018	889.4	1020.0	7.81	1.106	1430.9	0.875	127.6	0.10821	1179.4
1	300	1.8C2H2+2.5O2+9.4N2	2018.6	21.56	1126.9	1.2148	891.7	1031.1	7.90	1.104	1431.6	0.876	127.8	0.12012	1064.2
1	300	2C2H2+2.5O2+9.4N2	2031.6	21.66	1139.8	1.2269	891.8	1038.6	7.93	1.102	1426.7	0.877	127.5	0.13170	968.5
1	300	2.2C2H2+2.5O2+9.4N2	2040.4	21.71	1149.3	1.2368	891.1	1043.8	7.94	1.101	1421.7	0.878	127.2	0.14299	889.8
1	300	2.4C2H2+2.5O2+9.4N2	2046.7	21.73	1156.4	1.2449	890.3	1047.4	7.94	1.100	1416.3	0.879	126.9	0.15399	824.1
1	300	2.6C2H2+2.5O2+9.4N2	2037.7	21.48	1153.2	1.2482	884.5	1043.4	7.85	1.099	1403.7	0.88	125.9	0.16471	764.5

Table 25: Impulse model predictions for H_2-air mixtures

P_1 (bar)	T_1 (K)	Mixture	U_{CJ} (m/s)	P_2 (bar)	c_2 (m/s)	γ	u_2 (m/s)	c_3(m/s)	P_3 (bar)	α	I_V(kg/m^{2}s)	V(m^3/kg)	I_{SP} (s)	X_F	I_{SPF} (s)
0.2	300	2H2+O2+3.76N2	1934.2	3.01	1067.1	1.1644	867.1	995.8	1.13	1.108	25.4	5.96	15.4	0.02852	540.2
0.4	300	2H2+O2+3.76N2	1950.5	6.11	1078	1.1684	872.5	1004.5	2.29	1.108	274.5	2.98	83.4	0.02852	2923.9
0.6	300	2H2+O2+3.76N2	1959.6	9.23	1084.5	1.1712	875.1	1009.6	3.47	1.107	523.0	1.99	106.1	0.02852	3719.6
0.8	300	2H2+O2+3.76N2	1965.9	12.36	1089	1.1731	876.9	1013.1	4.64	1.107	771.0	1.49	117.1	0.02852	4105.5
1	300	2H2+O2+3.76N2	1970.7	15.51	1092.3	1.1746	878.4	1015.6	5.82	1.106	1019.4	1.19	123.7	0.02852	4335.4
1.2	300	2H2+O2+3.76N2	1974.6	18.67	1095	1.1758	879.6	1017.7	7.01	1.106	1268.0	0.99	128.0	0.02852	4486.3
1.4	300	2H2+O2+3.76N2	1977.8	21.89	1097.3	1.1769	880.5	1019.4	8.22	1.106	1520.8	0.85	131.8	0.02852	4619.9
1.6	300	2H2+O2+3.76N2	1980.5	25.01	1099.2	1.1777	881.3	1020.9	9.39	1.106	1765.5	0.75	135.0	0.02852	4732.1
1.8	300	2H2+O2+3.76N2	1982.9	28.19	1100.9	1.1785	882	1022.2	10.58	1.106	2014.3	0.66	135.5	0.02852	4751.2
2	300	2H2+O2+3.76N2	1985	31.38	1102.4	1.1793	882.6	1023.3	11.78	1.106	2263.5	0.596	137.5	0.02852	4821.3
1	300	0.8H2+O2+3.76N2	1491.3	10.31	868.6	1.2597	622.7	787.7	4.00	1.088	812.5	0.99	82.0	0.01161	7063.7
1	300	1.2H2+O2+3.76N2	1709.6	12.83	973.5	1.2205	736.1	892.3	4.89	1.096	934.4	1.06	101.0	0.01731	5832.4
1	300	1.6H2+O2+3.76N2	1865.3	14.56	1044.5	1.1903	820.8	966.4	5.51	1.102	1000.1	1.13	115.2	0.02295	5019.8
1	300	2H2+O2+3.76N2	1970.7	15.51	1092.3	1.1746	878.4	1015.6	5.82	1.106	1019.4	1.19	123.7	0.02852	4335.4
1	300	2.4H2+O2+3.76N2	2033	15.63	1129	1.1792	904	1048.0	5.87	1.106	996.4	1.26	128.0	0.03403	3760.5
1	300	2.8H2+O2+3.76N2	2072.3	15.38	1157.5	1.1905	914.8	1070.4	5.78	1.104	958.1	1.32	128.9	0.03948	3265.2
1	300	3.2H2+O2+3.76N2	2101.5	15.02	1180.1	1.201	921.4	1087.5	5.66	1.101	917.6	1.38	129.1	0.04487	2876.8
1	300	3.6H2+O2+3.76N2	2125.3	14.65	1199	1.2104	926.3	1101.6	5.52	1.100	879.6	1.44	129.1	0.05020	2572.4
1	300	4H2+O2+3.76N2	2146.4	14.29	1215.7	1.2183	930.7	1114.1	5.40	1.098	844.6	1.5	129.2	0.05546	2328.6
1	300	4.4H2+O2+3.76N2	2165	13.95	1230.6	1.2252	934.4	1125.4	5.28	1.097	813.0	1.56	129.3	0.06067	2130.7
1	300	4.8H2+O2+3.76N2	2181.5	13.61	1244	1.2316	937.5	1135.4	5.15	1.096	782.5	1.62	129.2	0.06583	1963.2
1	300	5.2H2+O2+3.76N2	2196.4	13.28	1256.4	1.2377	940	1144.7	5.04	1.095	753.9	1.68	129.1	0.07092	1820.5
1	300	5.6H2+O2+3.76N2	2209.9	12.97	1268	1.2437	941.9	1153.2	4.92	1.093	727.6	1.74	129.1	0.07596	1699.0

Table 26: Impulse model predictions for Jet A-air mixtures

P_1 (bar)	T_1 (K)	Mixture	U_{CJ} (m/s)	P_2 (bar)	c_2 (m/s)	γ	u_2 (m/s)	c_3(m/s)	P_3 (bar)	α	I_V(kg/m^{2}s)	V(m^3/kg)	I_{SP} (s)	X_F	I_{SPF} (s)
0.2	300	JetA+13O2+48.9N2	1717.2	3.42	946.8	1.1659	770.4	882.9	1.28	1.109	65.2	4.107	27.3	0.06495	420.4
0.4	300	JetA+13O2+48.9N2	1728.8	6.92	954.9	1.1704	773.9	889.0	2.59	1.108	381.6	2.053	79.9	0.06495	1229.7
0.6	300	JetA+13O2+48.9N2	1735.3	10.43	959.5	1.1731	775.8	892.4	3.90	1.107	696.4	1.369	97.2	0.06495	1496.4
0.8	300	JetA+13O2+48.9N2	1739.8	13.97	962.8	1.1751	777	894.8	5.22	1.107	1012.6	1.027	106.0	0.06495	1632.3
1	300	JetA+13O2+48.9N2	1743.3	17.51	965.3	1.1766	778	896.6	6.55	1.107	1327.8	0.821	111.1	0.06495	1711.0
1.2	300	JetA+13O2+48.9N2	1746	21.06	967.3	1.1778	778.7	898.1	7.87	1.107	1643.3	0.684	114.6	0.06495	1764.2
1.4	300	JetA+13O2+48.9N2	1748.3	24.62	968.9	1.1789	779.4	899.2	9.20	1.107	1958.7	0.587	117.2	0.06495	1804.6
1.6	300	JetA+13O2+48.9N2	1750.2	28.19	970.3	1.1798	779.9	900.2	10.53	1.106	2274.9	0.513	119.0	0.06495	1831.7
1.8	300	JetA+13O2+48.9N2	1752	31.76	971.6	1.1806	780.4	901.1	11.87	1.106	2590.5	0.456	120.4	0.06495	1854.1
2	300	JetA+13O2+48.9N2	1753.5	35.34	972.7	1.1813	780.8	901.9	13.20	1.106	2906.8	0.411	121.8	0.06495	1875.1
1	300	0.4JetA+13O2+48.9N2	1341.1	9.78	787.1	1.2755	554	710.8	3.80	1.085	842.2	0.847	72.7	0.02703	2690.1
1	300	0.6JetA+13O2+48.9N2	1533.6	12.97	879.7	1.242	653.9	800.6	4.93	1.094	1049.6	0.838	89.7	0.04001	2241.0
1	300	0.8JetA+13O2+48.9N2	1667.1	15.69	935.9	1.2012	731.2	862.3	5.90	1.102	1218.7	0.83	103.1	0.05264	1958.8
1	300	1JetA+13O2+48.9N2	1743.3	17.51	965.3	1.1766	778	896.6	6.55	1.107	1327.8	0.821	111.1	0.06495	1711.0
1	300	1.2JetA+13O2+48.9N2	1761.3	17.81	985.2	1.2015	776.1	907.0	6.64	1.103	1333.3	0.813	110.5	0.07694	1436.3
1	300	1.4JetA+13O2+48.9N2	1729.5	17.01	983.4	1.2416	746.1	893.3	6.33	1.097	1276.6	0.806	104.9	0.08862	1183.5
1	300	1.6JetA+13O2+48.9N2	1679.2	16.07	962.8	1.2606	716.4	869.5	5.99	1.094	1226.2	0.798	99.7	0.10002	997.3
1	300	1.8JetA+13O2+48.9N2	1621.9	15.08	935.6	1.2728	686.3	842.0	5.64	1.092	1176.0	0.791	94.8	0.11113	853.3
1	300	2JetA+13O2+48.9N2	1558.8	14.02	904.1	1.2826	654.7	811.6	5.26	1.090	1120.7	0.784	89.6	0.12197	734.3
1	300	2.2JetA+13O2+48.9N2	1489.4	12.9	869.2	1.2928	620.2	778.4	4.87	1.087	1060.1	0.776	83.9	0.13255	632.7
1	300	2.4JetA+13O2+48.9N2	1412.6	11.69	830.3	1.3038	582.3	741.8	4.45	1.085	990.1	0.77	77.7	0.14288	543.9
1	300	2.6JetA+13O2+48.9N2	1326.1	10.38	786.6	1.3177	539.5	700.9	3.99	1.082	907.9	0.763	70.6	0.15296	461.7

Table 27: Impulse model predictions for JP10-air mixtures

P_1 (bar)	T_1 (K)	Mixture	U_{CJ} (m/s)	P_2 (bar)	c_2 (m/s)	γ	u_2 (m/s)	c_3(m/s)	P_3 (bar)	α	I_V(kg/m^{2}s)	V(m^3/kg)	I_{SP} (s)	X_F	I_{SPF} (s)
0.2	300	JP10+14O2+52.64N2	1753.5	3.58	963.9	1.1636	789.6	899.3	1.33	1.110	77.0	4.097	32.1	0.06617	485.7
0.4	300	JP10+14O2+52.64N2	1766.7	7.25	972.7	1.1676	794	906.2	2.70	1.109	400.9	2.048	83.7	0.06617	1264.9
0.6	300	JP10+14O2+52.64N2	1774.3	10.95	977.7	1.1697	796.6	910.1	4.08	1.109	724.7	1.366	100.9	0.06617	1525.2
0.8	300	JP10+14O2+52.64N2	1779.5	14.67	981.2	1.1714	798.3	912.8	5.46	1.109	1048.7	1.024	109.5	0.06617	1654.4
1	300	JP10+14O2+52.64N2	1783.5	18.4	983.9	1.1727	799.6	914.9	6.85	1.108	1372.5	0.819	114.6	0.06617	1731.8
1.2	300	JP10+14O2+52.64N2	1786.7	22.15	986.1	1.1738	800.6	916.5	8.24	1.108	1697.3	0.682	118.0	0.06617	1783.3
1.4	300	JP10+14O2+52.64N2	1789.3	25.9	987.9	1.1747	801.4	917.9	9.64	1.108	2021.5	0.585	120.6	0.06617	1821.9
1.6	300	JP10+14O2+52.64N2	1791.6	29.66	989.5	1.1755	802.1	919.1	11.04	1.108	2346.0	0.512	122.4	0.06617	1850.5
1.8	300	JP10+14O2+52.64N2	1793.6	33.43	990.9	1.1763	802.7	920.1	12.44	1.108	2670.8	0.455	123.9	0.06617	1872.1
2	300	JP10+14O2+52.64N2	1795.4	37.2	992.1	1.1769	803.3	921.0	13.84	1.108	2995.1	0.41	125.2	0.06617	1891.8
1	300	0.4JP10+14O2+52.64N2	1385.5	10.44	809.3	1.2701	576.2	731.5	4.03	1.087	885.9	0.846	76.4	0.02756	2771.9
1	300	0.6JP10+14O2+52.64N2	1581.8	13.85	902	1.2319	679.8	823.2	5.24	1.096	1102.6	0.837	94.1	0.04078	2306.8
1	300	0.8JP10+14O2+52.64N2	1710.1	16.62	953.8	1.1896	756.3	882.1	6.23	1.104	1272.4	0.828	107.4	0.05365	2002.0
1	300	1JP10+14O2+52.64N2	1783.5	18.4	983.9	1.1727	799.6	914.9	6.85	1.108	1372.5	0.819	114.6	0.06617	1731.8
1	300	1.2JP10+14O2+52.64N2	1817.2	19.16	1006.5	1.1839	810.7	932.0	7.11	1.107	1407.3	0.811	116.3	0.07837	1484.6
1	300	1.4JP10+14O2+52.64N2	1816.6	19.01	1020.4	1.2171	796.2	934.0	7.05	1.102	1386.3	0.803	113.5	0.09025	1257.4
1	300	1.6JP10+14O2+52.64N2	1794	18.5	1018.5	1.2437	775.5	924.0	6.85	1.098	1353.0	0.795	109.6	0.10183	1076.8
1	300	1.8JP10+14O2+52.64N2	1762	17.89	1007.1	1.2601	754.9	908.9	6.62	1.095	1321.2	0.787	106.0	0.11312	937.0
1	300	2JP10+14O2+52.64N2	1725.1	17.23	991.1	1.2723	734	891.2	6.38	1.093	1289.0	0.78	102.5	0.12412	825.7
1	300	2.2JP10+14O2+52.64N2	1684.3	16.52	972.2	1.2827	712.1	871.5	6.13	1.091	1255.1	0.773	98.9	0.13486	733.3
1	300	2.4JP10+14O2+52.64N2	1639.8	15.76	950.8	1.2925	689	850.0	5.86	1.090	1218.1	0.765	95.0	0.14534	653.6
1	300	2.6JP10+14O2+52.64N2	1591.3	14.94	927	1.302	664.3	826.7	5.57	1.088	1177.1	0.758	90.9	0.15557	584.6